

El trabajo experimental presentado en esta tesis doctoral ha sido realizado en la División de Biomedicina Epitelial del Centro de Investigaciones Energéticas, Medioambientales y Tecnológicas (CIEMAT) en Madrid y en el Departamento de Bioingeniería e Ingeniería Aeroespacial de la Universidad Carlos III de Madrid.

Verónica López Llorente ha disfrutado de una beca predoctoral de Formación de Personal Investigador concedida por el CIEMAT.



Universidad
de Alcalá

Programa de Doctorado en Señalización Celular

**Detection and characterization of mechanical forces and
molecular dynamic rearrangements in collective cell
migration**

Tesis Doctoral presentada por:

Verónica López Llorente

Directores:

Dr. José Luis Jorcano Noval

Dra. Marta García Díez

Dr. Javier Rodríguez Rodríguez

2021

A aquellos brazos que siempre encuentro abiertos,

sin condiciones,

desde el corazón.

A mi familia.



AGRADECIMIENTOS

*“Allí es Wendy,
la segunda estrella a la derecha,
recto hasta el amanecer.”
(Peter Pan, J.M. Barrie)*

La respuesta a la pregunta es la siguiente: No. No me arrepiento.

Una de las grandes cosas que he aprendido durante estos años, es a valorar lo que es realmente importante, y si pudiera, lo añadiría a la sección de resultados de esta tesis. Muchas veces nos perdemos entre marañas de rutinas, presiones y agobios y no somos capaces de ver nada más allá.

Ahora, después de muchas sonrisas y también (por qué no decirlo) muchas lágrimas, agradezco que mi “yo” de 2016 tomase la decisión de dejarlo todo por hacerme feliz a mí. Ella, que a pesar de saber sobradamente que iba a ser un camino difícil, tuvo el valor de hacerlo. Lo hizo por mí y por mi futuro. Por la pasión de dedicarse a algo que hace que se le llenen los ojos de ilusión. Por la esperanza de que algún día todo su esfuerzo sirva para que alguien, aunque sea una sola persona enferma en el mundo, pueda vivir un poquito mejor. Entonces el sueño se habría cumplido. Entonces yo me merece la pena.

Por supuesto, es mucho más difícil crecer si no tienes a todas las personas valiosas que yo he tenido (y tengo) la suerte de tener a mi lado. Podría rellenar otros dos tomos contando lo que me han aportado todas y cada una de ellas, pero creo que no es necesario haceros sufrir con tanta lectura.

Trabajar en un campo tan diferente al mío me ha permitido aprender a ver las cosas con ojos de ingeniero, a abrir la mente, a conectar y a mirar desde otros puntos de vista. Gracias a mis tres directores: José Luis Jorcano, por darme la oportunidad de aprender con vosotros cada día y poder desarrollarme como investigador y como persona. Marta García, por acogerme y enseñarme desde el primer día con esa alegría que te caracteriza y por recibirme siempre con esa sonrisa que te anima y te asegura que “todo va a salir bien”. Y, por último, pero no menos importante, a Javier Rodríguez, por todo el tiempo y cariño que has dedicado a desentrañarme los secretos de la física y contagiarme tu ilusión por la ciencia. También a mi tutor de la UAH, Alberto Domingo, por su apoyo, incluso desde antes de comenzar este camino, y porque con su ayuda todos los trámites han sido mucho más llevaderos.

Gracias a Curra, del servicio de microscopía de la Fundación Jiménez Díaz, por todas las “gélidas” horas de confocal y por las buenas ideas que has aportado para mejorar. También al servicio de microscopía del Centro Nacional de Biotecnología por vuestro impecable trabajo. En especial a Sylvia Gutiérrez y a Ana Oña, por transmitirme vuestros conocimientos, ideas y soluciones para muestras “imposibles”, por vuestra implicación y ayuda. Ha sido un placer trabajar con grandes profesionales como vosotras.

A mis compañeros de la UC3M: Gonzalo, Ignacio, Cristina, Jorge, Leti, Angélica, Guille, Miguel, Diego, Marisa, Marina, Ana, Encarni, Carlos, Lucía, Sara. Por los experimentos fallidos, momentos y cocidos madrileños compartidos al principio de los tiempos. Andrés, gracias por tus palabras y por tu compañía, tan necesarias en momentos tan difíciles, espero que te vaya todo muy bien. Y a las nuevas incorporaciones, Iria y Cristina M., os deseo mucha suerte en vuestra nueva etapa. Iria, gracias aquí (y allí) por estar siempre dispuesta a ayudar cuando se necesita. Ha sido un camino muy difícil y solitario. De aquí me llevo, quizá, el aprendizaje más importante de

esta etapa: a confiar en mí misma y darme cuenta de que, pase lo que pase, soy capaz de superar las dificultades.

También a mis compañeros de batallas y amigos del CIEMAT. Con vosotros he aprendido lo que sé, he reído, he llorado, me he perdido, la he liado, y gracias a vuestra ayuda, lo he solucionado.

A los "oncolocos" (Cristian, Sara, Carol, "la Raque", "la Jose", Ester, Ricky, Iris, Jessy, Miriam, Carmensín, pequeña Flippy) y "pequehematos" (Sergio, Fran, Sara, Oma, Cris, Fans, Yari, Carlos, Andrea, Virgi, Chuchi y Merche, Sario, Raqueliña, Manué, Laura carapapa). Al equipo de "gestiones, pedidos y todo tipo de maniobras de salvamento" más divertido de la historia (Sole, Sergio, Mamen, Aurora). A Marisa siempre pendiente de todos nosotros. A Pilar y Kiko (sin vuestra ayuda todavía estaría procesando muestras). A todos los investigadores "veteranos" del CIEMAT (sin ofender), porque sé que os habéis preocupado de cómo me iban las cosas y me habéis animado siempre que habéis tenido oportunidad. Podría escribir mil cosas buenas de todos vosotros, pero eso merecería un libro aparte. Solo deciros, que jamás me hubiera esperado encontrar personas como vosotros el día que llegué.

Han pasado muchas cosas. Buenas (buenísimas), pero también no tan buenas. Esta etapa me ha hecho llevar al límite todas mis emociones. Por eso, me habéis visto reír a carcajadas y derrumbarme como si fuese un castillo de naipes. Vosotros me habéis hecho explotar de alegría en los karaokes, en la playa, en los escenarios, en las fiestas y videos de tesis, en congresos, aprendiendo a bailar salsa, intentando correr más de 10 minutos seguidos sin desmayarme o canturreando como una loca por los pasillos toooodas y cada una de las canciones que suenan en mi cabeza. Pero también me habéis visto desaparecer y encerrarme en mí misma cuando no podía más. Pasar fugazmente entre la gente, casi desapercibida. Y, aun así, nunca me ha faltado vuestro cariño, vuestras palabras o vuestros silencios, vuestras miradas que me aseguran que no estoy sola. Aunque no seáis conscientes de esto, todos y cada uno de vosotros me habéis aportado algo importante, y lo mejor de todo, es que hemos podido compartir juntos una época inolvidable. Habéis sido (y sois) una gran compañía de valor incalculable, porque no se puede tener más suerte de teneros cerca. Gracias, gracias y gracias por ser tan grandes y por estar tanto para los momentos buenos, como para los no tan buenos.

Mis epis, ¿Qué haría yo sin mis epis? Porque los abrazos de Nuria son medicina indispensable cuando las cosas se tuercen, o simplemente cuando hace falta porque sí. Igual que la buena compañía de Almu en cultivos o los momentos con Eva, compartiendo gustos musicales con sus peques y recibiendo todo su cariño siempre. Porque tampoco hubiera sido lo mismo sin las conversaciones intensas sobre la vida con "el mae", o las pizzas con Fran peque a las 22h cuando ya no queda nadie en el laboratorio y nos da por bailar salsa choke (ahora que nadie nos ve).

Lo que tampoco puede faltar es la sonrisa del chico más alegre que me he cruzado nunca: Parki. Él nunca deja de sonreír y regala cariño y alegría allá donde va (aparte de una lista increíble con los últimos temas musicales). Jose, gracias por todos tus ánimos, por tus abrazos y por transmitir ese buen rollo que levanta el ánimo a cualquiera. Mucha, muchísima suerte en tu nueva etapa.

Vic, mi "Vihtoria" (léase con acento pacense). Otra de las grandes sonrisas y pilares importantes en estos años. Gracias, amiga, por tantas horas de confianzas, por tu cariño, por tu espontánea sinceridad, por ser "TÚ" con letras mayúsculas. Por compartir tus preocupaciones, ilusiones y sueños conmigo. De aquí al infinito "marichocho".

Y, aunque no haga caso a nada de lo que me dice, también han sido muy necesarios los grandes y sabios consejos de "Carre". Fuiste la primera cara que conocí y que me dio la oportunidad de estar aquí. Gracias a mi Garci (otra vez) por ser mucho más que una directora, una amiga. A María, la gallega preferida. Por todas las conversaciones (real time, doy fe), y por tu ayuda y tu cariño cuando más lo he necesitado. A Ángeles y Rodolfo por todas vuestras enseñanzas y por la mano que me habéis echado para sacar esto adelante. A Fernando, por acogerme desde el principio con los brazos abiertos y preocuparte porque todo me vaya bien (y por los dulces argentinos tan ricos que nos traes de vez en cuando).

Blanca... la jefa (también wikijefa) se merece otro párrafo aparte. Ella es la persona que está siempre. Es la mano que te ayuda cuando lo necesitas, es la palabra que te saca sonrisas siempre que hace falta. Es el oído que te escucha cuando necesitas contar algo (y que también te pilla imitando sonidos aleatorios cuando piensas que nadie te oye). Siempre dispuesta, para todo y para todos. GRA-CIAS.

Lo mejor de todo esto es que fuera de esas cuatro paredes que han sido mi casa durante estos años, me sigo sintiendo afortunada por las personas excepcionales que están cerca de mí, y de las que aprendo cada día.

Empezando por mis "Ángeles de Izzy" (Patri, Susana, Izzy...auténticos 100%) y siguiendo por mis "Ponchos", Patri y Aroa. Porque nos quedan muchos trenes que coger y lugares por descubrir, muchas bachatas, grullas y ataques de risa por sufrir. Aquí, en Milano o donde sea, ma ... sempre insieme ragazze. A mi amigo Jose por ser mi consejero espiritual y compañero de aventuras desde la más tierna infancia, por hacerme saber que estás conmigo, aunque no te vea.

A la pequeña gran familia "Solmusic", porque me alegra compartir con vosotros nuestra gran pasión. Sois los mejores compañeros de escenario y de ilusiones que se puede tener. Aroa, contigo la aventura empezó en "Nunca Jamás" y nos llevará volando allá donde seamos capaces de imaginar. Gracias por compartir tu polvo de hadas conmigo. Juan Ángel, mi gran amigo, maestro y guía fuera y dentro de la música. Gracias por crear mucho más que una escuela, una gran familia, por enseñarme y por disfrutarlo con nosotros. Por estar siempre y regalarnos tu cariño, tu alegría y ¡tu locura! Gabriel, "no comments". Soy feliz de que compartamos nuestros pensamientos, ilusiones y reflexiones vitales y que, como dice la canción, "no importe la distancia". Sé que algún día tendré que comprar entradas muy caras para verte brillar en el escenario de un gran teatro. Mis mejores deseos para ti.

A mi piano y a mis cuerdas vocales, por ser capaces de expresar lo que yo no sé decir con palabras. "Porque la vida sin música sería un error".

Bianca y Maira. Las bonitas casualidades siempre ocurren por algo. Ya sabéis que sois dos de mis grandes pilares. Por sacar lo mejor de mí. Por quererme como soy. Por ser y estar. Por todo lo que me enseñáis cada día. Gracias al escritor por todo esto, pero, sobre todo, gracias a vosotras por decidir vivirlo conmigo.

Cristina. Doctora Segovia, mi Crismaitía. Eres de esas personas que dejan huella. De las que de verdad “ven” dentro de los demás. De las que te recuerdan que, pase lo que pase, podemos con todo. Eres uno de los grandes tesoros que he tenido la suerte de encontrar en la vida. Pero tú y yo sabemos que los lazos de verdad no se describen con palabras, no se ven. Se sienten y se cuidan. Juntas empezamos este camino, y juntas lo continuaremos. ¡Vamos a por todo lo que nos queda por vivir!

A mi familia Llamazares, desde Madrid hasta León. Por todo vuestro apoyo, vuestra ayuda y por quererme desde el principio como una más. (Y por esas tortillas de patata con pan de leña hechos con tanto cariño).

Ángel. Da igual que llueva, nieve, truene, venga una pandemia o nos secuestren los alienígenas. Siempre consigues que todo sea más fácil. Gracias por ser mi compañero de locuras y de ilusiones, de caminos de barro y bailes de etiqueta, de conversaciones profundas y abrazos de recarga. Por ser mi ingeniero y psicólogo de guardia. Por tu gran corazón. No tengo palabras para ti, no sería suficiente. GRACIAS.

Javi, tú eres “mi pensamiento alegre”. Mi cabo suelto, mi cómplice, mi paño de lágrimas, mi manantial de carcajadas y mi tesoro más preciado. Me quedaré corta con cualquier cosa que te diga. Así que sólo te diré lo orgullosa que estoy de tener un hermano como tú, en todos los sentidos que puedas imaginar. Eres muy grande Javi. Te mereces lo mejor y lo conseguirás.

A mis padres. Vosotros sois la verdadera razón de que hoy pueda estar escribiendo todo esto. Por vuestro sacrificio y cariño incondicional. Por ayudarme a cumplir mis sueños, por enseñarme, cuidarme y acompañarme pase lo que pase. Vosotros habéis hecho posible que yo sea lo que quiera ser, habéis hecho “fácil” que yo pueda lograr mis metas. Me habéis hecho una persona inmensamente feliz. Porque si se pudiera elegir, os volvería a elegir a vosotros.

“Nadie consigue algo importante completamente solo”.

TABLE OF CONTENTS

TABLE OF CONTENTS	I
LIST OF FIGURES	IV
LIST OF TABLES	VII
LIST OF ACRONYMS	VIII
1 ABSTRACT/RESUMEN	3
2 GENERAL INTRODUCTION	7
2.1 THE SKIN	9
2.1.1 <i>Function and structure</i>	9
2.1.2 <i>Epidermis</i>	10
2.2 CYTOSKELETON	12
2.2.1 <i>Extracellular matrix molecules</i>	12
2.3 CELL JUNCTIONS.....	13
2.4 CELL MIGRATION	20
2.5 SINGLE CELL MIGRATION	20
2.6 COLLECTIVE CELL MIGRATION.....	22
2.7 MECHANOBIOLOGY	24
2.8 FORCES INVOLVED IN CELL MOTION	25
2.9 MEASUREMENT OF CELLULAR FORCES.....	29
2.10 WOUND HEALING.....	31
2.11 WOUND HEALING PROCESS	31
2.11.1 <i>Hemostasis and coagulation</i>	32
2.11.2 <i>Inflammation</i>	33
2.11.3 <i>Proliferation</i>	33
2.11.4 <i>Remodeling</i>	34
2.12 MECHANICAL FORCES IN WOUND HEALING AND SKIN FRAGILITY DISORDERS	34
3 JUSTIFICATION AND OBJECTIVES	43
3.1 JUSTIFICATION	45
3.2 OBJECTIVES.....	45
3.3 GENERAL AIM	45
3.4 SPECIFIC AIMS.....	45

4	MEASUREMENT OF FORCES EXERTED BY MIGRATING HACAT CELLS AND FORMULATION OF THE MODEL.....	47
4.1	STATE OF THE ART	49
4.2	MOTIVATION.....	51
4.3	METHODOLOGY	52
4.4	MATERIALS AND METHODS	53
4.5	CELL CULTURE.....	53
4.6	EXPERIMENTAL SETUP	54
4.6.1	<i>Time-lapse experiments.....</i>	<i>56</i>
4.6.2	<i>Image Analysis and velocity measurements.....</i>	<i>57</i>
4.7	RESULTS	58
4.8	MEASUREMENTS OF FORCES EXERTED BY MIGRATING HACAT CELLS.....	58
4.9	MODEL FORMULATION.....	63
4.9.1	<i>Terms of the fiber-monolayer system equation.....</i>	<i>67</i>
4.9.2	<i>Boundary conditions.....</i>	<i>68</i>
4.10	THEORETICAL VS. EXPERIMENTAL OBSERVATIONS	70
4.11	DISCUSSION	75
5	EFFECT OF THE CARBON FIBER ON ACTIN CYTOSKELETON REARRANGEMENTS AND CADHERIN-MEDIATED CELL-CELL ADHESION.....	83
5.1	ADHERENS JUNCTIONS MECHANOSENSING AND CYTOSKELETAL REARRANGEMENTS IN MIGRATING CELLS 85	
5.2	MATERIALS AND METHODS	87
5.3	CELL CULTURE AND EXPERIMENTAL SETUP	87
5.4	IMMUNOCYTOCHEMISTRY	87
5.5	BEHAVIOR OF THE CELL MONOLAYER UPON MEETING THE FIBER	90
5.6	INFLUENCE OF THE FIBER ON E-CADHERIN-MEDIATED CELL-CELL ADHESION.....	91
5.6.1	<i>Influence of the fiber on actin cytoskeleton rearrangement</i>	<i>96</i>
5.7	DISCUSSION	104
6	GENERATION OF KINDLIN-1 DEFICIENT CELLULAR MODEL FOR FORCE MEASUREMENT EXPERIMENTS 113	
6.1	KINDLER SYNDROME	115
6.2	KINDLIN- 1 PROTEIN STRUCTURE	116
6.3	RELEVANCE OF KINDLIN IN MECHANOTRANSDUCTION AND WOUND HEALING	118
6.4	MOTIVATION AND METHODOLOGY	119
6.5	CRISPR/Cas9 GENE EDITING SYSTEM	119
6.6	MATERIALS AND METHODS.....	121

6.7	IMMORTALIZED HUMAN KERATINOCYTES (HKE6E7)	121
6.8	CRISPR/CAS9 SYSTEM AND NUCLEOFECTION	121
6.9	ISOLATION OF EDITED CLONES	122
6.10	NUCLEIC ACID EXTRACTION	123
6.11	RNA REVERSE TRANSCRIPTION (cDNA OBTENTION).....	124
6.12	DNA FRAGMENT AMPLIFICATION.....	124
6.13	CLONING OF PCR PRODUCTS	126
6.14	SEQUENCING ANALYSIS	126
6.15	CELLULAR PROTEIN EXTRACTION	127
6.16	ANALYSIS OF PROTEIN EXPRESSION BY WESTERN BLOTTING.....	127
6.17	KINDLIN-1 DETECTION BY IMMUNOCYTOCHEMISTRY.	128
6.18	CHARACTERIZATION OF GENERATED KINDLIN-1 DEFICIENT CELLULAR MODEL.....	129
6.19	FORCE MEASUREMENTS IN KINDLIN-1 DEFICIENT CELLS.....	136
6.20	DISCUSSION	146
7	FUTURE PERSPECTIVES.....	155
7.1	FUTURE WORK.....	157
8	CONCLUDING REMARKS.....	163
8.1	CONCLUSIONS	165

LIST OF FIGURES

FIGURE 2.1. SECTIONAL VIEW OF SKIN STRUCTURE	9
FIGURE 2.2. SCHEMATIC REPRESENTATION OF SKIN LAYERS.	11
FIGURE 2.3. SCHEMATIC REPRESENTATION OF TYPES OF CELL JUNCTIONS AND PROTEINS INVOLVED IN CELL ADHESIONS.	16
FIGURE 2.4. GENERAL REPRESENTATION OF SOME OF THE MOLECULES INVOLVED IN THE FOCAL ADHESION (FA) COMPLEX..	19
FIGURE 2.5. SCHEMATIC REPRESENTATION OF CELL MOVEMENT STAGES.	21
FIGURE 2.6. POLARIZATION OF LEADER CELLS IN COLLECTIVE	24
FIGURE 2.7. CYTOSKELETAL STRUCTURES.....	26
FIGURE 2.8. FOCAL ADHESIONS AS MOLECULAR CLUTCHES	28
FIGURE 2.9. TRANSMISSION OF CELLULAR FORCES DURING CELL MIGRATION.....	29
FIGURE 2.10. SCHEMATIC REPRESENTATION OF SOME FORCE SENSING TECHNIQUES.....	30
FIGURE 4.1. SCHEMATIC REPRESENTATION OF THE METHOD.....	52
FIGURE 4.2. DESIGNED OF THE 3D PRINTED STENCIL FOR REGULAR TIME LAPSE EXPERIMENTS.....	54
FIGURE 4.3. STEPS FOR CARBON FIBER POSITIONING UNDER MICROSCOPE.....	55
FIGURE 4.4. STENCIL POSITIONING.....	56
FIGURE 4.5. EVOLUTION OF THE WOUND HEALING ASSAY AT DIFFERENT TIMES	58
FIGURE 4.6. FITTING CORRESPONDING TO A FIBER LENGTH = 4MM AT TIME 52,61H.....	59
FIGURE 4.7. TIME EVOLUTION OF THE UNIFORM FORCE PER UNIT LENGTH FOR DIFFERENT FIBER LENGTHS	60
FIGURE 4.8. WOUND HEALING ASSAY AT TIME = 0. L = 3MM	60
FIGURE 4.9. KYMOGRAPHS.....	61
FIGURE 4.10. MIGRATING CELL MONOLAYER FIXED AT TIME = 48H	62
FIGURE 4.11. CELL DENSITY ANALYSIS OF FIGURE 4.10. (NUMBER OF CELLS/MM ²)	63
FIGURE 4.12. DAMPED HARMONIC OSCILLATION	64
FIGURE 4.13. DAMPED HARMONIC MOTION. OVERDAMPED	65
FIGURE 4.14. FIBER-MONOLAYER SYSTEM PROGRESSION OVER TIME	66
FIGURE 4.15. EXPERIMENTAL VS. MODEL RESULTS	70
FIGURE 4.16. SCHEMATIC REPRESENTATION. L_c AND $-l$	72
FIGURE 4.17. MAXIMUM FORCE MEASURED IN EXPERIMENTS CORRESPONDING TO DIFFERENT FIBER LENGTHS.....	74
FIGURE 4.18. MAXIMUM FIBER DEFLECTION AS A FUNCTION OF THE MAXIMUM FORCE.....	75
FIGURE 5.1. ENGAGED ADHERENS JUNCTION	86
FIGURE 5.2. 3D PRINTED STENCIL FOR ICC ASSAYS.	88
FIGURE 5.3. SCHEMATIC REPRESENTING THE NOTATION USED FOR IMMUNOFLUORESCENCE ANALYSIS.	89
FIGURE 5.4. DAPI STAINING OF MIGRATING CELLS OVERPASSING THE FIBER	90
FIGURE 5.5. E-CADHERIN CELL-CELL ADHESION STAINING.	91
FIGURE 5.6. ZOOM ON C AND D REGIONS OF FIGURE 5.5.	92

FIGURE 5.7. E-CADHERIN CELL-CELL STAINING OF THE CELLS AT THE WOUND EDGE.	93
FIGURE 5.8. E-CADHERIN CELL-CELL ADHESION STAINING (72H)	94
FIGURE 5.9. ZOOM ON REGIONS 1, 2 AND 3 OF FIGURE 5.8	95
FIGURE 5.10. ACTIN CYTOSKELETON STAINING (72H)	97
FIGURE 5.11. ZOOM ON D, E AND F REGIONS OF FIGURE 5.10	98
FIGURE 5.12. ACTIN CYTOSKELETON STAINING OF THE CELLS AT THE WOUND EDGE.	99
FIGURE 5.13. ZOOM ON E AND F REGIONS OF FIGURE 5.11	100
FIGURE 5.14. ACTIN CYTOSKELETON STAINING (72H)	101
FIGURE 5.15. ZOOM IN ON D, E AND F REGIONS OF FIGURE 5.14.....	102
FIGURE 5.16. ACTIN CYTOSKELETON LABELLING AND E-CADHERIN IMMUNOFLUORESCENCE (72H)	103
FIGURE 6.1. KINDLIN-1 PROTEIN DOMAINS.....	117
FIGURE 6.2. A. GENERAL REPRESENTATION OF SOME OF THE MOLECULES INVOLVED IN THE FOCAL ADHESION (FA) COMPLEX	117
FIGURE 6.3. CRISPR/Cas9 SYSTEM	120
FIGURE 6.4. SCHEME OF CRISPR/Cas9 COMPLEX.....	122
FIGURE 6.5. GENOMIC DNA CHROMATOGRAM OF WILD TYPE IMMORTALIZED HUMAN KERATINOCYTES (HKE6E7).....	130
FIGURE 6.6. PCR ANALYSIS FOR HOMOZYGOUS CLONES FOR E6 DELETION	131
FIGURE 6.7. FERMT1 EXPRESSION ANALYSIS IN HKE6E7 Δ E6 CELLS.....	132
FIGURE 6.8. KINDLIN-1 EXPRESSION ANALYSIS OF HKE6E7 Δ FERMT1 CELLS.....	132
FIGURE 6.9. GENOMIC DNA SANGER SEQUENCING.	133
FIGURE 6.10. cDNA SANGER SEQUENCING.....	134
FIGURE 6.11. MORPHOLOGICAL ANALYSIS OF HKE6E7 Δ E6 CELLS.....	135
FIGURE 6.12. KINDLIN-1 EXPRESSION IN HKE6E7 Δ E6 KERATINOCYTES.....	136
FIGURE 6.13. HAcat VS. KIN1 ⁻ CELLS. TIME EVOLUTION OF THE UNIFORM FORCE PER UNIT LENGTH FOR DIFFERENT FIBER LENGTHS.....	137
FIGURE 6.14. MAXIMUM FORCE MEASURED IN EXPERIMENTS CORRESPONDING TO DIFFERENT FIBER LENGTHS.	138
FIGURE 6.15. MAXIMUM FIBER DEFLECTION AS A FUNCTION OF THE MAXIMUM FORCE)	139
FIGURE 6.16. TIME EVOLUTION OF MIGRATING HAcat AND KIN1 ⁻ CELLS (WITHOUT FIBER).....	140
FIGURE 6.17. COMPARISON BETWEEN HAcat AND KIN1 ⁻ CELLS MIGRATING FRONT (WITH FIBER)	141
FIGURE 6.18. KYMOGRAPHS CORRESPONDING TO FIGURE 6.16.	142
FIGURE 6.19. PIV ANALYSIS OF KIN1 ⁻ CELLS AT TWO DIFFERENT TIMEPOINTS.....	143
FIGURE 6.20. PIV ANALYSIS (TIME= 15H). COMPARISON BETWEEN HAcat AND KIN1 ⁻ CELLS.....	144
FIGURE 6.21. KYMOGRAPHS (KIN1 ⁻ CELLS).....	145
FIGURE 7.1. SCHEMATIC REPRESENTATION OF THE DIFFERENTIATION PROCESS OF AN ORGANOTYPIC SKIN CULTURE.	157
FIGURE 7.2. ORGANOTYPIC CULTURES FOR IN VITRO STUDIES.	158
FIGURE 7.3. SCHEMATIC REPRESENTATION OF THE 3D CELL TRACKING EXPERIMENTAL PROCEDURE PROPOSED..	158
FIGURE 7.4. PRELIMINARY RESULTS OF 3D CELL TRACKING IMAGING.....	159

FIGURE 7.5. SKETCH OF A CARBON FIBER IMMERSSED IN A DEVELOPING ORGANOTYPIC SKIN CULTURE DURING DIFFERENTIATION
PROCESS..... 160

FIGURE 7.6. SCHEMATIC REPRESENTATION OF THE EXPERIMENTAL SETUP FOR ATP:ADP RATIO ANALYSIS.. 161

LIST OF TABLES

TABLE 2.1. CELL- ECM JUNCTIONS:	14
TABLE 2.2. CELL-CELL JUNCTIONS.	15
TABLE 2.3. "FIGURE 2.3" LEGEND.....	17
TABLE 2.4. FORCE MEASUREMENT TOOLS.....	31
TABLE 2.5. CONCEPT MAP OF WOUND HEALING PROCESS.	32
TABLE 4.1. REFERENCES AND DILUTIONS FOR PHALLOIDIN, PRIMARY AND SECONDARY ANTIBODIES.	88
TABLE 6.1. GRNAs DESIGNED TO TARGET EXON 6 FROM FERMT1.	121
TABLE 6.2. PRIMERS FOR RT- PCR.....	124
TABLE 6.3. PRIMERS FOR PCR.....	125
TABLE 6.4. PCR REAGENTS.	125
TABLE 6.5. GENERAL CONDITIONS FOR PCR AMPLIFICATION	126
TABLE 6.6. PRIMARY ANTIBODIES FOR WB.	128
TABLE 6.7. SECONDARY ANTIBODIES FOR WB.	128

 LIST OF ACRONYMS

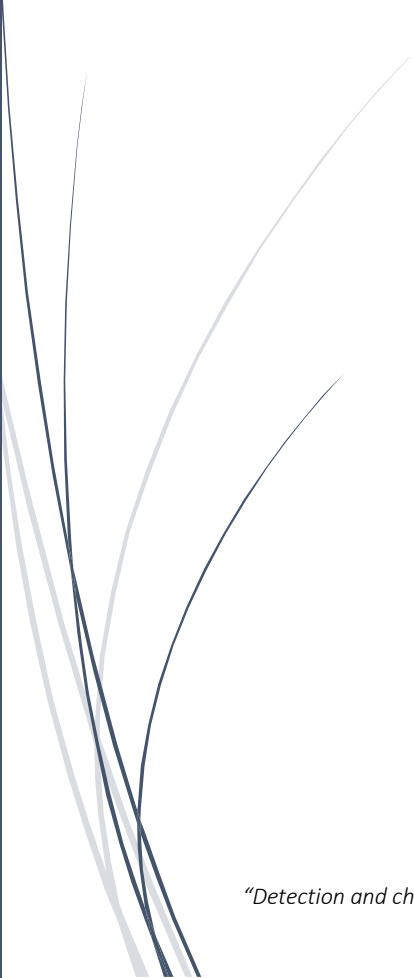
3D	Three dimensional
Ab	Antibody
ABPs	Actin Binding Proteins
AFM	Atomic force microscopy
AJ	Adherens junction
AMPs	Antimicrobial Peptides
BC	Bent- closed (integrin conformation)
BM	Basement membrane
BSA	Bovine serum albumin
cDNA	Complementary DNA
CIL	Contact Inhibition of Locomotion
CRISPR	Clustered regularly interspaced short palindromic repeats
CU	Contractile Unit
DAB	3,3'-Diaminobenzidine
DMEM	Dulbecco's Modified Eagle Medium
DMSO	Dimethyl sulfoxide
dNTP	Deoxynucleotide triphosphate
DSBs	Double-stranded breaks
EB	Epidermolysis bullosa
EC	Extended-closed (integrin conformation)
ECM	Extracellular matrix
EDTA	Ethylenediamine tetraacetic acid
EGFR	Epidermal growth-factor receptor
EO	Extended-opened (integrin conformation)
F	Forward (Primer)
FA	Focal adhesion
FBS	Fetal bovine serum
FC	Focal Contacts
<i>FERMT1</i>	Fermitin family member 1 gene
FRET	Fluorescence resonance energy transfer
GAG	Glycosaminoglycans
gDNA	Genomic DNA
gRNA	Guide RNA
HaCat	Human spontaneously immortalized epithelial keratinocytes
HEK	Human Embryonic Kidney cells
HK	human keratinocytes
HKE6E7	Human immortalized keratinocytes
HPV16	Human Papillomavirus
ICC	Immunocytochemistry

IF	Intermediate filaments
IFE	Interfollicular Epidermis
IHC	Immunohistochemistry
ILK	Integrin linked kinase
IPP	ILK–PINCH–parvin
JAM	Junctional Adhesion Molecule
K1/K10	Cytokeratin 1 and cytokeratin 10
K5/K14	Cytokeratin 5 and cytokeratin 14
KDM	Keratinocyte differentiation medium
KGM	Keratinocyte Growth medium
KS	Kindler Syndrome
KSM	Keratinocyte Seed medium
MMPs	Metalloproteinases
mRNA	messenger RNA
NHEJ	Non-homologous end joining
NPWT	Negative pressure wound therapy
O/N	Overnight
PAM	Protospacer Adjacent Motif
PBS	Phosphate Buffer Saline
PCR	Polymerase Reaction Chain
PH	Plekstrin Homology
PLA	Polylactic acid
PTB	Phosphotyrosine binding site
Q.S	Quantum Statis (enough amount to reach an specific volume)
R	Reverse (primer)
RT- PCR	Reverse transcription- Polymerase Chain Reaction.
SC	Stratum corneum
TA cloning	Thymidine-adenine cloning
TFM	Traction force microscopy
TIMPS	Tissue inhibitors of metalloproteinases
Tm	Melting temperature
UJT	Unjammed transition
WB	Western Blot



1 Abstract/Resumen

*“Solo chi sogna può volare”
(J.M. Barrie)*



“Detection and characterization of mechanical forces and dynamic molecular rearrangements in collective cell migration” – Verónica López

Mechanobiology studies the interplay between the cell and its environment to correlate cellular functions with physical forces. Cells have the ability to exert active forces on their surroundings and, in turn, are able to sense and respond to changes in mechanical properties of the extracellular matrix. This bi-directional communication controls many relevant biological processes, such as morphogenesis, tissue repair or cell migration, proliferation, and differentiation. Dysregulation of these highly coordinated mechanisms, results in the appearance of pathological processes such as cancer invasion, chronic wounds, or skin fragility disorders.

The inherent difficulty in measuring certain physical quantities such as force, in a biological system, has meant that most advances in this field are due primarily to a deeper knowledge of the biochemical processes that govern these mechanisms. A full understanding of mechanobiology, however, requires a combined study of biological and physical phenomena.

In this regard, a variety of techniques have been developed that have provided us with qualitative and quantitative data on the kinematics and dynamics of cell behavior. These methods in turn, are often complemented by theoretical models that decipher and predict biological behavior based on the laws of physics. Nevertheless, in the context of an organism, most tissues acquire a three-dimensional structure, so there is a need for these measurement techniques to be applicable to 3D environments. Much remains to be developed and improved in this direction, as 3D measurement techniques still present many difficulties.

The present thesis reports the development of a new 2D force measurement technique based on a flexible structure of known mechanical properties. This cantilever-based force sensor is deformed by epidermal keratinocytes as they migrate, in a wound healing experimental setup. The resultant deflection of the structure is detected over time by image analysis to infer the forces exerted by the cells. According to the results obtained, an active fluid based theoretical model was formulated that represents the fundamental characteristics of the system and predicts the evolution of its behavior.

Thereby, we established a reproducible, easy to implement and affordable 2D force measurement tool. On the other hand, the proposed theoretical model, collects the essential ingredients needed to describe how a multicellular tissue modulates the force it exerts depending on the compliance of its external surroundings. One of its most advantageous features is that its reduced complexity allows for easier interpretation and possible incorporation into other more complex models.

This measurement technique was subsequently tested in a Kindler syndrome cellular model, which was generated using the CRISPR/Cas9 tool to produce the loss of kindlin-1 expression. The results obtained showed that, in our specific context, the force measurement tool is sensitive enough to detect a difference between the forces and mechanical work exerted by healthy cells and those exerted by cells exhibiting poor adhesion to the substrate.

Furthermore, we also studied the distribution of the cytoskeleton and cell adhesions of the migrating monolayer when interacting with the force sensor, to characterize how cells respond to this experimental environment.

Future perspectives focus on a deeper molecular and metabolic characterization of the cellular responses upon interaction with a compliant body and the adaptation of the force sensor to a 3D environment.

RESUMEN

La mecanobiología estudia la interacción entre la célula y su entorno para correlacionar las funciones celulares con las fuerzas físicas. Las células tienen la capacidad de ejercer fuerzas activas sobre su entorno y, a su vez, son capaces de percibir y responder a los cambios en las propiedades mecánicas de la matriz extracelular. Esta comunicación bidireccional controla muchos procesos biológicos relevantes, tales como la morfogénesis, la reparación de tejidos o la migración, proliferación y diferenciación celular. La desregulación de estos mecanismos altamente coordinados conduce a la aparición de estados patológicos como las heridas crónicas, procesos invasivos en el desarrollo del cáncer o trastornos de fragilidad de la piel, entre otros.

La dificultad que conlleva la medida de ciertas magnitudes físicas como la fuerza en un sistema biológico, ha supuesto que los avances en este campo se hayan debido fundamentalmente a una mayor profundización en el conocimiento de los procesos bioquímicos que gobiernan estos mecanismos. Sin embargo, para llegar a una comprensión completa de la mecanobiología, se requiere un estudio conjunto de los fenómenos biológicos y físicos que están involucrados. En este sentido, se han desarrollado una gran variedad de técnicas que proporcionan datos cualitativos y cuantitativos sobre la cinemática y la dinámica de los comportamientos celulares. Estos métodos a su vez se suelen complementar con modelos teóricos que, basándose en las leyes de la física, descifran y predicen el comportamiento biológico. No obstante, en los organismos, la mayoría de los tejidos adquieren una estructura tridimensional, por lo que es necesario que estas técnicas de medición puedan aplicarse a entornos 3D. En este sentido, todavía hay un amplio recorrido de desarrollo y mejora, ya que las técnicas de medición en 3D siguen presentando muchas dificultades.

En el presente trabajo se expone el desarrollo una nueva técnica de medición de fuerzas en 2D, basada en una estructura flexible de propiedades mecánicas conocidas. Este sensor de fuerza es deformado por células epidérmicas (queratinocitos), a medida que migran hacia adelante. La deflexión

producida en la estructura se detecta a lo largo del tiempo mediante análisis de imagen, para inferir las fuerzas ejercidas por las células. De acuerdo con los resultados obtenidos, se formuló un modelo teórico basado en fluidos activos que representa las características fundamentales del sistema y predice la evolución de su comportamiento.

De este modo, hemos desarrollado una herramienta de medición de fuerzas en entornos biológicos bidimensionales que es fácil de reproducir e implementar y de coste reducido en comparación con otras técnicas. Por otro lado, el modelo teórico propuesto, reúne los ingredientes esenciales necesarios para describir cómo una monocapa de células migratorias modula las fuerzas que ejerce en función de la rigidez de su entorno. Una de sus características más ventajosas de este modelo, es que su reducida complejidad permite una interpretación más fácil y su posible incorporación a otros modelos más complejos.

La técnica de medición fue posteriormente testada en un modelo celular de síndrome de Kindler que generamos utilizando la herramienta CRISPR/Cas9 para producir la pérdida de expresión de kindlina-1. Los resultados obtenidos confirmaron que, en nuestro contexto específico, la herramienta de medición es lo suficientemente sensible como para detectar una diferencia entre las fuerzas y el trabajo realizado por células sanas y las ejercidas por células que presentan una deficiencia de adhesión al sustrato.

Además, también se estudió la distribución del citoesqueleto y adhesiones celulares de la monocapa migratoria al interactuar con el sensor de fuerza, para caracterizar cómo responden las células a este entorno experimental.

Las perspectivas futuras se dirigen hacia una caracterización molecular más profunda de las respuestas celulares al interactuar con un cuerpo externo flexible y hacia la adaptación del sensor de fuerza a un entorno 3D.



2 General introduction

*“A scientist in the laboratory
is also a child confronting natural phenomena
that impress him as though they were fairy tales”.*
(Marie Curie).

*“Detection and characterization of mechanical forces and dynamic molecular rearrangements in collective
cell migration” – Verónica López*

2.1 The skin

2.1.1 Function and structure

The skin is the largest organ in the body constituting 15–20% of total body weight. It is a metabolically active organ and one of its main functions is to act as a defensive barrier against environmental factors such as microorganisms, UV radiation and biological, chemical and physical agents. Moreover, the skin is responsible for maintaining body homeostasis, preventing dehydration and regulating temperature. It also plays an important role as a sensory organ and in the generation of the immune response^{1,2}. The skin is comprised of three main layers: epidermis, dermis and hypodermis (subcutaneous layer).

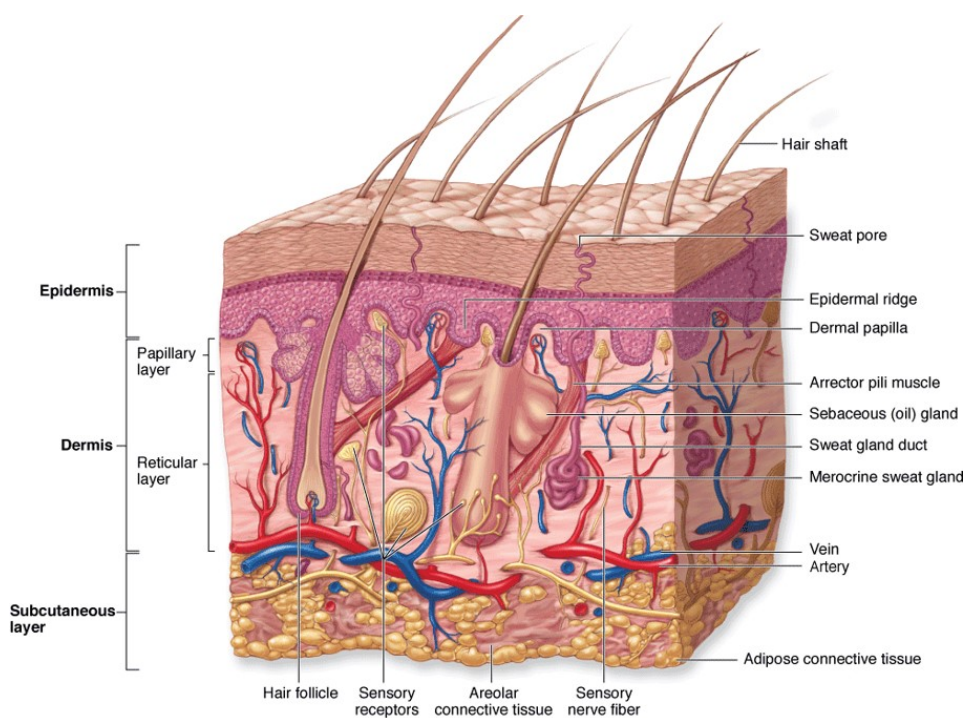


Figure 2.1. Sectional view of skin structure. From Junqueira's. Text and atlas. 12th edition³.

Besides, the skin along with specialized glands, nerve, hair and nail, form the integumentary system, covering all our body and carrying out the different functions described above (Figure 2.1).

2.1.2 Epidermis

The epidermis is the outermost layer of the skin and has an ectodermal origin. It is a stratified and dynamic self-renewing tissue which lacks blood vessels and is dependent on the vascularization of the dermis for its nutrition, oxygenation and excretion of metabolites⁴. The epidermis is made up of four types of cells:

- **Keratinocytes**, which makes up 90% of the epidermis.
- **Melanocytes**, responsible of melanin production. Melanin is a pigment that is able to absorb radiation and free radicals from UV light. It confers a dark color to the skin and protects it against UV radiation⁵.
- **Langerhans cells** are a type of dendritic cells which play a role in the immune response. They are located at the basal and suprabasal layers of the epidermis and act as antigen presenters to T lymphocytes⁶.
- **Merkel cells**, that are slowly adapting mechanoreceptors involved in tactile sensitivity^{7,8}.

The thickness of the epidermis depends on the region and varies from 0.05 mm (on the eyelids) to 1.55mm (on the palms and soles) and is divided into four layers⁹ : *stratum basale*, *stratum spinosum*, *stratum granulosum* and *stratum corneum* (Figure 2.2).

Skin undergoes a constantly self-renew throughout life keeping a precise equilibrium between cellular proliferation and differentiation (**skin homeostasis**). The *stratum basale* (the innermost layer of the epidermis) is composed of mitotically active keratinocytes, which secrete the ECM components of the basement membrane. Some of these cells are **stem cells**, which divide and originate other basal cells that stay in the *stratum basale*, and **transient-amplifying cells**, that migrate towards suprabasal layers as they proliferate and differentiate, thus forming the rest of the layers of the epidermis¹⁰. Moreover, cells endure biochemical changes through the sequential synthesis of different proteins and enzymes that characterize the stage of differentiation in which they are found, and therefore their location in a given stratum. This process ends with the formation of a **cornified envelope** which provide the skin with the ability to

function as a strong skin barrier, essential for skin permeability and water-loss prevention^{11,12,13}.

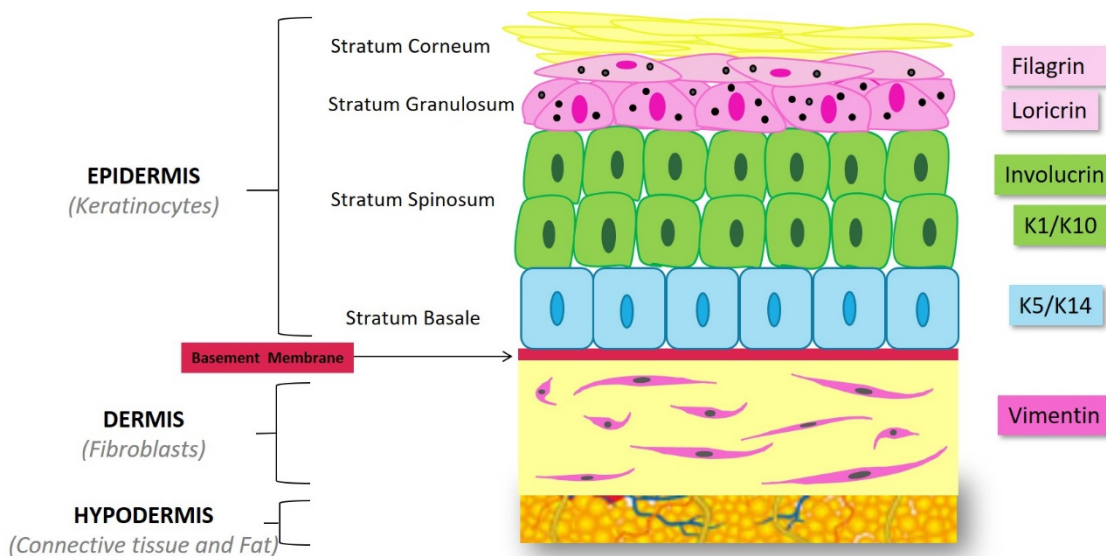


Figure 2.2. Schematic representation of skin layers. Epidermis. S. corneum (yellow), S. granulosum (pink), S. Spinosum (green) and S. basale (blue). **Basement membrane.** (dark red) Specialized ECM beneath the S. basale. **Dermis.** Fibroblasts (pink), ECM (yellow). **Hypodermis.** Connective tissue, fat, capillaries. **Proteins expressed at different layers.** Vimentin, K5/14, K1/10, involucrin, loricrin and filaggrin. *This is a self-created illustration.*

2.1.3 Dermis

The dermis is the thicker layer of the skin, a mesodermal derived connective tissue located between the epidermis and the hypodermis. It consists of **ECM populated with fibroblasts**, macrophages, and mast cells as well as nerve endings, blood vessels, hair follicles and sweat and sebaceous glands. The upper layer of the dermis (papillary dermis) presents rete ridges which helps the dermal-epidermal junction endure shear stress. Its main ECM components are loose and thin **type III and type I collagen fibers**, thus providing the skin with stress resistance. The lower region of the dermis (reticular dermis), is composed of thicker bundles of **collagen type I** arranged parallel to the skin surface and elastin fibers that confers the skin its elastic behavior.

Both collagen and elastic fibers secreted by fibroblasts, constitute the structural and nutritional support to the epidermis together with blood vessels^{2,4,10,14,15}.

2.1.4 Hypodermis

Below the dermis is the subcutaneous adipose tissue formed by adipocytes that make up a metabolically active tissue that protects the organisms providing cushioning and thermal isolation³.

2.2 Cytoskeleton

Cytoskeleton is a complex and dynamic network of protein filaments present in the cytoplasm of the cell. It helps to maintain the **cell shape**, gives the cell **mechanical resistance** to stress and it is involved in many processes such as cell division, intracellular transport, cell signaling and the **generation of forces** responsible for **cell migration**, among others.

There are three types of protein filaments forming the cytoskeleton: **actin filaments, microtubules and intermediate filaments (IF)**. Each one is made up of protein subunits (actin, tubulin and a family of fibrous proteins respectively) and confer different mechanical properties^{16,17}.

Actin and intermediate filaments are especially important in the structure of cellular junctions forming adhesion complexes together with other proteins to establish strong links with the surrounding ECM or neighbor cells (*See 2.6 Forces involved in cell motion*).

2.2.1 Extracellular matrix molecules

The extracellular matrix (ECM) constitute a dynamic structural and functional support for cells and tissues. Depending on its specific composition and spatial arrangement of its components, it confers different mechanical properties to the tissue adapting it to a variety of functional requirements. Cells are responsible of the secretion of this macromolecules and the interaction between them and its own ECM can affect several processes including cell proliferation, cell differentiation, cell migration, cell adhesion, tissue regeneration and repair. Also, the ECM plays an important role in cell signaling.

The ECM is made up of a mixture of five groups of macromolecules: collagen family, elastic fibers, glycosaminoglycans (GAG), proteoglycans (association of GAGs to a protein backbone) and adhesive glycoproteins. In the

case of skin, the ECM is more abundant in the dermis and scarce between the cells of the different layers of the epidermis^{18,19}.

The basement membrane (BM), also called basal lamina, is a specialized ECM which underlies beneath the basal cells of the epidermis, separating it from the dermis and providing structural support to the epithelium. Specifically, in skin the BM is composed mainly by **type IV collagen** and **type VII collagen** (the last one forms anchoring fibrils), glycoproteins such as **fibronectin** and **laminin**, **nidogen** and **proteoglycans** (heparan sulfate and perlecan)^{20,21}.

2.3 Cell junctions

Cells interact with molecules from ECM or from other cells, thus forming structurally organized tissues and organs. Keratinocytes are strongly attached to each other by cell-cell junctions, which maintain epidermal integrity and barrier function as well as participate in important dynamic processes as skin homeostasis, tissue morphogenesis, cell migration and wound healing.

These cell junctions are formed by a number of molecules as part of complex systems and allow cells to detect and react to the properties of its environment as they receive chemical and physical signals^{22,23}. In this section, we summarized the different types of cell junctions and molecules involved (*Table 2.1, Table 2.2, Figure 2.3, Table 2.3*).

	Name	Interaction	Elements involved
Cell-ECM	Focal Adhesion	Intracellular actin cytoskeleton with ECM through integrin heterodimer .	$\alpha\beta$ -Integrin heterodimer (<i>TM</i>) Actin cytoskeleton (<i>intracell.</i>) Collagen fibers (<i>ECM</i>) Some adaptor proteins (<i>intracell.</i>): <i>Talin</i> <i>Kindlin</i> <i>α-actinin</i> <i>Filamin</i> <i>Tensin</i> <i>FAK</i> <i>Vinculin</i> <i>Paxilin</i>
	Focal contact	A few intracellular actin fibers with ECM through integrin heterodimer .	$\alpha\beta$ -Integrin heterodimer (<i>TM</i>) Less actin fibers (<i>intracell.</i>) Collagen fibers (<i>ECM</i>) Adaptor proteins (<i>intracell.</i>): <i>Talin</i> <i>Tensin</i> <i>Vinculin</i> <i>Paxilin</i>
	Podosome	Intracellular actin cytoskeleton with ECM	Integrin (<i>TM</i>) Dense actin core MMPs
	Close contact	Blend between podosome and filopodia. Links actin with ECM through integrins.	Actin filaments Integrin Talin
	Hemidesmosome	Connect intracellular keratin intermediate filaments to ECM molecules of the basal layer through integrin .	Laminin (<i>ECM</i>) Integrin (<i>transmembrane</i>) Keratin (<i>intracell.</i>). Adaptor proteins: <i>Plectin</i> <i>BP180</i> <i>BP230</i>

Table 2.1. Cell- ECM junctions^{23,24,16,25}. *TM*. Transmembrane molecule. **Intracell.** Intracellular localization. **ECM**. Extracellular matrix. **MMPs**. Matrix metalloproteinases. **FAK**. Focal adhesion kinase.

	Name		Interaction	Elements involved
Cell-cell	Tight Junction		Connect actin cytoskeleton from both cells through a claudin-occludin link.	IgG Family of JAMS (junctional adhesion molecules). <i>Claudin- Occludin (TM)</i> <i>Actin</i>
	Cytoskeleton linked junctions	Adherens junction	Connect actin cytoskeleton from both cells through a cadherin-cadherin link.	E-Cadherin (<i>TM</i>) Actin cytoskeleton (<i>intracell.</i>) Linker proteins (<i>intracell.</i>): <i>p120cat</i> <i>α-catenina</i> <i>β-catenina</i>
		Desmosome	Connect keratin intermediate filaments from both cells through a desmoglein-desmocollin link.	Desmoglein-desmocollin (<i>TM</i>) Keratins (<i>intracell.</i>) Linker proteins (<i>intracell.</i>): <i>Plakoglobin</i> <i>Plakophilin</i> <i>Desmoglein</i>
	Gap junction		Transmembrane proteins which links both cells forming communicating channels between them.	Connexin (<i>TM</i>)

Table 2.2. Cell-cell junctions^{16,23,24}. *TM*. Transmembrane molecule. *Intracell.* Intracellular localization.

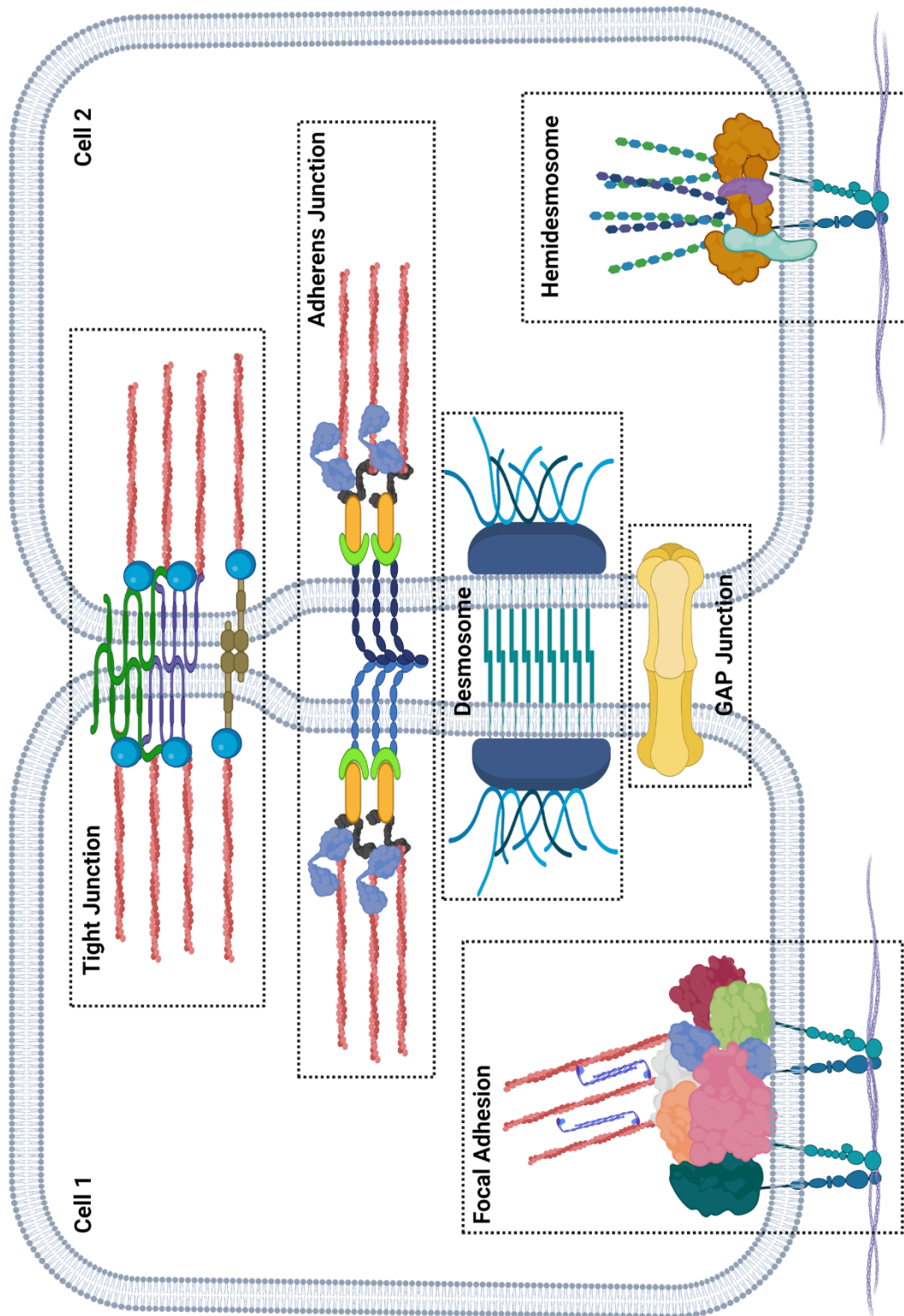


Figure 2.3. Schematic representation of types of cell junctions and proteins involved in these adhesions. From upper to lower side: Cell-cell junctions- Tight junction, Adherens junction, Desmosome, Gap junction. Cell-ECM junction: Focal adhesion, Hemidesmosome. LEGEND: next page. This is a self-created illustration, using www.Biorender.com.

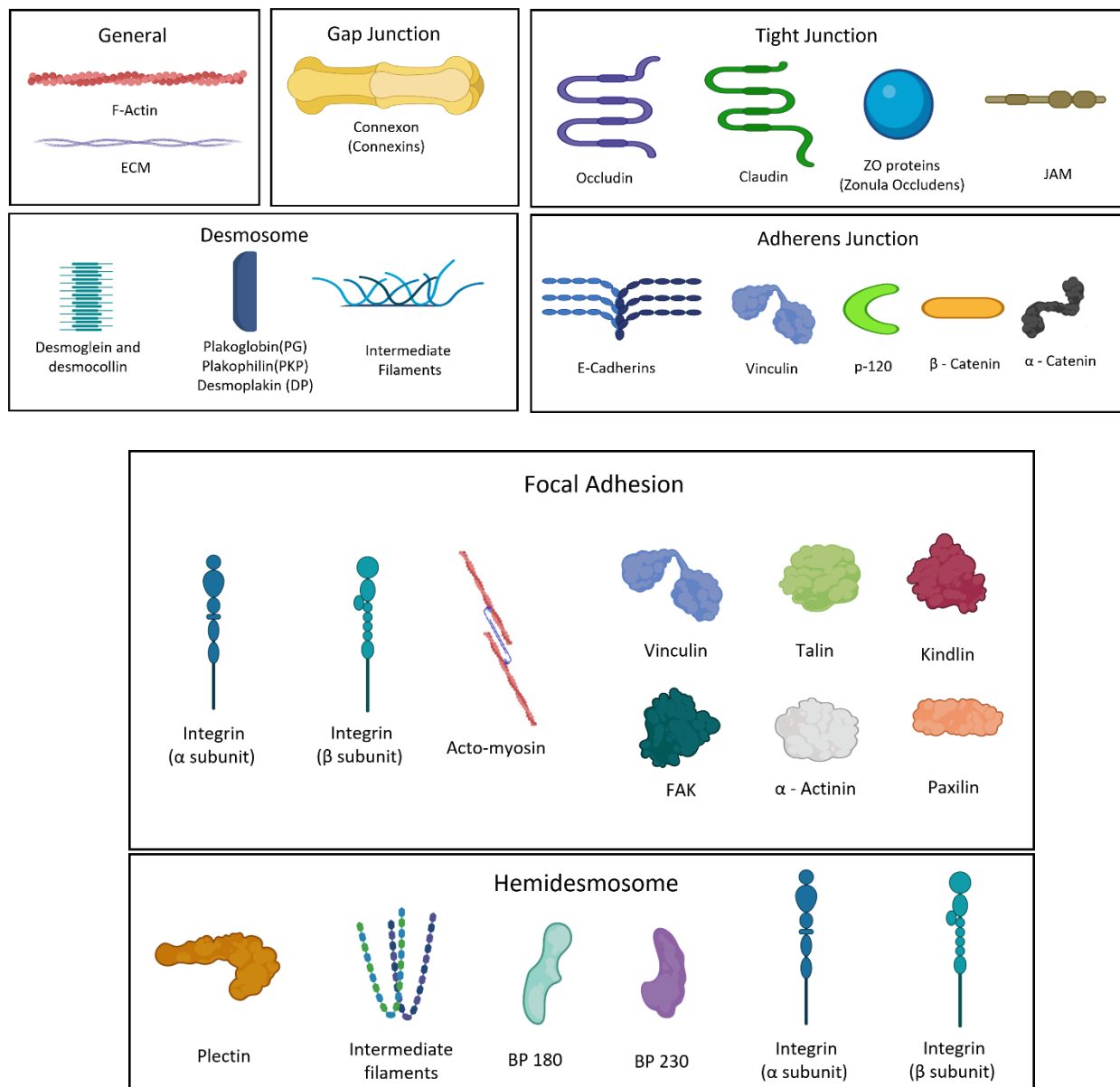


Table 2.3. "Figure 2.3" Legend. This is a self-created illustration, using www.Biorender.com

The most relevant cell junctions to consider in this work, will be adherens junctions (AJs cell-cell junctions) and focal adhesions (FAs) (cell-ECM integrin mediated adhesions). Their study will be used to characterize the interactions among migrating cells with the specific elements introduced in the experiments.

- **Focal Adhesions**

Focal adhesions (FAs) are dynamic multiprotein complexes that connect the actin cytoskeleton with the ECM through integrin receptors. They maintain

tissue integrity and resistance to mechanical stress. In turn, FAs are the main regulators of mechanotransduction which constitute signaling complexes that coordinate different pathways involved in cell function (adhesion, proliferation, migration, differentiation)²⁶.

Integrins are broadly expressed heterodimeric **adhesion molecules** that connect ECM components to the intracellular cytoskeleton. They are constituted by two subunits: **α and β** . This α/β is a non-covalent association that defines the **affinity state** and **specificity** for its ligands, depending on the conformation that they adopt and the type of α and β subunits. There are eighteen α subunits and eight β subunits that can combine in 24 different manners. In epidermis, integrins are constitutively expressed or wound induced. The most abundant integrins in basal keratinocytes are laminin receptors ($\alpha 6\beta 4$, $\alpha 3\beta 1$) and collagen-binding receptors ($\alpha 2\beta 1$) or the wound induced fibronectin, tenascin and vitronectin receptors ($\alpha 9\beta 1$)²⁷.

Each integrin subunit contains an extracellular domain, a transmembrane segment, and a short cytoplasmic tail. This ensures a two-way signaling:

- **Inside-out:** intracellular signals recruit molecules to the cell membrane, which bind to integrin cytoplasmic tail inducing a conformational change in the extracellular domain. This conformational change activates integrin by changing its affinity state for the ligand.
- **Outside-in** activated integrin binds to its ligand at ECM. This is essential for rigidity sensing since force transmitted from the substrate to the integrin triggers the assembly of a protein complex at the intracellular domain. This allows integrin binding to the actin cytoskeleton and thus, a direct force transmission between cells and their surroundings²⁸ (*Figure 2.4*).

More than 150 proteins involved in FA complexes have been described²⁹.

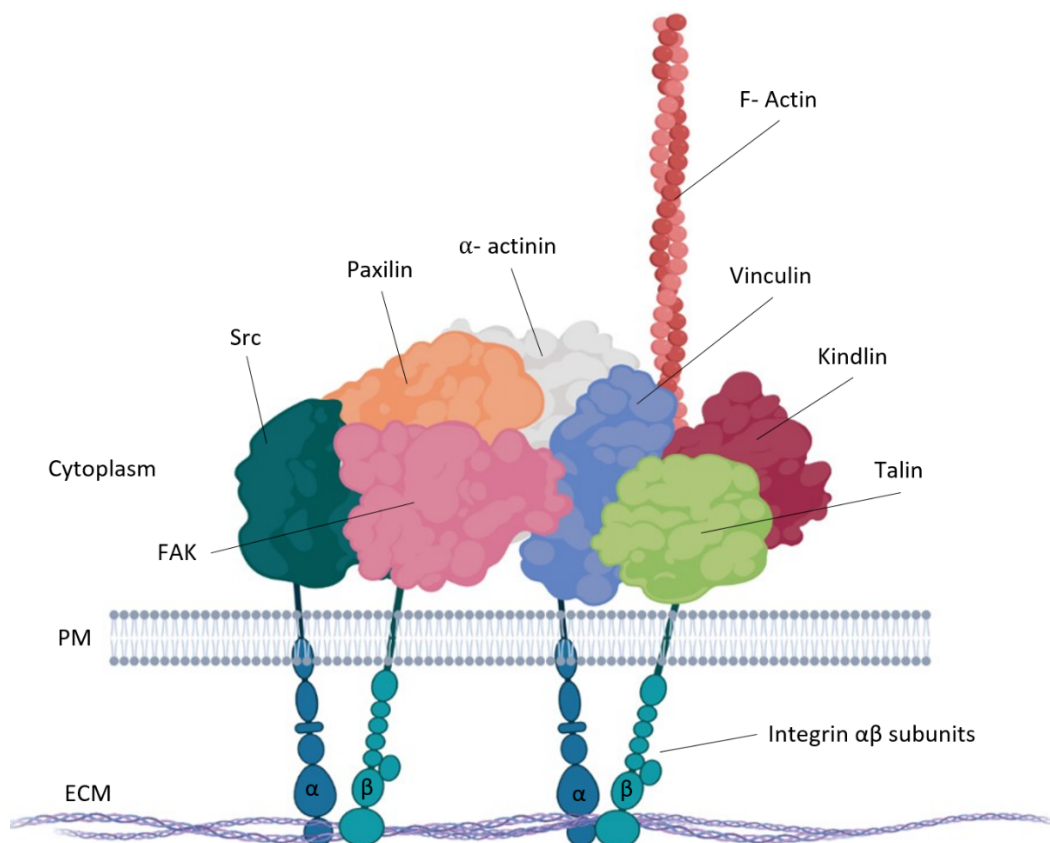


Figure 2.4. General representation of some of the molecules involved in the focal adhesion (FA) complex. ECM. Extracellular matrix. PM. Plasma membrane. $\alpha\beta$ Integrin heterodimers are bonded to the ECM (open active conformation, high affinity state). This is a self-created illustration, using www.Biorender.com.

- **Adherens Junctions**

Adherens junctions (AJs) are cell-cell adhesion complexes mediated mainly by cadherin molecules and dynamically response to external stimuli. As well as FAs, they are mechanosensitive and allow **mechanical coupling** between cells³⁰.

The Cadherin family is a group of glycoproteins involved in calcium-dependent cell-cell adhesions. Specifically, E-Cadherin mediates intercellular contacts in epithelial cells and drives cell polarity³¹. **Cadherins** are transmembrane molecules that present an extracellular domain which acquires an active conformation in the presence of calcium to establish cadherin-cadherin interactions between neighboring cells. The cytoplasmic domain of cadherin is connected to the actin cytoskeleton through a protein complex that is reinforced in response to mechanical forces. This creates a **multicellular**

actin network essential for a coordinated cell behavior. Thereby, mechanosensitive AJs play an important role in the transmission of intercellular tension, cell polarization and migration and tissue integrity^{32,33,34,35}.

2.4 Cell migration

Cell migration plays an essential role in many physiological and pathological processes in the body. In order to move, cells need to establish an interaction with their environment through several structures such as lamellipodia, filopodia and podosomes.

This cell movement can be carried out as **individual** cells, as white blood cells during the immune response or germ cells, or as a **collective** as occurs during development, wound healing or tumor invasion.

2.4.1 Single cell migration

To be able to move, cells need to experience a **polarization** and then develop extensions (**lamellipodia and filopodia**) which expands to establish the leading edge of the cell. These extensions adhere to the substrate while the body of the cell must retract³⁶. This polarization could appear spontaneously in absence of external signals, which is called “**random walker**” (effective only for very short distances), or otherwise, cells can migrate in response to **chemical or physical signals** which promotes a constant migration over long distances³⁷.

Thanks to advancing imaging techniques, the steps that a single cell migration involves have been widely described (*Figure 2.5*):

1. **Polarization**: the direction of the cell movement is determined in response to an external stimulus. It defines the cell front and back by orienting and reorganizing the molecular mechanisms of cell migration.
2. **Protrusion**: polymerization of actin filaments at the leading edge pushes the cell membrane forward over the substrate resulting in cell extension.

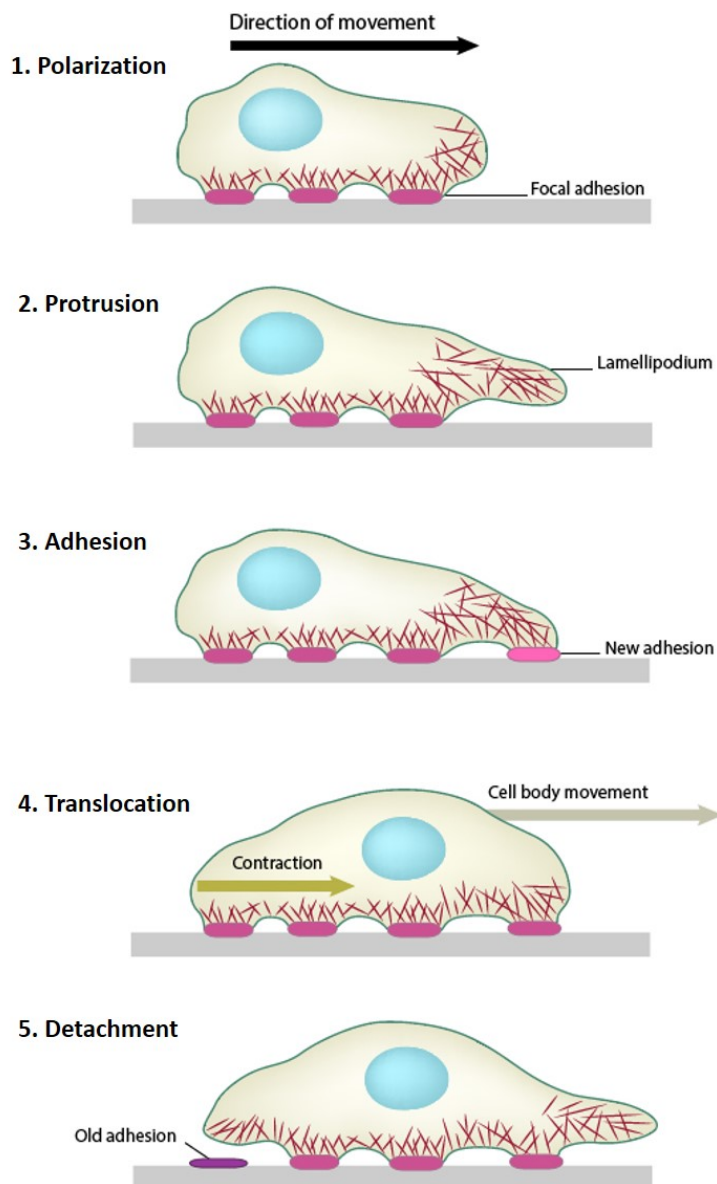


Figure 2.5. Schematic representation of cell movement stages. 1. Polarization. 2. Protrusion. 3. Adhesion. 4. Translocation. 5. Detachment. Modified from MBInfo³⁸.

- 3. Adhesion:** binding of the cell membrane receptors to the substratum through focal adhesions, which in turn links to the network of actin filaments.
- 4. Translocation:** Also called retraction. The body of the cell is pulled forward by the retrograde actin flow combined with contractile forces produced at the rear of the cell by the actomyosin network. Myosin II mediates this contraction by regulating the gliding of microfilaments and stress fibers and generates enough force to drag forward the trailing edge of the cell.

5. **Detachment:** As a result of the tensile forces created by the contraction of the actomyosin network, focal adhesions disassemble at the rear of the cell and the cell crawls forward. Some extracellular events, such as ECM proteases activity on the substrate, are thought to also contribute to FA release ^{16, 36,39,40,41}.

2.4.2 Collective cell migration

In nature, collective migration has been defined as “*the movement of groups in which individuals affect the behavior of one another*” ⁴². Thus, epithelial cells are connected to each other and move coordinately while keeping the integrity of the tissue. This way, they make robust collective decisions to guarantee a suitable cell distribution and tissue remodeling.

The mechanisms that underlie single cell migration have been widely studied⁴³, and in recent years the field has experienced a great evolution in the understanding of collective cell migration mechanisms⁴⁴. As seen above, single cells triggered by an external signal, undergo a several-step cyclic process driven by **actin polymerization and contractility** of the cell body, which is also fundamental in collective cell migration.

Some of the differential aspects of collective cell behavior are:

- Cells are coupled by **cell-cell junctions**. They coordinate these processes to move as a cohesive group and transmit the **pulling forces** through this physical coupling.
- They experience a **simultaneous polarization** of many cells at the leading edge, which are called “**leading cells**” (*Figure 2.6*).
- A **unified organization of the actin cytoskeleton** helps to generate traction forces within the cell sheet, which are higher than those generated by single cells as every cell contributes to the movement.
- **ECM** is remodeled as cells move forward, in order to adapt the available space for the cell group in constant movement and for the formation of a **basal membrane**^{45,46}.

Many years ago, **cell density**⁴⁷ was described as another important regulator of cell migration. Abercrombie and Heaysman observed in 1953 that chicken fibroblast cells alter their polarization, inhibiting protrusions at the site where they contact another cell, and developing new ones away from such contact, thus resulting in the change of the direction of migration. This is a mechanism, called **contact inhibition of locomotion** (CIL), by which cells are capable of sensing cell density. In this respect, it has been shown that mechanical forces are transmitted through intercellular adhesion proteins to generate CIL.

From this, it can also be observed that the higher the cell density, the higher the friction between cells and then the lower the velocity of migration, thus switching the system from a liquid-like state to a solid-like state⁴⁸.

The exposure of a cell monolayer to an empty space, triggers a migratory behavior, which translates into the formation of **finger-like** structures constituted by the so-called “**leader cells**” that show extended lamellipodia and are strongly attached to the follower cells by **cadherin** molecules. These leader cells have the ability of pulling the followers. This results in a polarized cluster where every single cell acquires the same direction as the leader cells (**directional guidance**).

In addition to cell polarization, a contractile **actin belt** acts as a complementary mechanism that helps the collective group to migrate. These actin bundles connect the cells that build up the finger-shaped structure along its edges. This mechanism is similar to the **purse-string** found in *in vivo*, which contributes to the late stage of the gap closure by its actomyosin mediated contraction.

Beyond the migrating front, different cellular movements arise **within the epithelial sheet**, some of which could be described as **laminar flows**. Furthermore, there are chaotic movements within the migrating cell monolayer, that can be visualized as “**vertices**”, as well as **cell division** or **extrusion** which also affects tissue dynamics.

In this context, among all the cellular adhesions, “adherens junctions” play an essential role in the coordination of cell movements and mechanosensitivity^{37,49,30}.

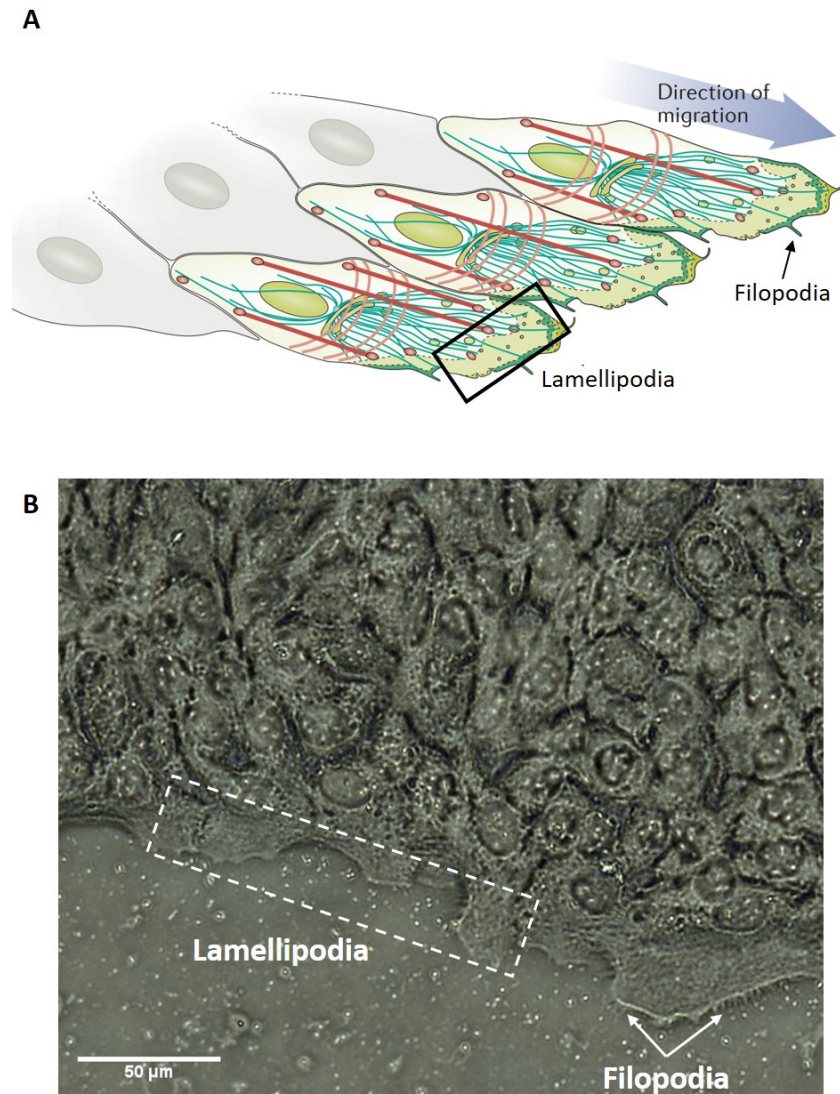


Figure 2.6. Polarization of leader cells in collective migration. A. Illustration modified from Mayor et al.⁵⁰ It represents the leading-edge plasma membrane with elongated leading cells that spread their lamellipodia in response to biochemical and mechanical cues, while pulling and guiding their coupled followers in a specific direction (directional guidance) **B. Contrast phase image of a migrating cell monolayer (HaCat cells).** **White dashed line and arrows** indicate, respectively, some of the lamellipodia and filopodia of the leader cells. **Scale bar = 50 μm.**

2.5 Mechanobiology

Mechanical forces may activate cellular mechanoreceptors that trigger signaling pathways converting them into biochemical responses (**mechanotransduction**) that influence cellular behavior (migration, proliferation,

differentiation, apoptosis, morphogenesis). Cells can also react to these physical stimuli by means of **cytoskeletal re-organization** and **force generation**⁵¹. For this reason, it is critical for development, homeostasis and progression of many diseases how cells respond to its biochemical and biomechanical environment.

We have mentioned above that cells that form a collective behave similar to a huge single cell in terms of migration mechanisms. It appears that the same occurs when we refer to forces exerted by cell monolayers on the ECM. Due to larger focal adhesions formed by the leading cells, it seems that **higher traction forces** are generated at the **front edge** and **propagate inwards** across the entire cell sheet⁵², while opposite retraction forces are generated at the back by the follower cells.

This whole coordinated mechanism needs to be maintained stable. It is transmitted through **cell-cell adhesions** and is reinforced by the so-called actin bundles formed at the edge of the migrating finger-like structure³⁰.

2.6 Forces involved in cell motion

A migrating cell, experiences external forces from the surrounding environment, and internal forces that arises from its own cytoskeleton. This cell movement process generates forces from actin polymerization, cell adhesions and from the cell body translocation.

- **Actomyosin cytoskeleton**

As mentioned above, cytoskeleton is a strong scaffold made of polymers with different stiffness and diameters (actin, microtubules and intermediate filaments) that, in combination with other proteins, form a strong network which provides the cell with **structural resistance, shape**, ability to **migrate and divide** and **transport of internal organelles**. Regarding cell motility, although other polymers also contribute to cell movement, the actin cytoskeleton has been described as the most important in the promotion of cell extension (second step of cell migration process)²³.

Actin filaments are organized in different manners. Thus, the **cell cortex** is a dense network beneath the plasma membrane that, in association with

myosin and other actin binding proteins (ABPs), confers the cell perimeter gel-like properties. In **filopodia** and **lamellipodia** they can adopt different arrangements as parallel or y-branched bundles respectively (*Figure 2.7*).

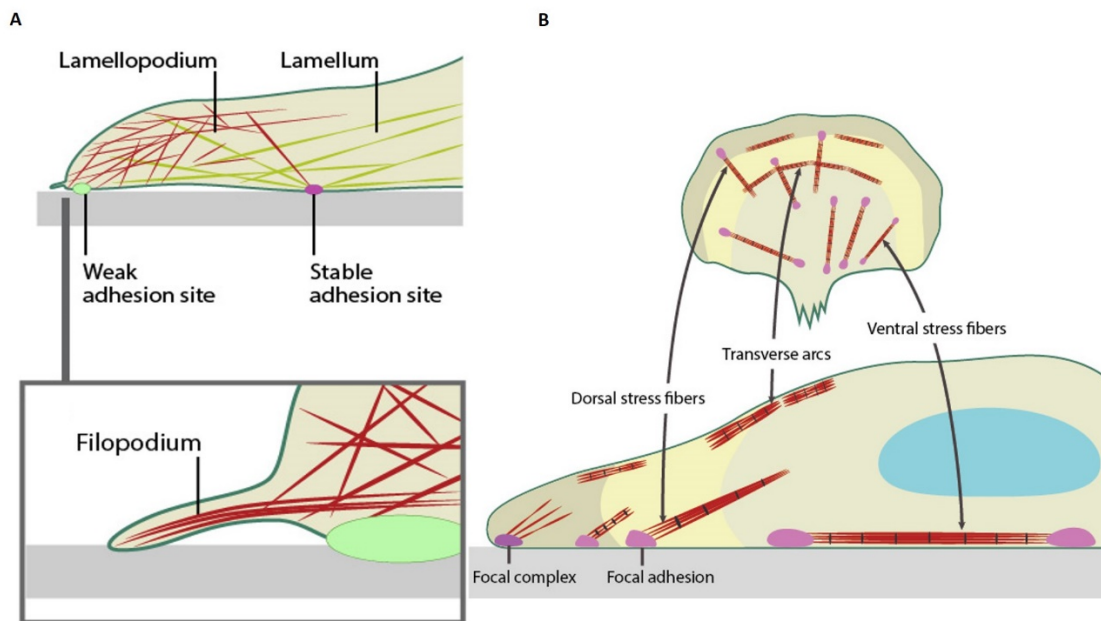


Figure 2.7. Cytoskeletal structures. A. Lamellipodia (y-branched actin bundles) and filopodia (parallel actin bundles) acting as sensory elements in cell migration. B. Stress fibers. Contractile actomyosin fibers that help maintain tension on the substratum. Dorsal and ventral stress fibers are anchored to focal adhesions while transverse arcs participate in driving cell protrusion. Modified from MBinfo³⁸.

Actin filaments are dynamic structures that undergo a process called “**treadmilling**” that allows the cell to rapidly adapt its response and elasticity. That means that actin filaments grow asymmetrically, adding or detaching monomers of globular actin to its different ends (plus and minus end) in a concentration and ATP dependent manner. This process generates forces that **push the cell membrane** forward thus forming cell protrusions. It is assisted by actin binding proteins (ABPs) which play different functions (α -actinin, cofilin, profilin, Arp2/3, WASP, formins, capping proteins).

Filamentous actin (F-actin) interacts with **myosin motor proteins** to generate contractile forces. Briefly, the head domain of the myosin protein, which has ATP hydrolyzing activity, is attached to the actin filament. Gliding of these heads along the actin filament in a cyclic manner produces contraction of

the actomyosin bundles. This is essential for **force generation** in lamellipodial structures and **stress fibers** ^{40,53}. (Figure 2.7).

- **Adhesion mechanics**

In order to migrate, these forces generated by the cytoskeleton, need to be transmitted to the substrate. This transmission is carried out through focal adhesions (FAs) from the cell to the ECM. In turn, stiffness from the ECM is sensed by the FA and transmitted to the cytoskeleton of the cell (**dynamic mechanoreciprocity**). It has been described that the protrusion-retraction cycles produced at the leading edge of migrating cells coincide with the force peaks produced by the local contractile rigidity sensing units (**Contractile units = CUs**). CUs establish a connection between nascent FAs via F-actin coupled to bipolar myosin filaments, which allow anti-parallel F-actin sliding in a sarcomere-like contraction. These leading-edge contractions probe substrate stiffness and drive adhesion reinforcement. If the substrate is rigid enough to support this contraction, recruitment of adaptor proteins is triggered to reinforce adhesion. Among them, α -actinin is responsible for F-actin binding and connects CUs to the retrograde actin flow, making possible the transmission of traction forces. Thus, FAs act as mechanosensitive **molecular clutches** that resist the actin retrograde flow and convert pulling forces into traction forces against the substrate^{54,55} (Figure 2.8).

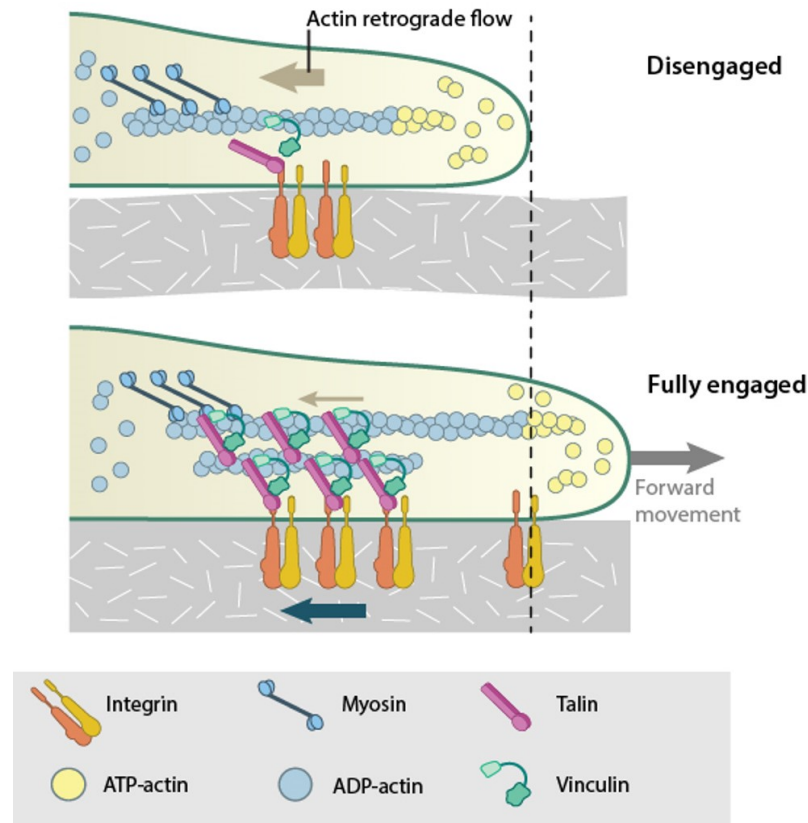


*Figure 2.8. Focal adhesions as molecular clutches. Retrograde flow of actin polymerization prevents the cell protrusions to be formed (**Disengaged**). When actin cytoskeleton is attached to focal adhesions (**Engaged**), it acts as a clutch that resist against the retrograde flow and translate the myosin contractions into traction forces on the underlying ECM, enabling the cell to move forward. **Modified from MBinfo**³⁸.*

On the other hand, cells are coupled between them and this allows the transmission of cytoskeleton generated forces to the follower cells promoting the collective cell motion. This **intercellular force transmission** is mainly mediated by the aforementioned **cadherin junctions**. It also contributes to cell polarization throughout the whole tissue during collective cell migration by generating high levels of Rac-1 at the front and high levels of RhoA at the back (**multicellular polarization**) (*Figure 2.9*)^{22,40,35,30}.

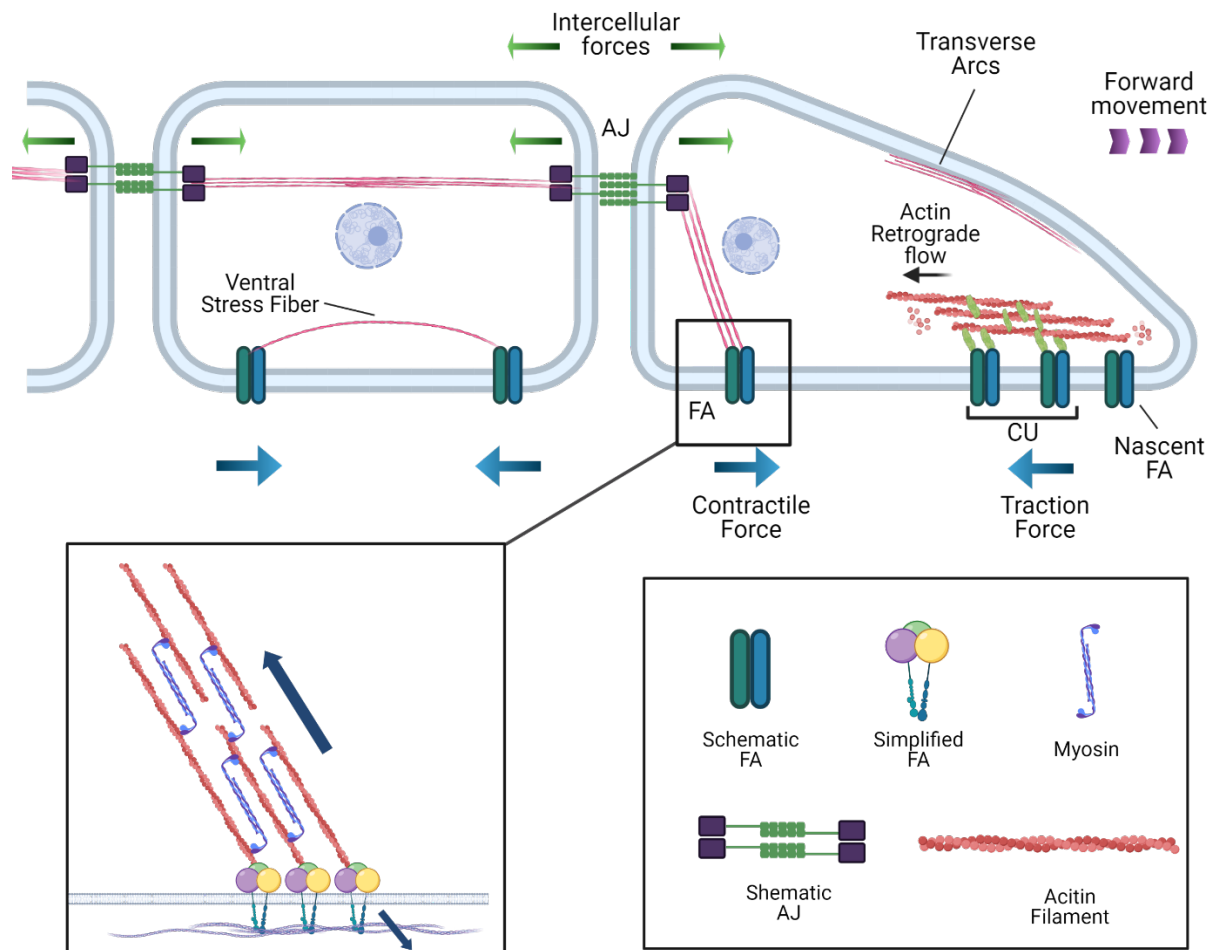


Figure 2.9. Transmission of cellular forces during cell migration. Actin treadmilling pushes the cell membrane and, helped by its anchorage to focal adhesions (FAs), part of the force generated by the retrograde flow is directed to the ECM resulting in the forward movement of the cell. Traction force is generated by the actin cytoskeleton connected to FA (inset). Intercellular forces are transmitted from leading cells to their neighbors through adherens junctions (AJs) that connect the cytoskeletons of neighboring cells. CU: Contractile units. This is a self-created illustration, using www.Biorender.com.

2.7 Measurement of cellular forces

Due to the evident importance of physical and mechanical characteristics of certain structures and organs in the body for supporting physical loads, studies in mechanobiology have been traditionally focused on the **macroscopic level**. Common examples of that are the skeleton or the skin as structural and protective elements against external stresses or the generation of forces in the respiratory and circulatory systems. But, in the last decades, new questions have arisen about the mechanisms of generation and bearing of forces at the

cellular level, resulting in the emergence of new experimental techniques for their detection⁵⁶.

As forces cannot be measured directly, it should be deduced from the **deformation caused on a material** of defined properties as they move⁵⁷. In this regard, many years ago, authors like James and Taylor (1969) made *in vitro* observations to describe tensions among migrating chicken fibroblasts from explants, particularly important for the contraction phase of wound healing⁵⁸. Some years later in 1980, Harris et al. stated that they could quantify traction forces that cells exert if they spread on a soft substrate by measuring its deformation⁵⁹. Those studies would be the first steps towards the development of **techniques** used nowadays to measure cellular forces⁶⁰. Several methods have been developed to determine the forces that cells produce or resist. Some of them are summarized in *Table 2.4*. These techniques must also be selected depending on the type of sample to be analyzed as well as its size, environmental requirements, biocompatibility and resolution needed (i.e. length and time scales)^{30,56}. (*Figure 2.10*).

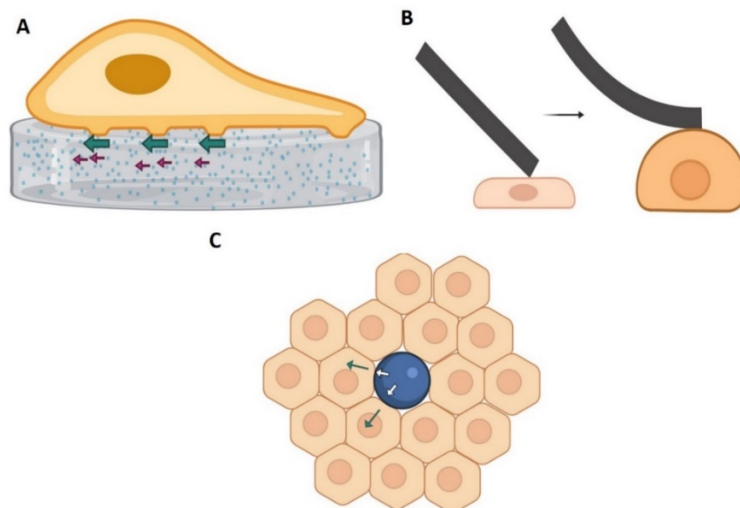


Figure 2.10. Schematic representation of some force sensing techniques. A. Traction force microscopy. Migrating cells exert traction force on the underlying soft substrate (green arrows). From displacement of fluorescent beads inside the substrate (purple arrows) its deformation can be measured. **B. Cantilever sensing.** The long structure is bent when a force is exerted on its free tip. Force exerted and displacement of the cantilever are proportional. **C. Droplets.** A deformable droplet of known mechanical properties is inserted in a tissue. This approach can be used to measure stresses inside 3D tissues^{61, 62}. **This is a self-created illustration, using www.Biorender.com.**

Force measurement tools

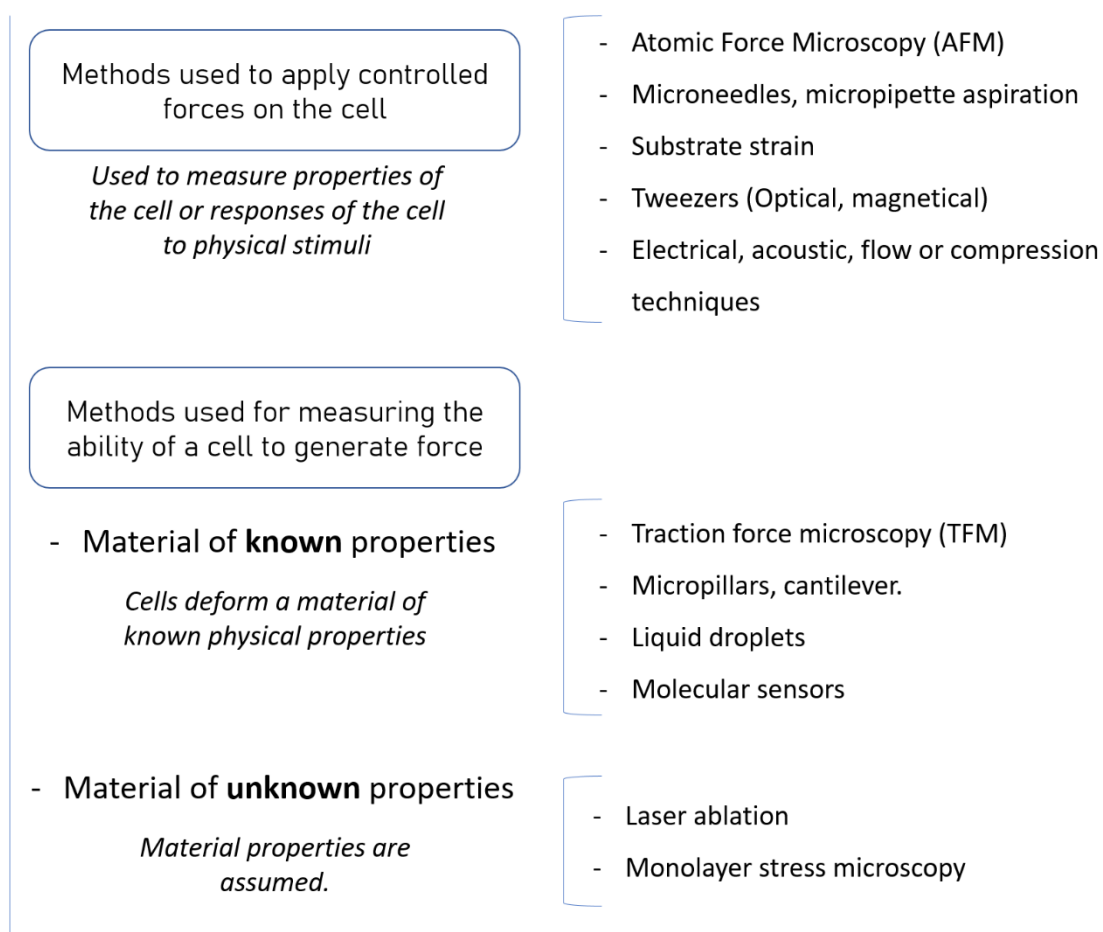


Table 2.4. Force measurement tools. Scheme of some of the techniques used to probe cellular forces^{30, 61,62,63}.

2.8 Wound healing

2.8.1 Wound healing process

Healthy skin needs to maintain its integrity to keep a physiological homeostasis of the human body as a protective barrier that averts infection, loss of water and thermal dysregulation⁶⁴. Injury to the skin causes disruption of the epidermis and the dermis or even deeper underlying tissues, depending on the depth of the wound. Wounds are awaited to heal within a period of 7 to 14 days, but when the process fails the wound will become a chronic non-healing wound⁶⁵.

Wound healing is a complex process that comprises four overlapping stages: hemostasis and coagulation, inflammation, proliferation and remodeling (Table 2.5)

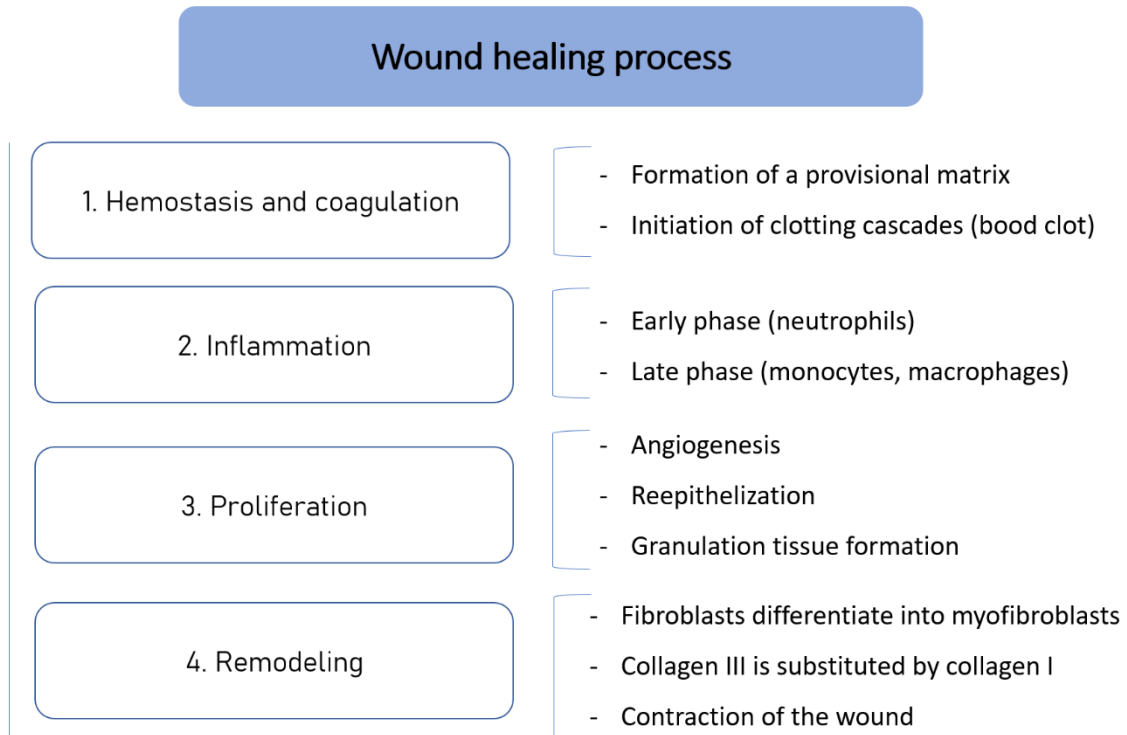


Table 2.5. Concept map of wound healing process.

- **Hemostasis and coagulation**

Begins right after injury and activates the **clotting cascade** as the first response to initiate hemostasis. The clotting factors initiate the extrinsic system and exposed collagen triggers the aggregation of thrombocytes resulting in the activation of the intrinsic clotting pathway. The aim of this activation is the formation of a **blood clot** which contains cytokines and growth factors⁶⁶ as well as fibrin, fibronectin, vitronectin and thrombospondins which constitute a **provisional matrix** that acts as a scaffold for the migration of different cells. Hemostasis and coagulation initiate the inflammation stage⁶⁷.

- **Inflammation**

This stage is essential to provide cytokines and growth factors for cellular migration and tissue movement. Most chronic wounds are thought to fail in the inflammatory step of wound healing⁶⁸.

In the **early phase** of the inflammatory process, neutrophils are recruited to kill bacteria, degrade necrotic tissue and recruit other cell types, thanks to their phagocytic function and secretion of pro-inflammatory cytokines, proteases, antimicrobial substances (such as ROS) and angiogenic factors. In the **late stage** of inflammation, monocytes are chemoattracted to the wound and differentiated into macrophages⁶⁹ (antigen-presenting cells) which phagocyte and secrete a wide variety of mediators⁷⁰.

Macrophages have an important role in the transition from inflammation to proliferation⁶⁴.

- **Proliferation**

The objective of this phase is to close the wound, including several steps: neovascularization/angiogenesis, reepithelialization and granulation tissue formation⁷¹.

- **Angiogenesis**

Angiogenesis begins with the activation of signaling pathways by binding of growth factors to their receptors on the endothelial cells. Then, the endothelial cells secrete metalloproteinases, which dissolve basal lamina and allow them to proliferate and migrate to form the new vessels.

- **Reepithelialization**

Local **fibroblasts migrate** through the fibrin mesh from the wound edges and start to synthesize **collagen I and fibronectin**, among other substances, that polymerize and cross-link to form a new metalloprotein-rich matrix of connective tissue. Synthesis of collagen and proliferation of fibroblasts are inversely proportional and promotes a balance to control degradation of the extracellular matrix (ECM). Keratinocytes play a key role in this stage as well,

because they 'shuffle' into the wound due to their ability to migrate in response of a chemotactic gradient. This process of migration ceases when migrating cells are in contact with each other⁶⁷.

- **Granulation tissue formation.**

Mainly fibroblasts, granulocytes, macrophages and blood vessels in complex with collagen form granulation tissue. Fibroblasts are responsible for the secretion of proteinases to **destroy the provisional matrix** previously generated during hemostasis. After that, fibroblasts synthesize collagen and other ECM components (e.g., proteoglycans, hyaluronic acid, glycosaminoglycans) to create granulation tissue⁷².

- **Remodeling**

The granulation tissue is replaced by the **scar tissue** with gradual increase in the concentration of **collagen fibers** that intend to reach a maximum **tensile strength**. It is not well known how immune mediators induce scar tissue formation.

Fibroblasts differentiate into **myofibroblasts**, which express α -smooth muscle actin (α -SMA) and help to contract the wound. The closure of the wound is characterized by the **degradation of collagen III** and its substitution by **collagen I**, which has a higher tensile strength. Likewise, **epithelial keratinocytes** that migrated into the wound area, concentrically **contract the wound**, thus increasing the tensile stress of the surrounding skin⁷¹. Matrix metalloproteinases (MMPs) and tissue inhibitors of metalloproteinases (TIMPs) are also secreted to **remodel** the newly synthesized ECM. The resulting scar exhibits mechanical properties different from those of unwounded skin⁷³.

2.9 Mechanical forces in wound healing and skin fragility disorders

The skin's characteristic structure and composition form a barrier against the external environment. Thanks to its high degree of intercellular attachment and the mechanical properties conferred by both the ECM and the intracellular

cytoskeleton, the skin is strong enough to maintain its **integrity** and yet sufficiently **flexible** to withstand mechanical stress. Changes in the amount or spatial organization and cross-linking of ECM components, lead to changes in cellular responses and vice versa. Thereby, tensional integrity of the skin (**tensegrity**) is maintained by a balance between intrinsic and extrinsic mechanical forces.

Several skin disorders are related to dysregulation of mechanical homeostasis. Epidermolysis bullosa, is a family of **skin fragility disorders**, characterized by skin blistering formation upon minor trauma or friction. This is due to mutations that lead to the absence or non-functional proteins involved in cell-cell or matrix cell anchorages. This renders the skin unable to withstand applied mechanical stresses and leads, depending on the affected anchoring structures, to blistering at different levels of the skin⁷⁴.

On the other hand, **wound healing** is also governed, in part, by mechanical cues. Forces arising from cell migration and myofibroblasts contractions are needed for gap closure, therefore, it is required that the ECM has certain biochemical and mechanical characteristics for the healing to be successful^{49,75}. In this respect, studies show different healing outcomes when comparing embryonic and adult wound closure⁶⁶. These differences are due to different mechanisms driving tissue repair, different ECM composition and thereby, different basal stresses in both cases.

An imbalance in tensional integrity between cells and ECM, leads to aberrant wound healing. **Hypertrophic scars and keloids** are both produced by a specific mechanical distribution at the wound site, that stimulates an excessive wound healing response. Some investigations for example, have focused on the study of the forces generated by fibroblasts obtained from keloids using AFM. They found out that actin filaments show different rigidity and force generation compared to normal fibroblasts, which drives to an increase in ECM secretion and enhanced migratory phenotype beyond the wound margins⁷⁶.

These findings have led to the development of a set of clinical therapies (**mechanotherapies**) based on the application of materials or devices to modify

tensions at the wound site. Some examples are the use of “paper tape” or “embrace advanced scar therapy” to relieve mechanical tensions and reduce scarring and fibrosis⁷⁷. Other mechanotherapies, such as **NPWT** (negative pressure wound therapy), are used to improve healing of **chronic wounds**. NPWT is based on the application of micromechanical forces to the wound environment that results in tissue strain and reduced inflammation⁷⁸. This could help to restore a “dead space” formed because of the persistent inflammatory environment and the destruction of ECM. The absence of a proper **ECM structure** prevents the cells to transmit mechanical forces (reduced migration, proliferation, differentiation, and contractile function of myofibroblasts). The application of forces through these therapies, induces macro and micro deformations in the wound bed which can improve the non-healing wound scenario⁷⁹.

Furthermore, in multifactorial diseases, such as **cancer**, mechanical properties play a key role. In solid tumors, there is a constant tug-of-war between the **mechanical compressive stress inside the tumor**, produced by the growth of cancer and stromal cells and an excessive ECM production, and the **stress applied externally** by the surrounding tissue that resists tumor expansion. Hence, tumors produce a stiffer matrix that pushes the surrounding tissue in order to grow. Thereby, increased tumor stiffness favors invasion and migration.⁸⁰

Gathering all this knowledge and important factors for skin functionality, 3D skin models are already being developed that focus on the maintenance of physiologic tensional homeostasis of skin, such as *in vitro* 3D organotypic cultures⁸¹, *ex vivo* research devices for pharmacological and cosmetic testing⁸², or RDEB (recessive dystrophic epidermolysis bullosa) 3D *in vitro* models to evaluate and quantify mechanical adhesion of dermo-epidermal junctions⁸³.

Characterization of mechanical forces in biological processes, improve the development of models mimicking physiological or pathological scenarios, that combine molecular and mechanistic features. This is essential for a more

accurate design of diagnostic tools and drug discovery, which in addition, are reliable alternatives to animal testing.

1. Velasco, D., Quílez, C., Garcia, M., del Cañizo, J. F. & Jorcano, J. L. 3D human skin bioprinting: a view from the bio side. *J. 3D Print. Med.* **2**, 141–162 (2018).
2. Paul A.J. Kolarsick, BS, Maria Ann Kolarsick, MSN, ARNP-C, and Carolyn Goodwin, APRN-BC, F. Anatomy and Physiology of the Skin. *J. Dermatol. Nurse. Assoc.* **3**, 203–203 (2011).
3. Anthony L. Meschner. *Junqueira's basic Histology. Text and atlas.* (McGrawhill, 2013).
4. McLafferty, E., Hendry, C. & Farley, A. The integumentary system: anatomy, physiology and function of skin. *Nurs. Stand.* **27**, 35–42 (2012).
5. Solano, F. Melanins : Skin Pigments and Much More — Types , Structural Models , Biological Functions , and Formation Routes. **2014**, (2014).
6. Matejuk, A. Skin Immunity. *Arch. Immunol. Ther. Exp. (Warsz).* **66**, 45–54 (2018).
7. Roudaut, Y. *et al.* Functional organization and molecular determinants of mechanosensitive receptors. **6**, 234–245 (2012).
8. William D. James, Dirk Elston, James R. Treat, Misha A. Rosenbach, I. N. *Andrews' Diseases of the Skin.* (Elsevier Inc., 2019).
9. Habif, T. P. *Clinical Dermatology. A color guide to diagnosis and therapy.* (Elsevier Inc., 2015).
10. Albanna, M. Z., Holmes IV, J. H., Allen-Hoffmann, B. L. & Rooney, P. J. *Skin Tissue Engineering and Regenerative Medicine. Skin Tissue Engineering and Regenerative Medicine* (2016). doi:10.1016/B978-0-12-801654-1.00013-9
11. Kalinin, A., Marekov, L. N. & Steinert, P. M. Assembly of the epidermal cornified cell envelope. *J. Cell Sci.* **114**, 3069–3070 (2001).
12. Bouwstra, J. A. & Ponc, M. The skin barrier in healthy and diseased state. *Biochim. Biophys. Acta - Biomembr.* **1758**, 2080–2095 (2006).
13. Proksch, E., Brandner, J. M. & Jensen, J. The skin: an indispensable barrier. 1063–1072 (2008). doi:10.1111/j.1600-0625.2008.00786.x
14. Komal Vig *, Atul Chaudhari, Shweta Tripathi, Saurabh Dixit, Rajnish Sahu, Shreekumar Pillai, V. A. D. and S. R. S. Advances in skin regeneration using tissue engineering. *Int. J. Mol. Sci.* **18**, 789 (2017).
15. Harvey, C. Wound Healing. *Orthop. Nurs.* **24**, 143–157 (2005).
16. Alberts, B. *et al. Essential Cell Biology.* (2014). doi:citeulike-article-id:4505949
17. Alberts, B. *et al. Molecular Biology of the Cell.* (Garland Science, 2015). doi:10.1024/0301-1526.32.1.54
18. Rosso, F., Giordano, A., Barbarisi, M. & Barbarisi, A. From Cell – ECM Interactions to Tissue Engineering. *J. Cell. Physiol* **199**, 174–180 (2003).

19. Ross, J. M. *Frontiers in Tissue Engineering*. (Elsevier Ltd., 1998). doi:10.1016/B978-0-08-042689-1.X5001-8
20. Chermnykh, E., Kalabusheva, E. & Vorotelyak, E. Extracellular Matrix as a Regulator of Epidermal Stem Cell Fate. *Int. J. Mol. Sci.* **19**, (2018).
21. Yurchenco, P. D. Basement Membranes: Cell Scaffoldings and Signaling Platforms. *Cold Spring Harb Perspect Biol* **3**, 1–27 (2011).
22. Pascalis, C. De, Etienne-manneville, S. & Weaver, V. M. Single and collective cell migration: the mechanics of adhesions. *Mol. Biol. Cell* **28**, 1833–1846 (2017).
23. Pollard, T. D., Earnshaw, W. C. & Johnson, G. T. *Cell biology*. (Elsevier Inc, 2017). doi:10.1016/C2014-0-00272-9
24. Xavier Trepap, Zaozao Chen, K. J. Cell Migration. *Compr Physiol* **2**, 2369–2392 (2012).
25. Anderson, K. I. & Cross, R. Contact dynamics during keratocyte motility. *Curr. Biol.* **10**, 253–260 (2000).
26. Roca-Cusachs, P. *et al.* Integrin-dependent force transmission to the extracellular matrix by α -actinin triggers adhesion maturation. *Proc. Natl. Acad. Sci. U. S. A.* **110**, (2013).
27. Longmate, W. M. & DiPersio, C. M. Integrin Regulation of Epidermal Functions in Wounds. *Adv. Wound Care* **3**, 229–246 (2014).
28. Qin, J., Vinogradova, O. & Plow, E. F. Integrin bidirectional signaling: A molecular view. *PLoS Biol.* **2**, 726–729 (2004).
29. Zaidel-Bar, R., Itzkovitz, S., Ma'ayan, A., Iyengar, R. & Geiger, B. Functional atlas of the integrin adhesome. *Nat. Cell Biol.* **9**, 858–867 (2007).
30. Ladoux, B. & Mège, R. M. Mechanobiology of collective cell behaviours. *Nat. Rev. Mol. Cell Biol.* **18**, 743–757 (2017).
31. Desai, R. A., Gao, L., Raghavan, S., Liu, W. F. & Chen, C. S. Cell polarity triggered by cell-cell adhesion via E-cadherin. *J. Cell Sci.* **122**, 905–911 (2009).
32. Mège, R. M. & Ishiyama, N. Integration of cadherin adhesion and cytoskeleton at adherens junctions. *Cold Spring Harb. Perspect. Biol.* **9**, 1–18 (2017).
33. Khalil, A. A. & de Rooij, J. Cadherin mechanotransduction in leader-follower cell specification during collective migration. *Exp. Cell Res.* **376**, 86–91 (2019).
34. Mayor, R. & Etienne-manneville, S. The front and rear of collective cell migration. *Nat. Publ. Gr.* (2016). doi:10.1038/nrm.2015.14
35. Chen, T., Saw, T. B., Mege, R. M. & Ladoux, B. Mechanical forces in cell monolayers. *J. Cell Sci.* **131**, (2018).

36. Cooper, G. M. & Robert E. Hausman. *La célula*. (Marbán, 2009).
37. Ram, S., Vedula, K., Ravasio, A., Lim, C. T. & Ladoux, B. Collective Cell Migration: A Mechanistic Perspective. *Physiology* 370–379 (2013). doi:10.1152/physiol.00033.2013
38. The National University of Singapore. Mechanobiology Institute. MBinfo. <https://www.mechanobio.info/>(2018).
39. Kirfel, G., Rigort, A., Borm, B. & Herzog, V. Cell migration: Mechanisms of rear detachment and the formation of migration tracks. *Eur. J. Cell Biol.* **83**, 717–724 (2004).
40. Ananthakrishnan, R. & Ehrlicher, A. The forces behind cell movement. *Int. J. Biol. Sci.* **3**, 303–317 (2007).
41. Bray, D. *Cell movements. From molecules to motility*. (Garland Publishing, 2001).
42. Shellard, A. & Mayor, R. Rules of collective migration: From the wildebeest to the neural crest. *Phil. Trans. R. Soc. B* **375**, 1–9 (2020).
43. Vicente-Manzanares, M., J. Webb, D. & Rick Horwitz, A. Cell migration at a glance. *J. Cell Sci.* **118**, 4917–4919 (2005).
44. Norden, C. & Lecaudey, V. Collective cell migration: general themes and new paradigms. *Curr. Opin. Genet. Dev.* **57**, 54–60 (2019).
45. Friedl, P. & Gilmour, D. Collective cell migration in morphogenesis, regeneration and cancer. *Nat. Rev. Mol. Cell Biol.* **10**, 445–457 (2009).
46. Rørth, P. Collective Cell Migration. *Annu. Rev. of Cell Dev. Biol.* **25**, 407–429 (2009).
47. Rosen, P. & Misfeldt, D. S. Cell density determines epithelial migration in culture. *Proc. Natl. Acad. Sci.* **77**, 4760–4763 (1980).
48. Deforet, M., Hakim, V., Yevick, H. G., Duclos, G. & Silberzan, P. Emergence of collective modes and tri-dimensional structures from epithelial confinement. *Nat. Commun.* 1–9 (2014). doi:10.1038/ncomms4747
49. Poujade, M. *et al.* Collective migration of an epithelial monolayer in response to a model wound. *Proc. Natl. Acad. Sci. U. S. A.* **104**, 15988–15993 (2007).
50. Martin, P. & Nunan, R. Cellular and molecular mechanisms of repair in acute and chronic wound healing. *Br. J. Dermatol.* **173**, 370–378 (2015).
51. Eyckmans, J., Boudou, T., Yu, X. & Chen, C. S. A Hitchhiker’s Guide to Mechanobiology. *Dev. Cell* **21**, 35–47 (2011).
52. Serra-picamal, X. *et al.* Mechanical waves during tissue expansion. *Nat. Phys.* **8**, (2012).
53. Blanchoin, L., Boujemaa-Paterski, R., Sykes, C. & Plastino, J. Actin dynamics, architecture, and mechanics in cell motility. *Physiol. Rev.* **94**,

- 235–263 (2014).
54. Meacci, G. *et al.* α -Actinin links extracellular matrix rigidity-sensing contractile units with periodic cell-edge retractions. *Mol. Biol. Cell* **27**, 3471–3479 (2016).
 55. Giannone, G., Mège, R.-M. & Thoumine, O. Multi-level molecular clutches in motile cell processes. *Trends Cell Biol.* **19**, 475–486 (2009).
 56. Moeendarbary, E. & Harris, A. R. Cell mechanics: Principles, practices, and prospects. *Wiley Interdiscip. Rev. Syst. Biol. Med.* **6**, 371–388 (2014).
 57. Trepap, X. When cellular forces became visible. *Nat. Rev. Mol. Cell Biol.* **21**, 253 (2020).
 58. James, D. W. & Taylor, J. F. The stress developed by sheets of chick fibroblasts in vitro. *Exp. Cell Res.* **54**, 107–110 (1969).
 59. ALBERT K. HARRIS, PATRICIA WILD & DAVID STOPAK. Silicone Rubber Substrata: A New Wrinkle in the Study of Cell Locomotion. *Science (80-.)*. **208**, 177–179 (1980).
 60. Munevar, S., Wang, Y. L. & Dembo, M. Traction force microscopy of migrating normal and H-ras transformed 3T3 fibroblasts. *Biophys. J.* **80**, 1744–1757 (2001).
 61. Rodriguez, M. L., McGarry, P. J. & Sniadecki, N. J. Review on cell mechanics: Experimental and modeling approaches. *Appl. Mech. Rev.* **65**, (2013).
 62. Roca-Cusachs, P., Conte, V. & Trepap, X. Quantifying forces in cell biology. *Nat. Cell Biol.* **19**, 742–751 (2017).
 63. Mohammed, D. *et al.* Innovative tools for mechanobiology: Unraveling outside-in and inside-out mechanotransduction. *Front. Bioeng. Biotechnol.* **7**, (2019).
 64. Sorg, H., Tilkorn, D. J., Hager, S., Hauser, J. & Mirastschijski, U. Skin Wound Healing: An Update on the Current Knowledge and Concepts. *Eur. Surg. Res.* **58**, 81–94 (2017).
 65. Lazarus, G. S. *et al.* Definitions and Guidelines for Assessment of Wounds and Evaluation of Healing. *arch dermatol* **130**, 489–493 (1994).
 66. Heng, M. C. Y. Wound healing in adult skin : aiming for perfect regeneration. *Int. J. Dermatol.* **50**, 1058–1066 (2011).
 67. Sorg, J. M. R. H. Wound Repair and Regeneration. *Eur Surg Res.* **49**, 35–43 (2012).
 68. Redd, M. J., Cooper, L., Wood, W., Stramer, B. & Martin, P. Wound healing and inflammation : embryos reveal the way to perfect repair. *Phil. Trans. R. Soc. Lond.* **359**, 777–784 (2004).
 69. Henry, G. & Garner, W. L. Inflammatory mediators in wound healing. *Surg*

- Clin North Am.* **83**, 483–507 (2003).
70. Eming, S. A., Krieg, T., Davidson, J. M. & Hall, R. P. Inflammation in Wound Repair: Molecular and Cellular Mechanisms. *J. Invest. Dermatol.* **127**, 514–525 (2007).
 71. Gonzalez, A. C. de O., Costa, T. F., Andrade, Z. de A. & Medrado, A. R. A. P. Wound healing - A literature review. *An. Bras. Dermatol.* **91**, 614–620 (2016).
 72. Landén, N. X., Li, D. & Ståhle, M. Transition from inflammation to proliferation: a critical step during wound healing. *Mol. Life Sci.* **73**, 3861–3885 (2016).
 73. Andrea Page-McCaw, A. J. E. & Z. W. Matrix metalloproteinases and the regulation of tissue remodelling. *Nat. Rev. Mol. Cell Biol.* **8**, 221–233 (2007).
 74. Hsu, C. *et al.* Mechanical forces in skin disorders. *J. Dermatol. Sci.* **90**, 232–240 (2018).
 75. Brugués, A. *et al.* Forces driving epithelial wound healing. *Nat. Phys.* **10**, 683–690 (2014).
 76. Harn, H. I. C. *et al.* Mechanical coupling of cytoskeletal elasticity and force generation is crucial for understanding the migrating nature of keloid fibroblasts. *Exp. Dermatol.* **24**, 579–584 (2015).
 77. Barnes, L. A. *et al.* Mechanical Forces in Cutaneous Wound Healing: Emerging Therapies to Minimize Scar Formation. **7**, 47–56 (2018).
 78. Shankaran, V., Brooks, M. & Mostow, E. Advanced therapies for chronic wounds: NPWT, engineered skin, growth factors, extracellular matrices. *Dermatol. Ther.* **26**, 215–221 (2013).
 79. Wiegand, C. & White, R. An introduction to the regulation of wound healing by micromechanical forces. *Wounds UK* **10**, (2014).
 80. Kalli, M. & Stylianopoulos, T. Defining the role of solid stress and matrix stiffness in cancer cell proliferation and metastasis. *Front. Oncol.* **8**, (2018).
 81. Kimura, S. *et al.* Tissue-scale tensional homeostasis in skin regulates structure and physiological function. *Commun. Biol.* **3**, 1–14 (2020).
 82. Hickerson, R. www.ten-bio.com.
 83. Jung, J. P., Lin, W. H., Riddle, M. J., Tolar, J. & Ogle, B. M. A 3D in vitro model of the dermoepidermal junction amenable to mechanical testing. *J. Biomed. Mater. Res. - Part A* **106**, 3231–3238 (2018).



3 Justification and objectives

*“If you don’t ask, you don’t get”
(Stevie Wonder)*

“Detection and characterization of mechanical forces and dynamic molecular rearrangements in collective cell migration” – Verónica López

3.1 Justification

Understanding of the mechanics of the spatiotemporal generation of 3D traction forces driving tissue morphogenesis and repair will provide more comprehensive information that could guide in the development of new approaches in the diagnostic and treatment of diseases (in this case, as a proof of concept, known skin diseases).

For this purpose, we will combine the use of our novel 2D force microscopy technique with genetic mutations, to connect specific molecular (i.e., adhesion dynamics and actin turnover) and structural (i.e. skin fragility) situations to the generation of 2D forces exerted during *in vitro* wound healing experiments. We will compare forces and cell migration patterns of healthy skin cells with that of others with known genetic deficiencies.

Once this technique is fully implemented and characterized for 2D cell monolayers, we aim to translate it to a 3D environment with the ultimate goal of being able to carry out *in vivo* three-dimensional force measurements.

3.2 Objectives

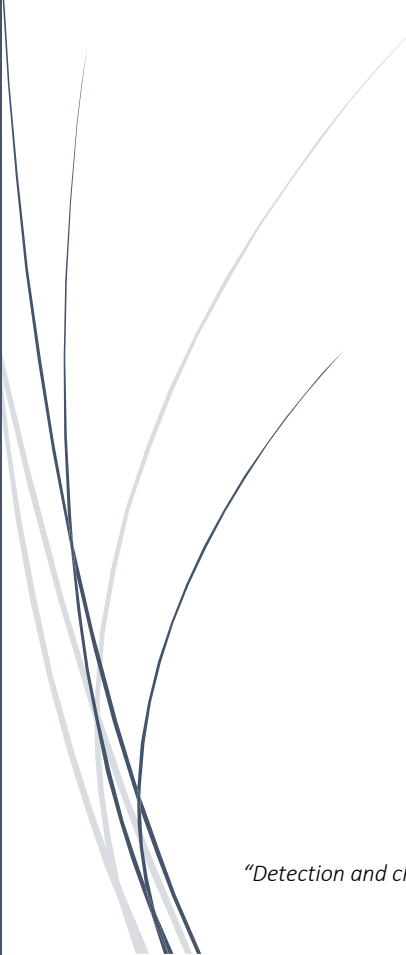

3.2.1 General aim

Development of an **experimental technique** and a **minimal** and simplistic **computational model** that describes the interaction between a biological tissue and an elastic body and characterize molecular dynamic rearrangements of cells subjected to our technique.

3.2.2 Specific aims

1. Setup of an experimental tool to measure cellular forces exerted on a compliant body during cell migration.
 - Selection of the force sensor, measuring system and materials to be employed in the experiments: compatible glue and flexible fiber rod of known properties.

- Design and 3D printing of the stencil to create controlled wounds on different plates.
2. Physical model formulation from the data generated by the experiments, to describe how a multicellular tissue modulates the forces it exerts depending on the stiffness of its external surroundings.
 3. Description of the cytoskeletal rearrangements and cell adhesion dynamics in a migrating cell monolayer while pushing a fiber rod.
 4. Elucidation of the impact of well-known genetic deficiencies on the biomechanics of tissue repair, by analyzing the differences between exerted forces of healthy and mutant human skin keratinocytes.
 - Generation and characterization of a kinlin-1 deficient cellular model and force measurement experiments.
 - Explore the sensitivity of the sensor to detect changes in cells exhibiting different phenotypes.



4 Measurement of forces exerted by migrating HaCat cells and formulation of the model

*Trying to grow up is hurting.
You make mistakes.
You try to learn from them,
and when you don't, it hurts even more.
(Aretha Franklin)*

"Detection and characterization of mechanical forces and dynamic molecular rearrangements in collective cell migration" – Verónica López

4.1 State of the art

Mechanobiology studies how mechanical forces influence cell behavior and cell shape. Traditionally, molecular pathways that control the main cellular functions have been widely studied, but less knowledge has been generated about how cells communicate with each other to coordinate their behavior in response to mechanical stimuli, or how they exert forces to migrate and divide. This was in part because of the lack of suitable technologies to measure and characterize them. Current biomechanical studies focus on the **combination of experimental and computational models**, to better describe the dynamics of living tissues and provide new insights to elucidate the role of mechanics in physiological and pathological situations¹.

Many biological processes are mediated by a **bidirectional** communication between cells and their external environment, in terms of mechanical forces. For instance, forces exerted by cells are responsible for tissue shaping during **embryogenesis** by influencing differentiation, migration and proliferation processes. In **wound healing**, they also play an important role, since confronted epithelial tongues (in cornea and skin) migrate until they meet and exert pressure on the opposite migrating front, resulting in a halting of the movement (CIL). Or for example in pathological situations such as cancer, it has been studied that the effect of compression stresses on a tumor worsens its response to pharmacological treatments²⁻⁵.

Force cytometry methods like the ones developed by Dembo et al.⁶, du Roure et al.⁷, Butler et al.⁸, Del Alamo et al.⁹, Trepap et al.¹⁰ and Tambe et al.¹¹ are today standard tools widely used to quantify traction forces in single cells or in cell monolayers. Many of them are based on the deformation of an elastic body or material of known physical properties.

The ability to accurately measuring the stresses (2D and 3D) exerted by individual cells, or by cell monolayers, resting on flat substrates using the methods described by these authors has provided significant knowledge towards a better understanding of mechanotransduction. Nonetheless, a vast majority of organs and tissues of interest are three-dimensional structures,

thus there exists a need to develop techniques capable of measuring cell-cell forces in a three-dimensional living tissue environment.

Several studies involving individual isolated cells embedded in 3D collagen fibrous matrices have been published in the last decades. This approach could provide a qualitative characterization of single cell migration in 3D biological matrices (Legant et al.¹², Koch et al.¹³), but it is not applicable to the complex multi-cell 3D tissue environment. For instance, Campàs et al.¹⁴ formulated a methodology capable of measuring inter-cellular force by introducing a drop inside a 3D tissue. However, cells can only exert normal stresses on the drop, a situation that is not physiological since cells can also apply shear forces on each other. In other words, it is unclear that the behavior of cells adhered to the drop is not altered. Other authors, have used beads instead of the drop, as tools for measuring and exert forces on tissues to quantify their mechanical properties⁴. Nonetheless, these methods require the injection of the element into the sample and depend on the accessibility to the tissue and the depth of the sample penetration by light¹⁵. Other approaches, like the use of optical tweezers¹⁶ or the development of 3D traction force microscopy as mentioned above^{12,17}, still present some difficulties to measure forces in three dimensional tissues or *in vivo* scenarios, such as sample heating (in the first example) or optical resolution¹⁸.

Together with experimental techniques, different **theoretical procedures** have arisen to better understand and interpret the measurements. In this respect, there are two major approaches. One of them is “**particle-based models**” that can describe cell-cell interactions and the cellular organization of the tissue, such as: Active network models (Vertex and Voronoi models), Vicsek-like models, Cellular Potts and phase-field models. The other approach is “**continuum models**”, which does not focus on individual particles, but refers to the whole collective of cells considering it a viscoelastic fluid (active gel theory). In continuous models, properties of individual cells and the tissue (i.e. velocity, cell density, cell polarity) are averaged over the entire collective^{19,20}

4.2 Motivation

To better understand all these processes, biology uses the mentioned **physical models** to describe the behavior of a specific system. In order to develop a model, it is necessary to identify the variables involved in the problem to establish relationships between them. This helps us to reproduce and understand in a theoretical way the process to be studied and to obtain information from our experiments. In turn, these models are supported by experimental measurements for its validation and fitting. These physical models usually describe the tissue as a fluid or solid-like active matter, characterized by variables that are expressed as differential equations and are often quite complex²⁰.

We try to overcome some of the limitations of the existing techniques, reducing the complexity of the system to be analyzed while keeping the physiological situation of the tissue, in order to avoid alterations in the behavior of tested cells. In our experiments, a **carbon fiber** is pushed by an epithelial cell monolayer that migrates in response to a free-edge exposure. Based on the experimental results obtained, we develop an **active-fluid (continuum) model** that qualitatively reproduces and predicts the most important characteristics of our system.

In this respect, one of our goals is to **reduce the complexity** of the model by recognizing which are the essential elements needed to describe our system. We remark that there are no models that describe how a multicellular tissue modulates the forces it exerts depending on the compliance of its external surroundings. This way we reduced the number of parameters to make them **easier** to understand and **complement** other existing models^{21,22}.

On the other hand, our 2D experimental setup is interesting in itself. It could help us to **compare mechanical behaviors of different cell types** (fibroblasts or endothelial cells for instance), cells presenting mutations that are representative of a specific **disease** (*See chapter 6*) or cells under different pharmacological **treatments**. We also expect this **affordable** and **reproducible** technique to be useful and adaptable to **three dimensional** experiments.

Moreover, it is a useful tool to better interpret the so-called **competition assays**²³, where two cell populations of different genotype and/or phenotype face each other and migrate until they collide. Thus, biochemical signals can be isolated from the mechanical role.

In summary, it can be used to identify and quantify the biomechanical mechanisms involved in healthy tissues as well as in pathological conditions such as chronic wounds or skin fragility disorders (widely studied in our group).

4.3 Methodology

To answer these questions, we used the classical 2D wound healing assay, which has the advantage of being reproducible and representative of physiological situations (i.e. wound healing). Later on, it could be modified to be used in three-dimensional cultures (*see chapter 7 Future perspectives*).

Our experimental method is based on a slender and long structure of known mechanical properties: a carbon fiber. This acts as a **cantilever** that is deformed by epidermal keratinocytes as they migrate. The resultant deflection of the structure is detected to infer the forces exerted by the cells (*Figure 4.1*).

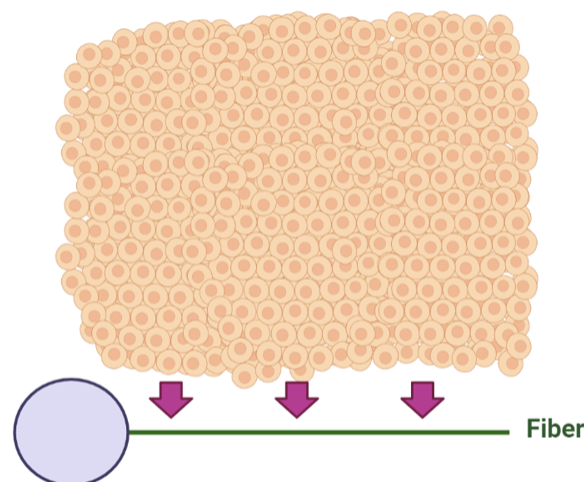


Figure 4.1. Schematic representation of the method. Cell monolayer migrating towards the carbon fiber. Green line: Carbon fiber. Pink arrows: direction of migration. Blue circle: Glue drop. This is a self-created illustration, using www.Biorender.com.

Keratinocytes are cells which conform a uniform monolayer while hardly attached to each other by cell junctions that mechanically stabilize the tissue and play a critical role in the transmission of forces during tissue

morphogenesis while they endure a constant mechanical stress²⁴. When exposed to a free- space, keratinocytes start to migrate. For this purpose, we decided to reproduce a traditional **2D wound healing assay**, by creating this free edge using a **stencil**. Stencils have been previously used by our group²⁵ and many other researchers^{26,27} to create “non-injured” wounds and thus avoid debris and permeabilization of the border cells due to the scratching of the monolayer, traditionally used for wound healing assays. These stencils are often made of PDMS (synthetic polymer).

In this work, we **3D printed** an **original stencil** made of PLA (Polylactic Acid), specifically designed for our experimental configuration. PLA is described as a bioplastic made of lactic acid, which makes it biocompatible²⁸ and amenable to be used together with cells. After removing the stencil, cells start to migrate until they reach the carbon fiber and start to push it as they advance. This carbon fiber has been previously glued at one of its ends to a cell culture plate. In order to create a homogeneous monolayer front as close to the fiber as possible while avoiding the bulging glue drop, we custom made the shape of the stencil (*See 4.4.2.Experimental setup, Figure 4.2*).

In addition, characterizing the speed and forces of a cell collective, leads to the use of techniques such as **PIV (Particle image velocimetry)**. A whole-field method to create **velocity maps** from time-lapse images, which determines the displacement of particles inside a fluid (cells in a tissue)²⁹.

4.4 Materials and methods

4.4.1 Cell culture

Experimental work with cells is carried out under aseptic conditions, in a level II biosafety laminar flow cabinet. Every cell culture is kept at 37 ° C in a moisture-saturated atmosphere containing 95% air and 5% CO₂ (*NAPCO CO2 incubator, Thermo Fisher Scientific (Waltham, MA, USA)*). Cell culture media are replaced every two days, depending on the cellular metabolic activity. Cell culture media consist of DMEM (*Dulbecco's Modified Eagles Medium 1X, Invitrogen Life Technologies*) supplemented with 10% Fetal Bovine Serum (*FBS, Thermo Scientific HyClone*) and 1% of Antibiotic Antimycotic (*ThermoFisher*).

To proceed to cell subculture, the adhered cell monolayer is washed with sterile 1x phosphate buffer saline (PBS), and cells are detached from the growth surface by trypsinization, using trypsin-EDTA enzyme solution 0.02% (Trypsin 1-300 0.25% - EDTA (Ethylenediamine tetraacetic acid) (*Sigma-Aldrich, Saint Louis, MO, USA*)) at 37 ° C for 20 minutes.

For preservation, cells are frozen and stored in liquid nitrogen. For this, cultures in exponential growth phase are trypsinized and resuspended in fetal bovine serum (*FBS, HyClone, Thermo Fisher Scientific*) supplemented with 10% dimethyl sulfoxide (*DMSO, Merck, Darmstadt, Germany*) as a cryopreservative agent.

4.4.2 Experimental setup

HaCat cells (human spontaneously immortalized epithelial keratinocytes) obtained from cell bank at CIEMAT, were used in these experiments. Cells were cultured as described above until 90% of confluence following standard protocols³⁰.

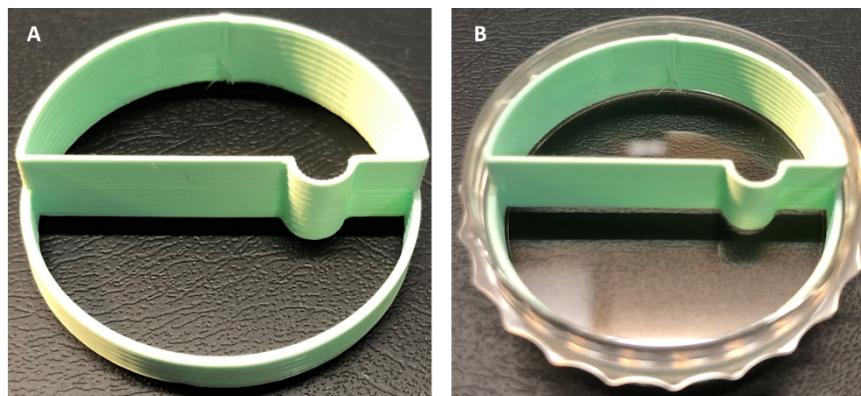


Figure 4.2. Designed of the 3D printed stencil for regular time lapse experiments. A. Top view. B. Top view inside of a petri dish.

First, an individual carbon fiber (7,8 μm diameter, kindly provided by Gustavo Victor Guinea, PhD from *Centre for Biomedical Technology*.) is separated from a bundle of fibers in a 35 mm petri-dish (*Corning®, Corning, NY*). Then, the individual carbon fiber is carefully positioned under a microscope with the help of a **custom-made 3D printed stencil** as a guide for its positioning (*Figure 4.2*).

Then, the fiber is glued at one end with a drop of cyanoacrylate glue, whose biocompatibility has been previously observed (*See carbon fiber positioning in Figure 4.3*). The glue drop needs to be as small as possible to reduce its interaction with the cell culture. Once the glue drop is completely dried, the fiber is cut to the corresponding length (2 to 5 mm) using a scalpel.

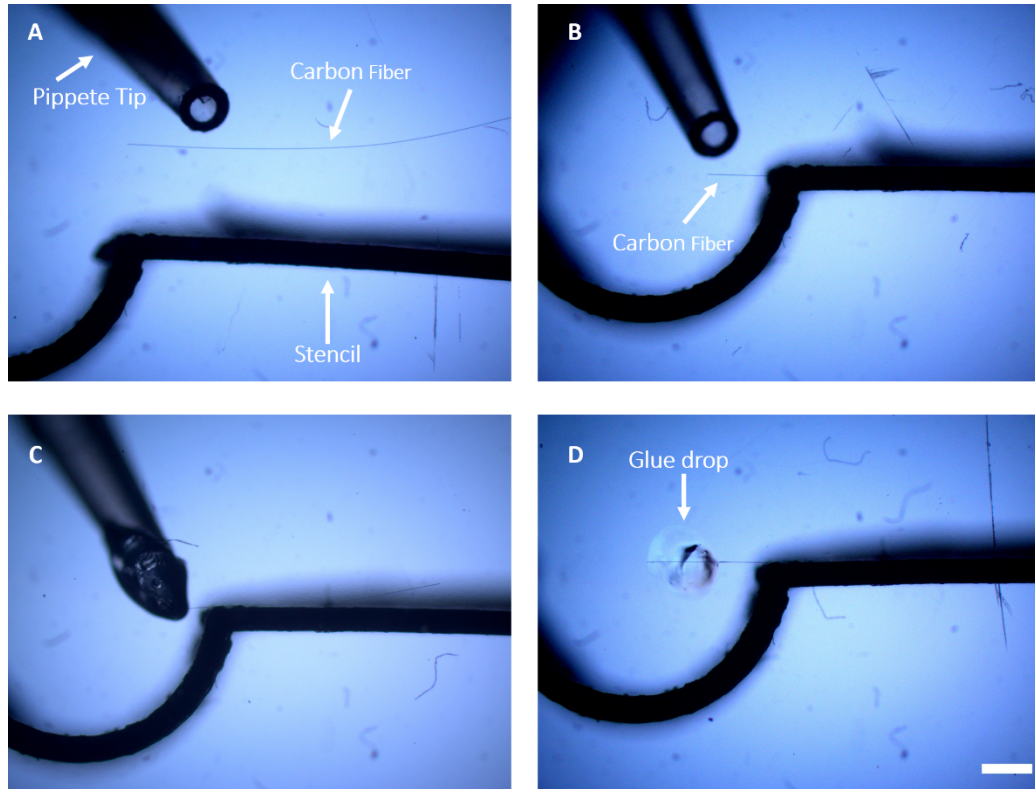


Figure 4.3. Steps for carbon fiber positioning under microscope. **A.** With a pipette tip we approach the fiber, previously placed on the plate, towards the stencil. **B.** Carbon fiber is placed in its final position. **C.** The fiber is glued at one end with a glue drop using a pipette tip. **D.** Carbon fiber is already glued in its final position before the removal of the stencil to let it dry. **Scale bar = 1000 μ m**

Following, 2 ml of collagen type I from bovine skin 0.1% (*Sigma Aldrich*) are used to functionalize the surface of the culture plate and the glued filament, for 2 hours at room temperature under the ultraviolet light. The stencil is also functionalized in a separate plate. After that period, the remaining collagen is removed, washed with PBS and left under UV light until it is completely dry.

Then, the stencil is placed again in the functionalized plate, cells are seeded at a final concentration of 1550 cells/mm² and incubated for 24 h to allow them to attach to the substrate, forming a confluent monolayer. Hereafter, the

stencil is carefully removed, creating the two-dimensional wound and excess cells are detached with a pippete tip (Figure 4.4).

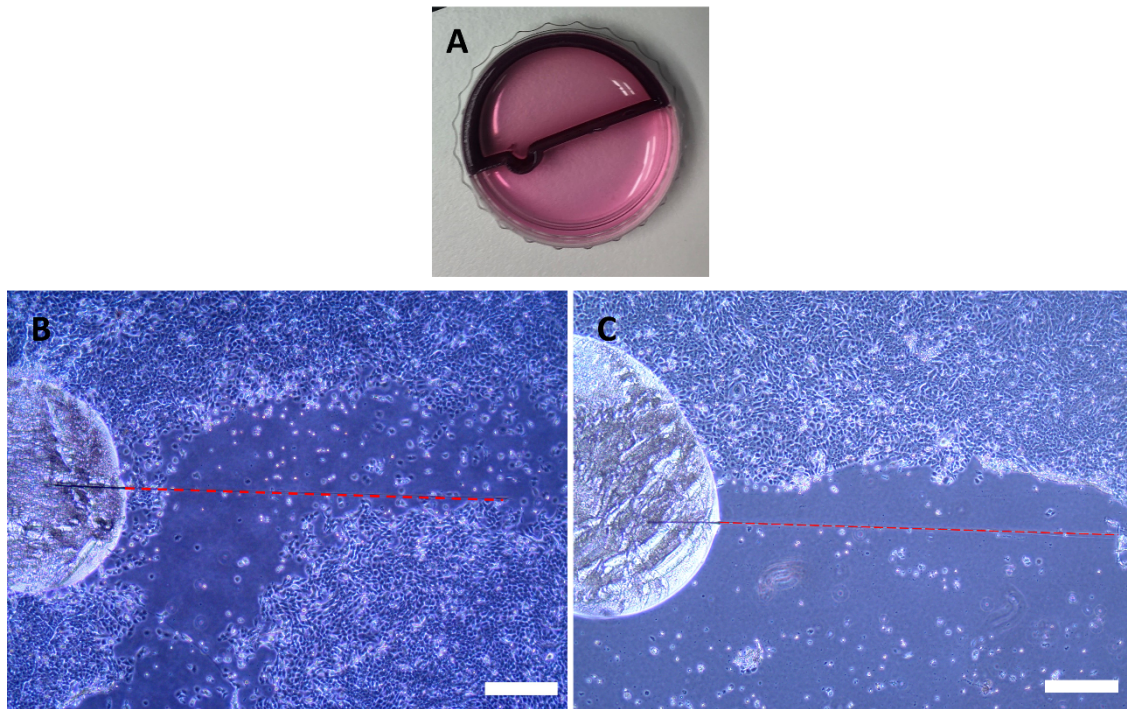


Figure 4.4. Stencil positioning. *A. Macroscopic top view of stencil position after seeding cells. B. Microscopic view after removing the stencil. C. Microscopic view after removing excess cells with a pippete tip. Red dashed line: Facilitates the visualization of the carbon fiber in the cell culture. Scale bar = 300 μm .*

The culture is afterwards washed with phosphate-buffered saline (PBS), and then 4 mL of fresh culture medium is added. This stencil-based method is more reproducible and causes less harm to the monolayer front than the classical scratching method.

4.4.3 Time-lapse experiments

Experiments are performed under an automated inverted microscope Leica Dmi8 (*Leica, Wetzlar, Germany*) equipped with an OKOLab incubator (*Pozzuoli, Italy*). A 4 petri-dish adaptor allows to control the temperature, air and CO₂, and humidity during the experiment.

The time-step between frames is 15 minutes and the total duration of each experiment is 120 hours.

Images are acquired in phase contrast with a 5X magnification objective and a Hamamatsu sCMOS Orca Flash 4.0 LT camera (*Hamamatsu City, Japan*) by means of LASX Navigator acquisition software from Leica Microsystems.

4.4.4 Image Analysis and velocity measurements

Custom-made **image analysis** codes for fiber detection were developed both in MATLAB software (*The MathWorks, Natick, MA*), using segmentation algorithms previously described³¹. The spatial resolution of the detection is 1,29 μm .

Velocity fields were measured from the time-lapse images using the open source toolbox PIVLab (*Time-Resolved Digital Image Velocimetry Tool for MATLAB*). The size of the interrogation window was set to 128 pixels with an overlap of 64 pixels and a second pass of 32 pixels, leading to a 32-pixel step between vectors. This corresponds to a spatial resolution of 42 μm between velocity vectors. The correlation algorithm chosen for the calculations was fast Fourier transform with multiple passes and allowing window deformation. The toolbox includes data validation section to filter noisy vectors by interpolating them between neighboring ones.

Kymographs are space-time plots that display the intensity values of a third variable. In our case this third variable is the streamwise velocity, u , that is the velocity along the x direction in *Figure 4.5* thus reducing, by projection, three-dimensional data (x, t, u) to two dimensions³².

For each region (shown as yellow dashed squares, A, B and C, in *Figure 4.8*), three columns of PIV velocity boxes of streamwise velocity (u) are averaged over the spanwise (y) direction in a band with a width of 126 μm . Each one of these averages is represented as a function of time. The color code corresponds to the value of “ u ”.

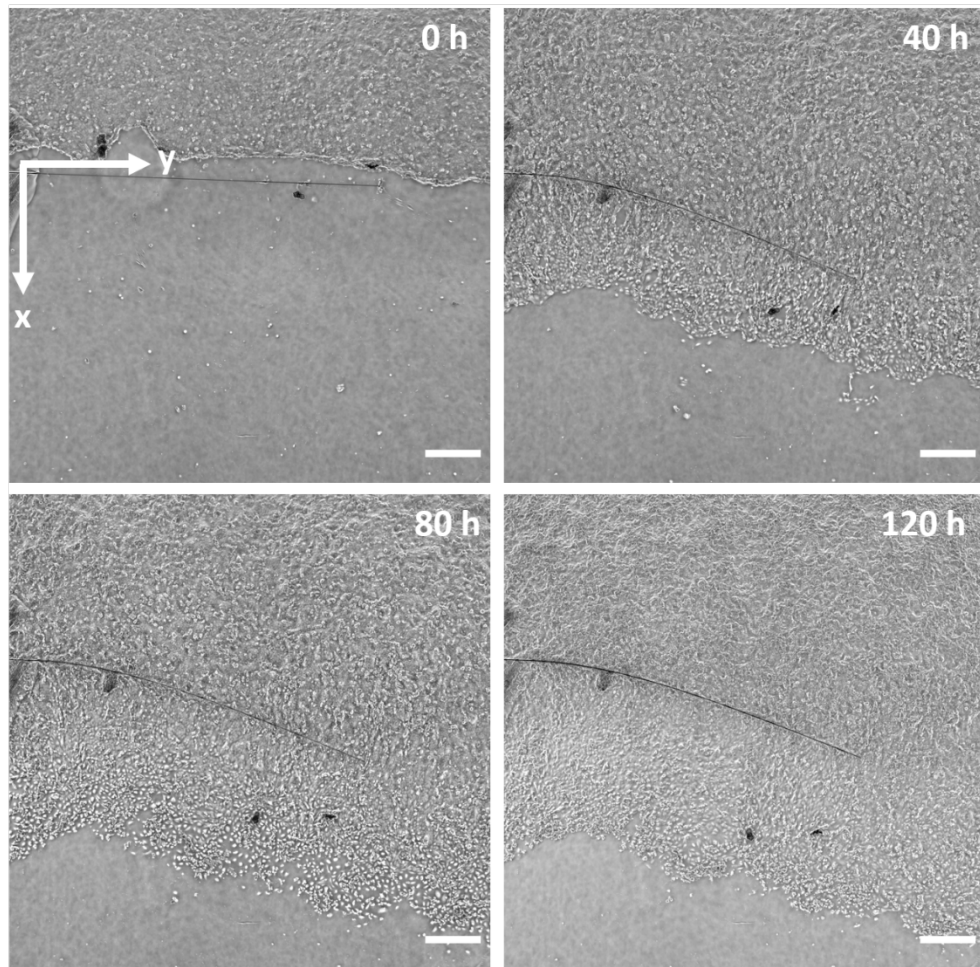


Figure 4.5. Evolution of the wound healing assay at different times. Carbon fiber length (L) = 3mm. X axis (streamwise): direction of collective cell migration. Y axis (spanwise): parallel to the undeformed fiber at the beginning of the experiment.

4.5 Results

4.5.1 Measurements of forces exerted by migrating HaCat cells

To summarize, the experimental setup used for the measurement of forces exerted by migrating cells, is carried out by gluing a carbon fiber at one end (hereafter “fixed end”) to a Petri dish and after its functionalization, a wound is created by using a stencil to prevent the attachment of cells to the fiber and its surroundings (*See 4.4.2. Experimental setup*).

As cells move forward to close the wound, they push the fiber causing its deflection. Then, from images, we analyzed the shape of the fiber over time in order to compute the force that cells are exerting on it. This force is modeled as a uniform force per unit length, f_0 , and the only parameter that we vary between

experiments is the length of the fiber, L , which is directly related to its rigidity. Lengths used for these experiments range from $L= 2\text{mm}$ to $L=5\text{mm}$.

To compute this force, we fit *Equation 4.1* described in Timoshenko ³³ to the different shapes adopted by the fiber (*Figure 4.6*).

$$x = \frac{f_0}{24EI} y^2 (y^2 - 4Ly + 6L^2)$$

Equation 4.1. Describes the shape of a flexible fiber of length L , fixed at one end ($y=0$) and free at the other ($y=L$) and deflecting under a constant force.

$x =$ Streamwise coordinate

$y =$ Spanwise coordinate

$E = 229 \times 10^6 \text{ nN}/\mu\text{m}^2$
(Young's modulus)

$f_0 =$ Measured force.

$$I = \left(\frac{\pi}{4}\right) \left(\frac{d}{2}\right)^2 = 181.7 \mu\text{m}^4 \text{ (Moment of inertia)}$$

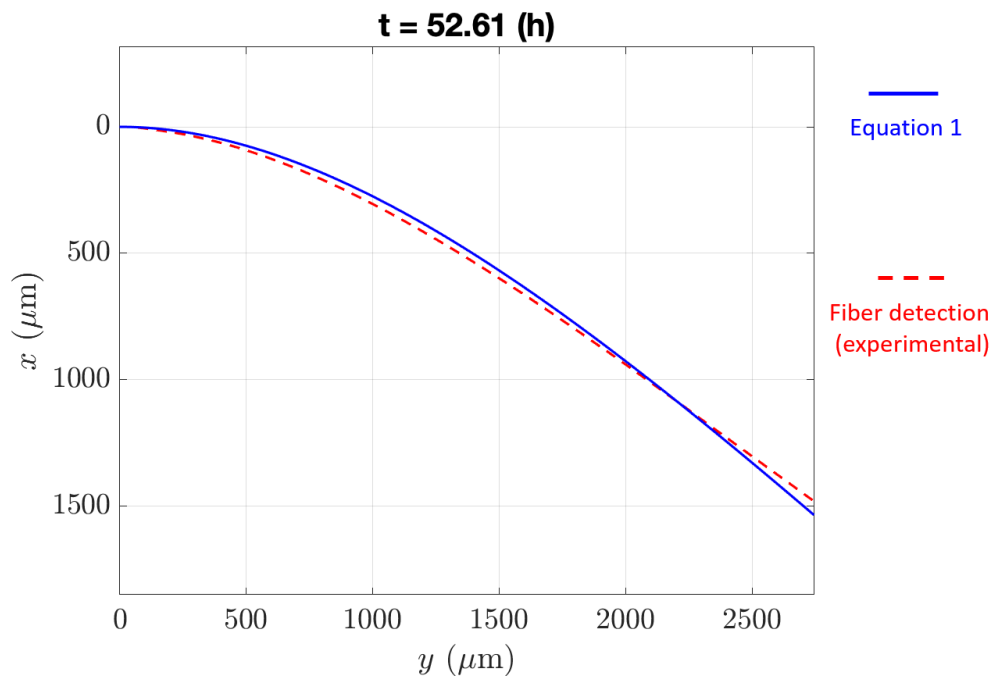


Figure 4.6. Fitting corresponding to a fiber length = 4mm at time 52,61h. The force obtained by fitting Equation 1 is $f_0 = 3.2 \text{ nN}/\mu\text{m}$.

Forces measured for different lengths of the fiber, are represented as a function of time in *Figure 4.7*. We observe that these curves show a maximum

after which, the fiber recoils. This maximum is more pronounced in the shorter fibers than in the longer ones. Notice that in the latter, its maximum value is very similar to the asymptotic deflection reached at long times.

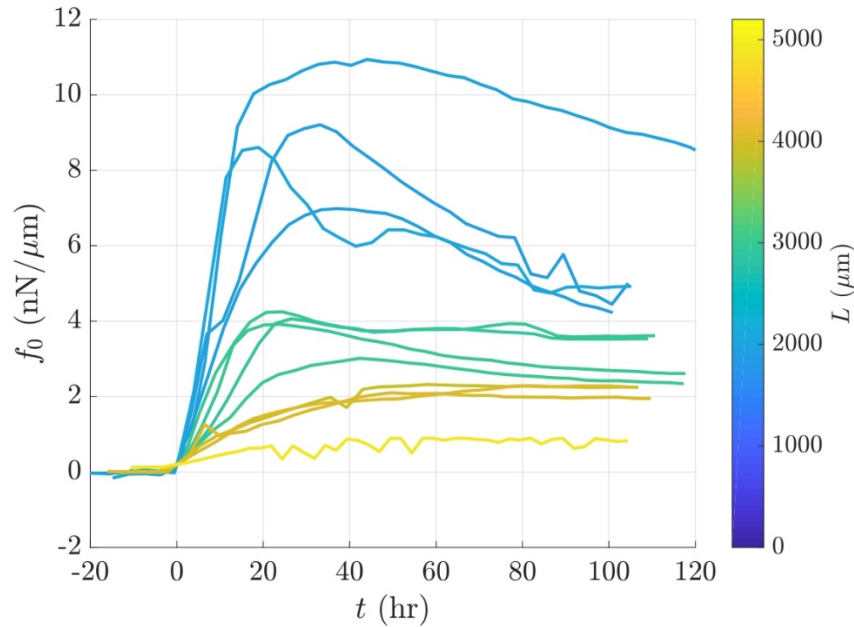


Figure 4.7. Time evolution of the uniform force per unit length for different fiber lengths. Color Scale: length of the fiber. $t = 0$: time at which the monolayer reaches the fiber.

In order to analyze the time evolution of the streamwise velocity, $u(x, t)$, and correlate it with the deflection of the fiber and the stop of the monolayer we plotted kymographs (Figure 4.9), representing the time evolution of this magnitude at three different vertical fields (Figure 4.8 as A, B and C).

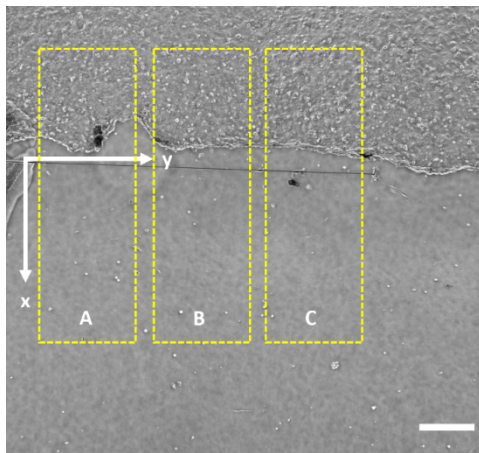
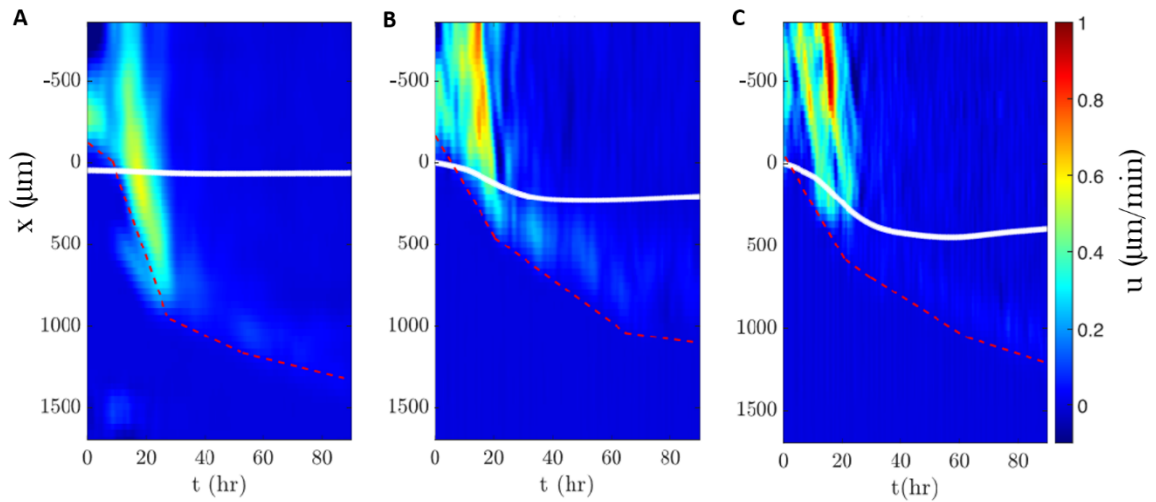
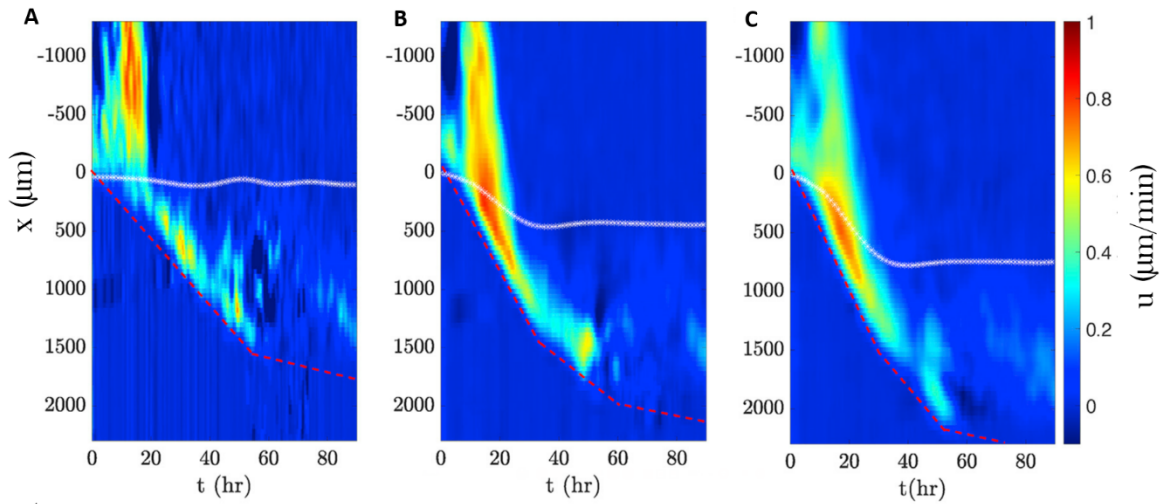


Figure 4.8. Wound healing assay at time $t = 0$. $L = 3\text{mm}$. X axis: direction of collective cell migration. Y axis: parallel to the undeformed fiber at the beginning of the experiment. Yellow dashed regions A, B and C: regions used to obtain A, B and C plots in Figure 4.9. Scale bar= $500\ \mu\text{m}$

CF = 2mm



CF = 3mm



CF = 4mm

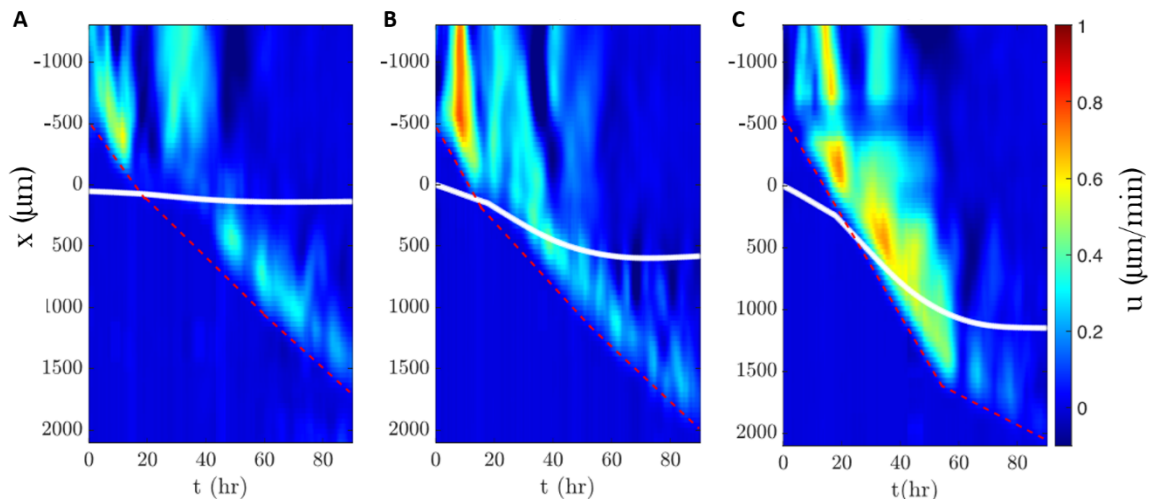


Figure 4.9. Kymographs. Colormap: Time evolution of the streamwise velocity field $u(x, t)$ at three different locations (Columns A, B and C), shown in Figure 4.8 as A, B and C. **White thick line:** Fiber deflection. **Red dashed line:** front of the monolayer. **CF=.**Length of the carbon fiber: 2mm, 3mm and 4mm for the upper, middle, and bottom rows respectively. Velocity values are positive along the x axis (in the direction of migration).

From these kymographs it can be observed that the monolayer stops when the fiber reaches its maximum deflection. After this maximum, the fiber starts to recoil and the force decreases

Note that cells that overpass the carbon fiber, continue migrating even after the fiber has reached its maximum deflection. However, the number of cells that have migrated downstream the fiber is considerably smaller than that upstream and therefore the cell density is there smaller. For this reason, the force with which these cells pull from this position is negligible compared to that of the cells that are pushing at the center of the monolayer (*Figure 4.10*).

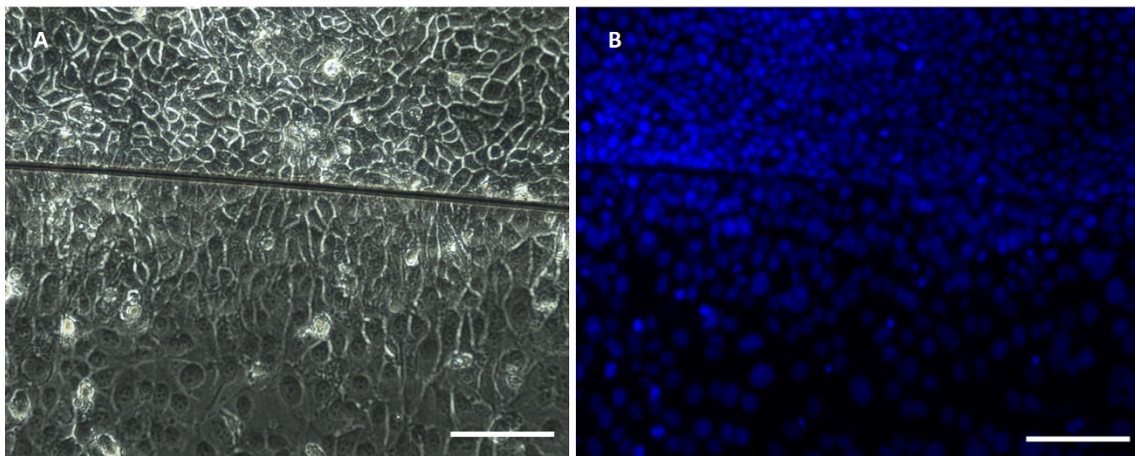


Figure 4.10. Migrating cell monolayer fixed at time = 48h. A. Brightfield image. B. Nuclear staining with DAPI (Blue). Carbon fiber is visualized as a black line. Scale bar = 100 μm .

To support this claim, a cell density analysis was performed, both by bright-field microscopy and by staining cell nuclei with fluorescent DAPI, in order to easily visualize the actual number of cells regardless of how much they spread. The corresponding quantitative analysis of the DAPI image is shown in *Figure 4.11*.

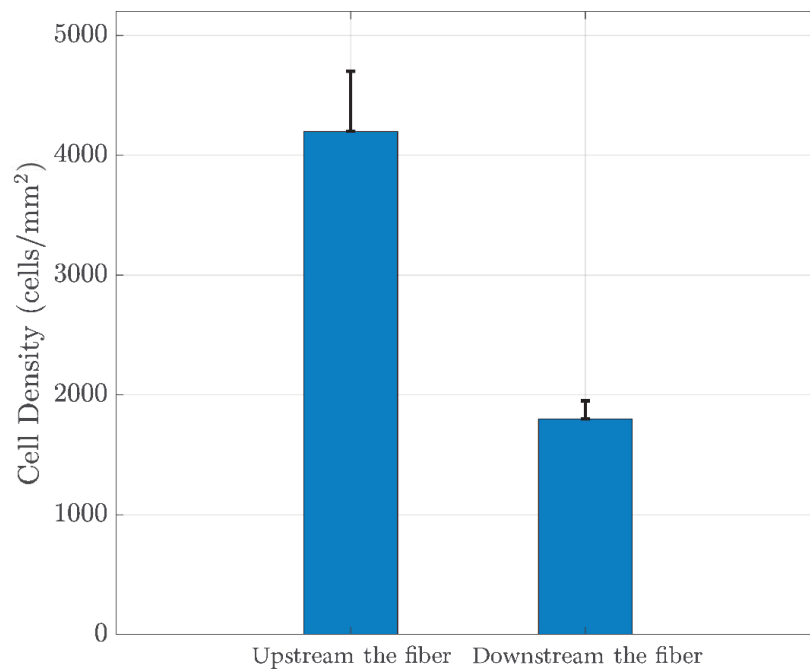


Figure 4.11. Cell density analysis of Figure 4.10. (Number of cells/mm²). Left bar: number of cells upstream the fiber. Right bar: number of cells downstream the fiber.

4.6 Model formulation

In this work, we aim to develop a **minimal model** which describes the physical interaction between a migrating cell monolayer and a flexible carbon fiber of known properties that opposes its progress. Keeping this in mind, we discard the modelling of the full motion of the monolayer, which would entail the approach of a much more complicated model that is not within our goals.

For this purpose, we propose a **one-dimensional model** that considers the cell monolayer as a **compressible active fluid** with **velocity field $u(x,t)$** .

Our experimental results suggest that the fiber-monolayer system behaves as a **damped harmonic oscillator**, close to the critical damping. That means that comparing both systems we find that they exhibit the same features.

To be more explicative, we have represented *Figure 4.12*.

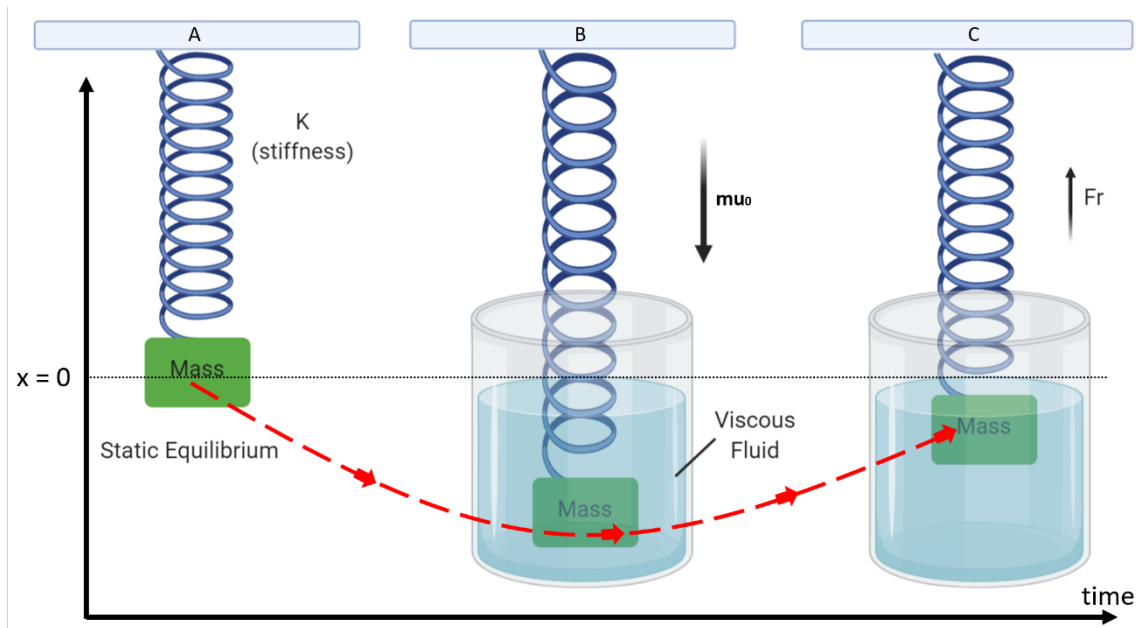


Figure 4.12. Damped harmonic oscillation. K = stiffness of the spring A. Static Equilibrium. B and C. System in motion. Red dashed line: path of the oscillation. Fr : restoring force. μ_0 , Impulse. $x = 0$: origin of the position (equilibrium point). This is a self-created illustration, using www.Biorender.com.

In *Figure 4.12.A*, a mass is hanging from a spring (**spring-mass system**) and it stretches some distance, reaching a **static equilibrium** where there is no motion (**equilibrium point: $x=0$**). Then, a force is applied to the mass and therefore, the spring is stretched downwards (*Figure 4.12.B*). When the mass is left free, the spring-mass system is going to oscillate up and down (**system in motion**) in a straight line along x -axis. The **restoring force** of the spring (Fr), tries to restore the mass to its equilibrium point, causing an acceleration (*Figure 4.12.C*). These oscillations describe curves (**red dashed line**). Here, as it is a **damped** harmonic oscillator, a **friction** provided by a viscous fluid opposes the motion of the system, which reduces the amplitude of the motion until reaching an equilibrium position. This explanation is useful to understand the behavior of our fiber-monolayer system.

Thus, the *Equation 4.2* describes a damped harmonic motion. The term on the left accounts for the inertia effect: mass (m) times acceleration (a). Note that the acceleration is: $a = \ddot{x} = d^2x/dt^2$. The first term on the right, $-kx$, corresponds to the restoring force of the spring and $-\beta\dot{x}$, is the damping force, where $\dot{x} = dx/dt$. Then, the net force (ma) is equal to the force of the spring

and the damping force. The direction of both restoring and damping forces which depends on the sign of the displacement (x) and the velocity(\dot{x})³⁴.

$$m\ddot{x} = -kx - \beta\dot{x}$$

Equation 4.2. Equation for damped harmonic oscillators. m = mass. \ddot{x} = acceleration. k = spring constant or stiffness factor. x = displacement. β = damping factor. \dot{x} = velocity.

The damped harmonic motion varies depending on the amount of damping. Thereby, when the damping is low (**underdamped**), the system oscillates and the amplitude of the motion decays (*Figure 4.13. Red dashed line*). If the damping is so high that the system does not oscillate and reaches an asymptote, the system is said to be **overdamped** (*Figure 4.13. Blue line*). Finally, **critical damping** occurs when the system slowly returns to its equilibrium position without overshooting it (*Figure 4.13. Green dashed line*).

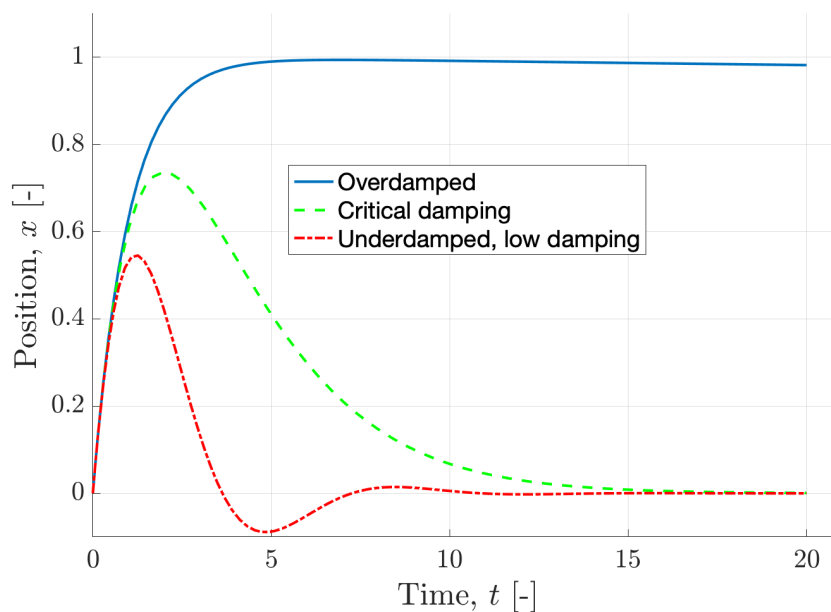


Figure 4.13. Damped harmonic motion. Overdamped (blue line). Critical damping (green dashed line). Underdamped (red dashed line). This is a self-created illustration.

Oscillations depicted in *Figure 4.13* are representative of those described by the fiber-monolayer system in the experiments (*Figure 4.7*). Initially the fiber is pushed by the cells, causing a fiber deformation at a nearly constant velocity,

causing a displacement from its initial position. It progressively slows down until it reaches a maximum deflection (Figure 4.14). Then, the shorter fibers **slowly recoil** describing an underdamped oscillation with high damping, which is close to but under the critical damping (underdamped, with high damping), whereas the longer ones **asymptotically** approach the maximum deformation and keep it until the end of our experiments (overdamped).

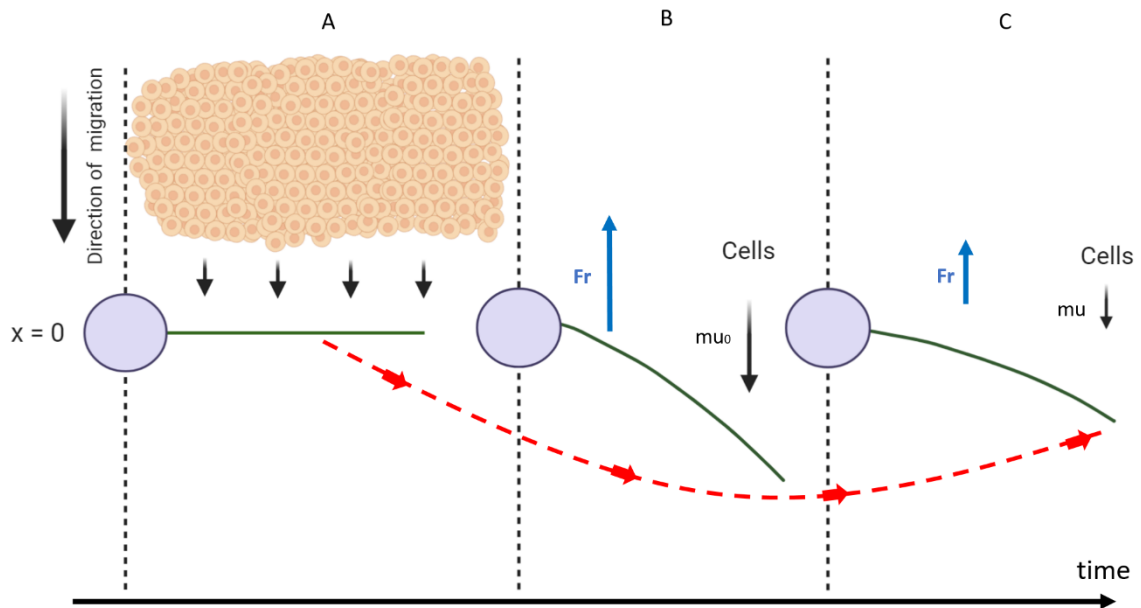


Figure 4.14. Fiber-monomer system progression over time. A. Initial time. Cells have not yet touched the fiber. B. Cells have pushed the fiber until a maximum deflection. C: After the maximum deformation, the fiber slowly recoils (example of a short fiber deformation). μ_0 and μ . Impulse. Fr. Restoring force. Red dashed line. Path of the oscillation.

This is a self-created illustration, using www.Biorender.com.

Thus, our system describes a nearly critically damped oscillation or overdamped oscillation depending on the length of the fiber. Keeping this in mind, we model the fiber-monomer system by incorporating an effective inertia, a Hookean linear force exerted by the fiber on the tissue and Newtonian viscous stresses (Equation 4.3).

$$m \left(\frac{\partial u}{\partial t} + u \frac{\partial u}{\partial x} \right) = -kx_f \delta[x - x_f] + \mu \frac{\partial^2 u}{\partial x^2}$$

Equation 4.3. Fiber monolayer system equation. m = effective inertia. u = velocity. t = time. x = front of the monolayer. x_f = position of the fiber. k = elastic constant.

4.6.1 Terms of the fiber-monolayer system equation

- **First term:**

$$m \left(\frac{\partial u}{\partial t} + u \frac{\partial u}{\partial x} \right)$$

This term from the [Equation 4.3](#), is equivalent to the resistance of cells to change their state of motion, that is an **inertia-like term**²¹. This is called “effective inertia” because its origin is different from the actual inertia, commonly used in mechanics. The effective inertia, m , can be attributed to the time that cells require to rearrange their cytoskeleton in order to change their polarization, as ideas from other research works suggest³⁵. We have also applied the material derivative $D/Dt = \partial/\partial t + u \partial/\partial x$ ³⁶, as we computed the acceleration of a field that includes both spatial and temporal variations. As the system can vary in time and space, we compute the derivative with respect to the two variables to analyze how the position of the system evolves.

- **Second term:**

$$-kx_f \delta[x - x_f]$$

This first term on the right side of the [Equation 4.3](#), corresponds to the **elastic force** exerted by the fiber, which is proportional to a deflection, x_f , times the bending stiffness, k . From [Equation 4.1](#)

[Equation 4.1](#), we can infer the relationship between stiffness and the length of the fiber: $k = \partial f_0 / \partial x_f \sim EI/L^4$

In this case, we have introduced the effect of the fiber as $\delta[x - x_f]$. This function is equal to zero everywhere except for $x = x_f$, meaning that the force is only applied at that point.

- **Third term:**

$$\mu \frac{\partial^2 u}{\partial x^2}$$

Finally, the third term of the equation accounts for **viscous stress**, whose origin comes from friction between moving cells. We have modeled this effect as in Blanch-Mercader et al³⁵. Then, μ , is a constant that measures the viscosity of the tissue, and $\partial^2 u / \partial x^2$, is a velocity field. We do not consider here, for simplicity, the cell-substrate friction. Its effect is expected to be less important close to the fiber, were velocity gradients ($\partial u / \partial x$) are large.

4.6.2 Boundary conditions

In order to solve our model computationally, we need to apply a series of mathematical modifications. Since there is a spatial dependence of the variables, we need to establish some boundaries for that spatial domain and define how the system behaves at those limits.

The system has two boundaries: the carbon fiber and the computational limit that we set, where we expect velocities to be independent of the position. Then, we establish the boundary conditions to those limits.

- **Velocity is uniform at a distance “ ℓ ” from the fiber.**

Reasonably far from the fiber, at a distance “ ℓ ” upstream from its initial position, the velocity is uniform in space, meaning that it does no longer depend on the position. Then, $\partial u / \partial x = 0$ at $x = -\ell$.

- **Dynamic boundary condition at the fiber.**

We already introduced the effect of the fiber through the function $\delta[x - x_f]$ of the [Equation 4.3](#). This way, we consider the forces that are exchanged at the front of the monolayer, whose position coincides with the position of the fiber $x = x_f$. There, cells receive the force exerted by the fiber.

However, this a **moving boundary**. Then, to make the equation suitable for numerical computation, we must add this condition by introducing a scaled spatial coordinate: $\xi = (x - x_f) / (\ell + x_f)$, such that $\xi(x = -\ell) = -1$ and $\xi(x = x_f) = 0$. This way, we handle a mobile domain, mapping it to a fixed mathematical domain. Then, we focus on the monolayer front and fiber surroundings to determine the monolayer behavior.

Moreover, we introduced the following **dimensionless notation**: $U = u/u_0$; $T = tu_0/L_c$; $\hat{\ell} = \ell/L_c$; $K = kL_c^3/\mu u_0$; $X_f = x_f/L_c$. This mathematical notation is applied to reduce the number of parameters of the initial equation and to facilitate the understanding of the relationship between them.

After introducing the first two boundary conditions and the dimensionless notation, we obtain *Equation 4.4*:

$$\frac{\partial U}{\partial T} + \frac{U - \dot{X}_f}{\hat{\ell} + X_f} \frac{\partial U}{\partial \xi} = -KX_f\delta[\xi] + \frac{1}{(\hat{\ell} + X_f)^2} \frac{\partial^2 U}{\partial \xi^2}$$

Equation 4.4.

- **Kinematic boundary condition.**

Finally, we need to establish which is the velocity of the front monolayer, $x = x_f$. Then, the boundary moves with the local velocity (*Equation 4.5*):

$$\dot{X}_f = U(\xi = 0)$$

Equation 4.5.

To **summarize**, after applying a dimensionless notation and three boundary conditions namely:

1. Boundary condition imposed at a distance " ℓ " from the fiber:
 - $\partial u/\partial x = 0$ at $x = -\ell$
2. Boundary conditions imposed at the front of the monolayer:
 - $x = x_f$
 - $\dot{X}_f = U(\xi = 0)$

Equation 4.2 turns into Equation 4.6.

$$\frac{\dot{X}_f^2}{2(\hat{\ell} + X_f)} + KX_f + \frac{1}{(\hat{\ell} + X_f)^2} \frac{\partial U}{\partial \xi} \Big|_{\xi=0} = 0$$

Equation 4.6.

4.7 Theoretical vs. experimental observations

To summarize, after observing how the bar is deflected over time (Figure 4.7), we chose two fluid-like behaviors to build a minimal model:

- **Inertia-like term:** cells start to migrate until they reach a constant velocity. When they touch the fiber, they do not immediately modify its velocity.
- **Viscous damping:** that represents that the fiber reaches at most only one relative maximum deflection after which it slowly recoils.

Both terms are balanced with the **elastic recovery force** of the fiber thus obtaining a qualitative description of the experimental results (Figure 4.15.B):

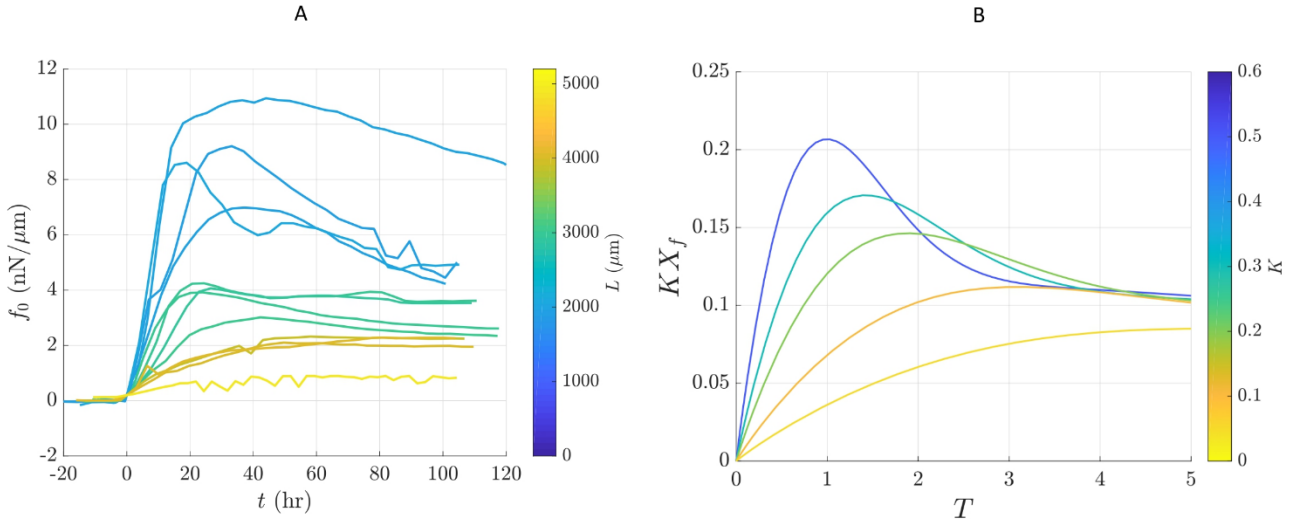


Figure 4.15. Experimental vs. Model results. A. Experimental results. Correspond to Figure 4.7: Time evolution of the uniform force per unit length for different fiber lengths. Color Scale: length of the fiber. $t=0$: time at which the monolayer reaches the fiber. B. Model results. Time evolution of the dimensionless force per unit length computed numerically for $\hat{\ell} = 5$ and $K = 0.5, 0.3, 0.2$ and 0.1 . K : Stiffness. X_f : characteristic deflection of the fiber.

From the study of the behavior of the system, we can extract the following statements:

- **Inertia and viscosity are of equal importance in the motion of the system**

This arises from the fact that the fiber deflection describes overdamped or nearly critically damped oscillations. It means that the fiber would eventually slowly return to its equilibrium position (initial position, $x = 0$) without overshooting it because **the viscosity of the tissue provides damping**. This overdamped oscillations strongly depend on the length of the fiber (then the stiffness). As we mentioned before, shorter (stiffer) fibers will experiment this recoil (*see blue color in Figure 4.15 A and B*) while the longer ones will reach an asymptotic maximum (*see yellow colors in Figure 4.15 A and B*). Recall that short fibers are stiffer than long ones, since $k = \partial f_0 / \partial x_f \sim EI/L^4$.

Then, at long times, model predicts that the monolayer stops and the fiber goes back to its equilibrium point. However, we cannot observe this recoil at times longer than 120h, due to experimental limitations, then we cannot confirm experimentally that it comes back to the initial position.

We treated the monolayer as a **viscous fluid**. From *Equation 4.3* we can infer that $L_c = \mu/mu_0$ can be chosen as the length scale of the flow. This means that L_c is the length of the tissue where the effect of the fiber is felt most strongly. In this region, inertia and viscous friction are of the same order of magnitude and enter in balance with the force exerted by the fiber. Outside this region, the effect of the fiber is still noticeable, albeit less pronounced, for a longer distance (ℓ). In the region between L_c and ℓ , viscous friction takes care of completely damping the velocity gradients, until at $x = -\ell$, the monolayer velocity is nearly uniform (*Figure 4.16*).

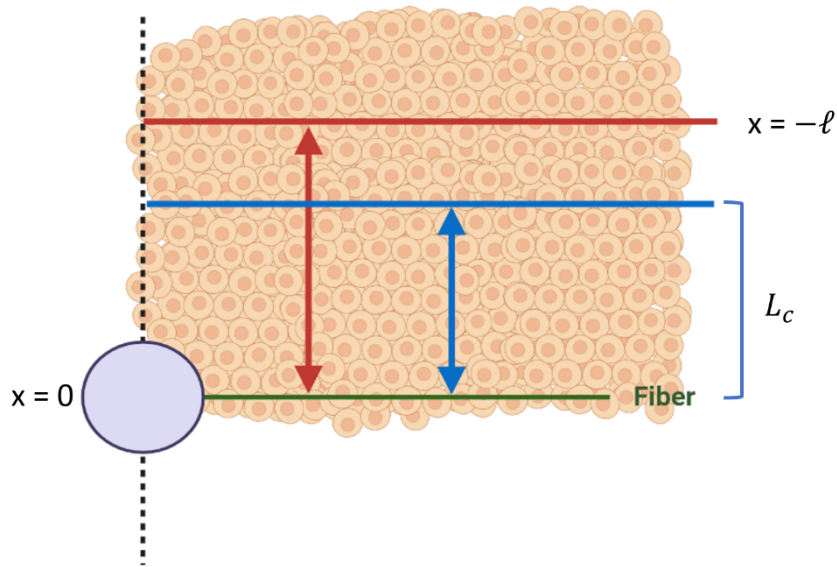


Figure 4.16. Schematic representation. L_c : size of the region where inertia and viscosity are equally important. $x = -l$: limit of the region where there is some effect of the fiber. Here velocity is uniform in space. This is a self-created illustration, using www.Biorender.com.

- **Effect of the fiber elasticity on the dynamics of the monolayer**

The only parameter that we can change in our experiments, is the fiber length (L). Since Young's Modulus (E) and moment of inertia (I) are inherent characteristics of the fibers that cannot be changed, we carried out experiments varying the length of the fibers (L).

As mentioned above, from [Equation 4.1](#) we can infer that $k \sim L^{-4}$. Thus, we could cover more than one order of magnitude by doubling the length. This is supported by the little variation in KX_f needed to obtain a high resolution in the plot ([Figure 4.15.B](#)).

If we treat the cell monolayer as an undamped oscillator, assuming that cell velocities are of the order of u_0 , and the maximum deformation of the fiber is x_{max} , then x_{max} coincides with the moment that the inertia of cells are equal to the restoring force of the fiber. Beyond that point, inertia can no longer oppose elastic forces. If we balance those terms, we get:

x_{max}^2 is given by the balance between inertia and elastic force, using Hooke's law $F = kx$:

$$\mathbf{Inertia = Elastic\ force}$$

$$\mathbf{Inertia: } ma = m u_0/t_c = m u_0^2/x_{max}$$

$$\mathbf{Elastic\ force: } f_{0,max} = kx_{max}$$

$$kx_{max} \sim m u_0^2/x_{max}$$

$$x_{max}^2 \sim m u_0^2/k$$

Recalling that $k \sim EIL^{-4}$, we replace x_{max} and k in the elastic force equation to obtain:

$$f_{0,max} \sim \frac{m^{1/2} u_0 (EI)^{1/2}}{L^2}$$

Equation 4.7. Equation of force

From [Equation 4.7](#), we establish the relationship between the force and the length of the fiber, which are inversely related. This prediction is in very good agreement with the experimental measurements represented in [Figure 4.17](#).

According to this, we found that the stronger the resistance of the environment, the stronger the force cells are able to exert. This behavior is commonly observed in mechanotransduction³⁷. In our model, the effective inertia makes cells push the fiber at their initial velocity independently of the obstacle they reach, whereby modulating its force. This happens until this inertia is balanced by the elastic force exerted by the fiber. Thus, at short times, this velocity does not depend on the stiffness of the fiber: the stiffer the fiber the stronger the force cells exert on it.

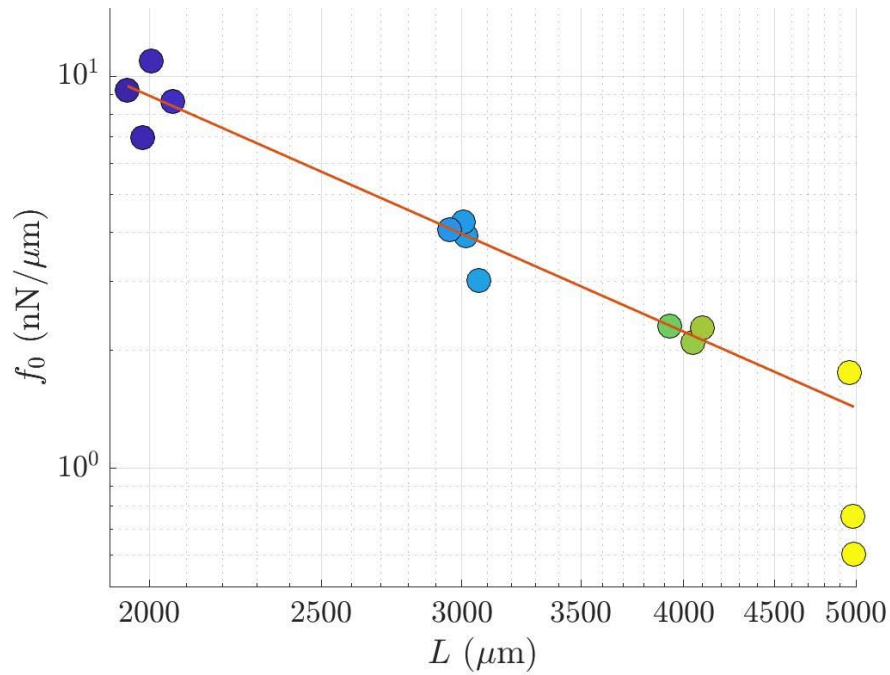


Figure 4.17. Maximum force measured in experiments corresponding to different fiber lengths. Each point corresponds to a single experiment. Color code indicates the length of the fiber used in each experiment. Solid red line: fit with a power law $f_{0,max} \sim Cf \times L^{-2}$. $Cf \approx 3.57 \times 10^7 \text{ nN}\mu\text{m}$

- Relationship between the maximum elastic energy, maximum deflection and force.

In a mechanical system, energy is equal to the product of force times distance. Starting with the force, we have calculated in Equation 4.7, we obtain Equation 4.8:

$$E_{max} \sim f_{0,max} x_{max} \sim k x_{max}^2 \sim \mu u_0^2$$

Equation 4.8. Equation of energy.

Then, we expect the maximum elastic energy per unit length accumulated by the fiber, E_{max} , to be nearly independent of its stiffness, whereby, fibers with different lengths, should present the same amount of energy (that transmitted by cells).

This prediction is contrasted in Figure 4.18. It works reasonably well, except for the longest fibers ($L= 5\text{mm}$, in yellow). It can be attributed to the fact that the hypotheses of uniform force, cell velocity, etc. do not work for the longest fibers.

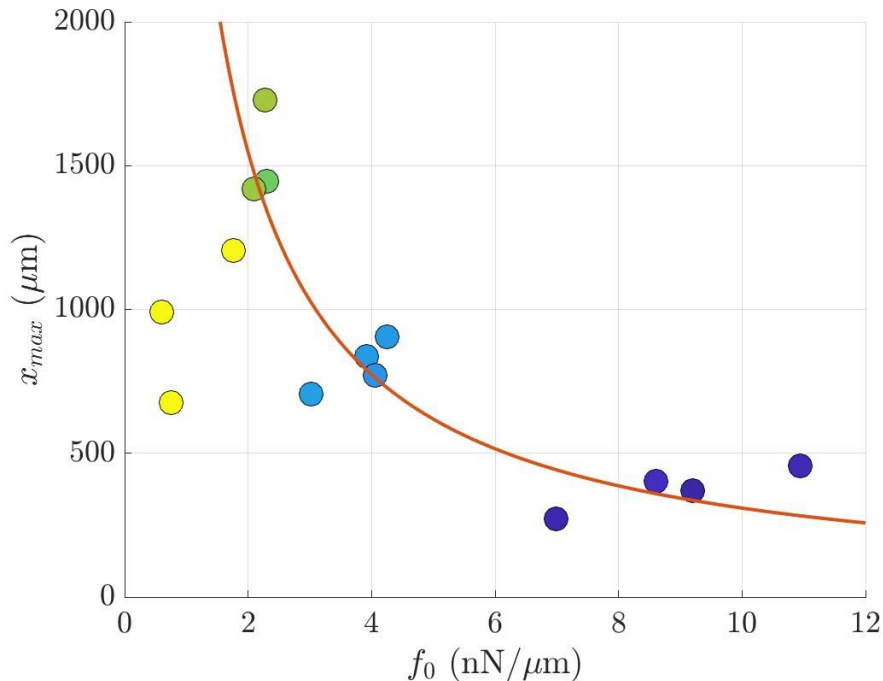


Figure 4.18. Maximum fiber deflection ($x_{max} = f_{0,max}/k$) as a function of the maximum force, $f_{0,max}$. Color code indicates the length of the fiber used in each experiment. Solid line: maximum deflection inversely proportional to the maximum force, $x_{max} f_{0,max} \approx 3.1 \times 10^3 nN$

From these arguments, the following **hypothesis** arises: independently of the fiber stiffness, cells exert a certain work on the fiber, meaning that they deposit the same mechanical energy in all cases. After spending a given amount of energy, cells stop moving.

4.8 Discussion

Cells exchange biochemical and mechanical signals with their surrounding extracellular environment establishing a two-way communication that regulates biological processes. The mechanical forces received or exerted by the cells, are transmitted through cellular structures and molecules, and translated into biochemical signals in a process called mechanotransduction, which modulates normal cell behavior. A change in the mechanical properties of the environment or a dysregulation of mechanotransduction signals may favor the progression of certain diseases and pathological conditions, such as cancer, asthma, chronic wounds or muscular dystrophy, which are related to abnormal cellular or tissue mechanics^{1,38}. In this regard, force cytometry tools

and computational models have been developed to a better understanding of the mechanisms by which mechanical forces regulates physiological and pathological processes^{6,7,8,9,10,11}. However, most of the organs and tissues of interest are three-dimensional structures and the few existing 3D force measurement techniques still present some limitations^{4,18}.

Thereby, we aimed to develop an affordable and reproducible force measurement technique, based on a carbon fiber that acts as a cantilever pushed by a migrating monolayer of keratinocytes. According to the obtained results, we transferred the *in vitro* results to mathematical relationships to build a physical model that helps us to extract information on the biological behavior of the tissue. Both experimental setup and model formulation are characterized by a reduced complexity, considering the essential elements needed to describe and reproduce the most important characteristics of our system. Thus, we built an active-fluid model that outline how the tissue modulate the forces it exerts depending on the compliance of its external surroundings.

The experiments conducted are based on wound healing assays, where a 3D- printed stencil specifically designed for our experimental configuration, was used to generate a damage-free wound. Upon the removal of the stencil from the cell culture, the cell monolayer is released and exposed to a free edge that triggers cell migration. As cell monolayer moves forward, it reaches the carbon fiber in its path and pushes it at nearly constant speed, causing the fiber deflection. Further on the velocity slows down eventually reaching a maximum deflection. After that, the fiber recoils and the monolayer stops (*Figure 4.9*). This observed pattern led us to model the system as a harmonic oscillator around the critical damping.

Keeping in mind our main purpose of creating a minimal model, we include in it the essential elements for the description of the observed behavior, specifically: effective inertia, viscous stress between cells and an elastic force opposed by the fiber. Thus, balancing the inertia-like term and viscous stress with the elastic recovery force, we obtained a qualitative description of the fiber-

monolayer system that allow us to extract information that is summarized below.

The viscous fluid behavior exhibited by the tissue is responsible of the overdamped fiber oscillations meaning that inertia and friction are equally important in the region affected by the fiber.

Conversely, the fiber stiffness also influences on the dynamics of the monolayer. To assess that, we tested different lengths of the fiber in the experiments, since stiffness and length are inversely related. Then, as the moment of maximum deflection of the fiber coincides with the moment that the inertia of cells is equal to the restoring force of the fiber, we balance the inertia and elastic force of the fiber. Thereby we obtain the equation for the force (*Equation 4.7*), that establishes an inverse relationship between the force and the length of the fiber to the square. This prediction is in good agreement with the experimental results (*Figure 4.17*), and resembles the behavior described in mechanotransduction: the stronger the resistance of the environment, the stronger the forces exerted by cells³⁷.

Finally, an interesting hypothesis arose from the last finding from our experiments. We observed that cells exert a certain mechanical work, which is constant for all fiber lengths. Thereby, the fiber accumulates the same maximum elastic energy per unit length for all cases, regardless of its stiffness. This led us to the conclusion that, under our experimental conditions, the limitation of the tissue to keep expanding against an external obstacle, is not so much the force to be exerted as the associated work to be done.

In this regard, we aim to test this hypothesis and correlate the results with the model's prediction (*see chapter 7 Future perspectives*).

To conclude, we expect our force measurement technique to be adaptable to three dimensional environments and hence to be useful for the improvement and development of 3D measurement techniques. Furthermore, the simplicity of our model allows an easier interpretation and could be used to be introduced in other more complex descriptions of collective cell behaviors. This would allow

them to characterize cellular interactions with external compliant elements, and compare different cellular populations while isolating the role of mechanical forces^{21,22,23}.

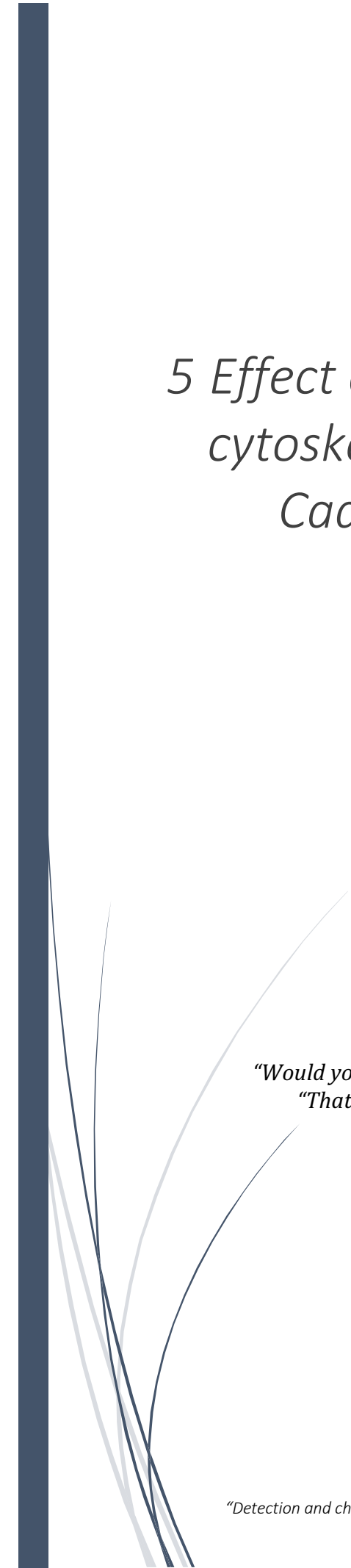
Finally, our method constitutes an affordable, reproducible, and easy to implement technique that, together with the model, can be applied to describe 2D scenarios (i.e. skin and cornea wound healing) that are representative of some physiological and pathological situations.

This work has been published on 2nd February 2021 (Valencia and López-Llorente et al. *Biophysical Journal*)³⁹.

1. Moendarbary, E. & Harris, A. R. Cell mechanics: Principles, practices, and prospects. *Wiley Interdiscip. Rev. Syst. Biol. Med.* **6**, 371–388 (2014).
2. Dua, H. S. & Forrester, J. V. The Corneoscleral Limbus in Human Corneal Epithelial Wound Healing. *Am. J. Ophthalmol.* **110**, 646–656 (1990).
3. Wang, T. *et al.* Downregulation of miR-205 in migrating epithelial tongue facilitates skin wound re-epithelialization by derepressing ITGA5. *Biochim. Biophys. Acta* **1862**, 1443–1452 (2016).
4. Angelo, A. D., Dierkes, K., Carolis, C. & Salbreux, G. In Vivo Force Application Reveals a Fast Tissue Softening and External Friction Increase during Early Embryogenesis. *Curr. Biol.* **May**, **6**, 1564–1571 (2019).
5. Rizzuti, I. F. *et al.* Mechanical Control of Cell Proliferation Increases Resistance to Chemotherapeutic Agents. *Phys. Rev. Lett.* **125**, 1–7 (2020).
6. Dembo, M. & Wang, Y. Stresses at the Cell-to-Substrate Interface during Locomotion of Fibroblasts. *Biophys. J.* **76**, 2307–2316 (1999).
7. du Roure, O. *et al.* Force mapping in epithelial cell migration. *Proc. Natl. Acad. Sci.* **102**, 2390–2395 (2005).
8. Butler, J. P., Tolic--Nørrelykke, I. V. A. M., Fabry, B. E. N. & Fredberg, J. J. Traction fields, moments, and strain energy that cells exert on their surroundings. *Am J Physiol Cell Physiol* **282**, 595–605 (2002).
9. Del Alamo, J. C. *et al.* Spatio-temporal analysis of eukaryotic cell motility by improved force cytometry. *Proc. Natl. Acad. Sci. U. S. A.* **104**, 13343–8 (2007).
10. Trepap, X. *et al.* Physical forces during collective cell migration. *Nat. Phys.* **5**, (2009).
11. Tambe, D. T. *et al.* Collective cell guidance by cooperative intercellular forces. *Nat. Mater.* **10**, 469–475 (2011).
12. Legant, W. R. *et al.* Measurement of mechanical tractions exerted by cells in three-dimensional matrices. *Nat. Methods* **7**, 969–971 (2010).
13. Thorsten M. Koch¹, Stefan Munster, Navid Bonakdar, James P. Butler, B. F. 3D Traction Forces in Cancer Cell Invasion. *PLoS ONE* **7**, (2012).
14. Campàs, O. *et al.* Quantifying cell-generated mechanical forces within living embryonic tissues. *Nat. Methods* **11**, 183–189 (2014).
15. Sugimura, K., Lenne, P. & Graner, F. Measuring forces and stresses in situ in living tissues. *Co. Biol. Ltd* **143**, 186–196 (2016).
16. Bambardekar, K., Clément, R., Blanc, O., Chardès, C. & Lenne, P. Direct laser manipulation reveals the mechanics of cell contacts in vivo. *PNAS* **112**, 1416–1421 (2015).
17. del Álamo, J. C. *et al.* Three-Dimensional Quantification of Cellular Traction Forces and Mechanosensing of Thin Substrata by Fourier Traction Force

- Microscopy. *PLoS One* **8**, (2013).
18. Chen, T., Saw, T. B., Mege, R. M. & Ladoux, B. Mechanical forces in cell monolayers. *J. Cell Sci.* **131**, (2018).
 19. Ladoux, B. & Mège, R. M. Mechanobiology of collective cell behaviours. *Nat. Rev. Mol. Cell Biol.* **18**, 743–757 (2017).
 20. Alert, R. & Trepant, X. Physical Models of Collective Cell Migration. *Annu. Rev. Condens. Matter Phys.* **11**, 77–101 (2020).
 21. Banerjee, S., Utuje, K. J. C. & Marchetti, M. C. Propagating Stress Waves during Epithelial Expansion. *Phys. Rev. Lett.* **114**, 1–5 (2015).
 22. Tlili, S. *et al.* Collective cell migration without proliferation: Density determines cell velocity and wave velocity. *bioRxiv* (2017). doi:10.1101/232462
 23. Moitrier, S. *et al.* Collective stresses drive competition between monolayers of normal and Ras-transformed cells. *Soft Matter* **15**, 537–545 (2019).
 24. Guillot, C. & Lencuit, T. Mechanics of Epithelial Tissue Homeostasis and Morphogenesis. *Science* **340**, 1185–1189 (2013).
 25. Valencia, L. Characterizing the mechanical response of epidermal cell monolayers during wound healing. (Carlos III University of Madrid, 2017).
 26. Poujade, M. *et al.* Collective migration of an epithelial monolayer in response to a model wound. *Proc. Natl. Acad. Sci. U. S. A.* **104**, 15988–15993 (2007).
 27. Ravasio, A. *et al.* Gap geometry dictates epithelial closure efficiency. *Nat. Commun.* **6**, (2015).
 28. Avérus, L., & Pollet, E. *Biodegradable Polymers. Green Energy and Technology.* (2012). doi:doi:10.1007/978-1-4471-4108-2_2
 29. Petitjean, L. *et al.* Velocity Fields in a Collectively Migrating Epithelium. *Biophysj* **98**, 1790–1800 (2010).
 30. Arakawa, Y. *et al.* Low concentration fluoride stimulates cell motility of epithelial cells in vitro. *Biomed. Res.* **30**, 271–277 (2009).
 31. H. P. Ng, S. H. Ong, K. W. C. Foong, P. S. G. and W. L. N. Medical Image Segmentation Using K-Means Clustering and Improved Watershed Algorithm. *2006 IEEE Southwest Symp. Image Anal. Interpret.* 61–65 (2006).
 32. Bert Nitzsch, Volker Bormuth, Corina Bräuer, Jonathon Howard, Leonid Ionov, Jacob Kerssemakers, Till Korten, Cecile Leduc, Felix Ruhnau, S. D. Studying kinesin motors by optical 3D-nanometry in gliding motility assays. *Methods Cell Biol.* **95**, 247–71 (2010).
 33. Timoshenko, S. *Strength of materials: Part I of Strength of materials,*

- Second Edition*. (D. Van Nostrand Company, New York, 1940).
34. Chaudhuri, R. N. *Waves and Oscillations, Second Edition*. (New age international publishers, 2010).
 35. Blanch-Mercader, C. *et al.* Effective viscosity and dynamics of spreading epithelia: a solvable model. *Soft Matter* **13**, 1235–1243 (2017).
 36. Batchelor, G. K. *An Introduction to Fluid Dynamics*. Cambridge University Press (Cambridge University Press, 2000). doi:10.1063/1.3060769
 37. Hoffman, B. D., Grashoff, C. & Schwartz, M. A. Dynamic molecular processes mediate cellular mechanotransduction. *Nature* **475**, 316–323 (2011).
 38. Rodriguez, M. L., McGarry, P. J. & Sniadecki, N. J. Review on cell mechanics: Experimental and modeling approaches. *Appl. Mech. Rev.* **65**, (2013).
 39. Valencia & López-Llorente et al. Interaction of a Migrating Cell Monolayer with a Flexible Fiber. *Biophys. J.* **120**, 1–8 (2021).



5 Effect of the carbon fiber on actin cytoskeleton rearrangements and Cadherin-mediated cell-cell adhesion

*"Would you tell me, please, which way I ought to go from here?"-said Alice
"That depends a good deal on where you want to get to," said the Cat.
[...]
"...you're sure to get somewhere," said the Cat,
"if you only walk long enough."
(Alice's adventures in Wonderland, Lewis Carroll)*

5.1 Adherens junctions mechanosensing and cytoskeletal rearrangements in migrating cells

Collective cell migration begins with the polarization of a group of cells that, in response to a biochemical or mechanical stimulus, acquire a migratory phenotype characterized by **front-rear asymmetry**. Thus, two functionally distinct morphologies are established in the cell population: leader and follower cells. **Leader cells** extend protrusions and bind to the ECM through integrin at the front and contracts the actomyosin cytoskeleton at the back. Both **actin** retrograde flow produced by the formation of the actin filaments that push the cell membrane forward and actomyosin contractions at the contractile units (CUs)¹, are transmitted to the substrate through integrin-mediated focal adhesions, thus generating **traction forces** that facilitate cell body translocation^{2,3} (*see chapter 2 general introduction*). These forces are in turn transmitted through integrins to the actin cytoskeleton, triggering intracellular signals that respond to ECM composition and rigidity (mechanosensing) by means of **cytoskeletal rearrangements** and cell polarization⁴.

Cadherins are transmembrane molecules that form adhesions between cells in a Ca^{+2} -dependent manner. They are the main components of adherens junctions (AJs) that bind to the cytoskeleton through a protein complex (p120, α -catenin and β -catenin, among others). That way, the **mechanical tension** is **transmitted** from the cytoskeleton to the cell-cell complex and causes a conformational change in the actin-binding protein α -catenin. This allows the binding of vinculin to α -catenin leading to a subsequent cell-cell complex reinforcement and local cytoskeletal rearrangement (**cortical stiffening**).

Cadherin extracellular domain of adjacent cells interact with each other (*trans*-interactions) and adopt a lattice-like lateral organization which allow *cis*-interactions between cadherins from the same cell. This facilitates the formation of **cadherin clusters** at nascent adhesion sites which associate through actin bundles at their intracellular domain forming a **mature junction** (*Figure 5.1*)^{5,6,7,8}.

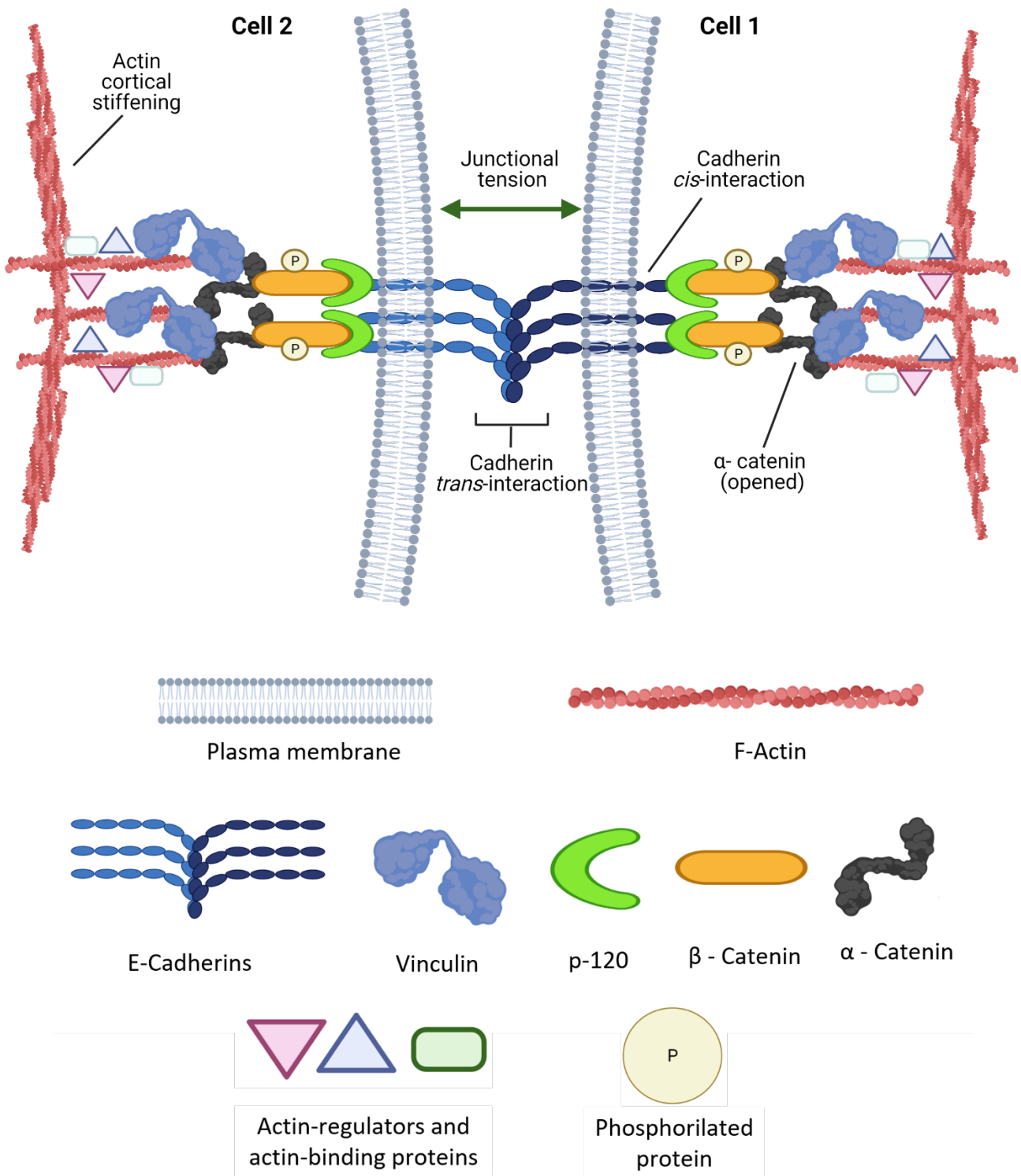


Figure 5.1. Engaged Adherens junction. This is self-created illustration, using www.Biorender.com.

Therefore, AJs connect the cytoskeleton of neighboring cells, establishing a dynamic and coordinated **multicellular actin network** (mechanical coupling between cells). They play an important role in the generation and maintenance of the polarization of cells inside the tissue⁸.

The **mechanosensitive** properties of AJs, makes cadherins the key players in the transmission of intercellular forces through the connection of longitudinal actin bundles several rows behind the migrating front, thus controlling the long-range monolayer dynamics⁹.

Hence, the association of the cadherin adhesome to F-actin cytoskeleton constitutes a **highly dynamic complex** that provides the cell with certain plasticity to withstand interactions with its surroundings⁵.

On this basis, we considered in first instance, both actin and E-cadherin (as one of the major cadherins expressed in epithelium)¹⁰, as good candidates to better understand the biological behavior of the cell monolayer upon interaction with the carbon fiber. The analysis was performed by immunofluorescence at several time points during force experiments.

5.2 Materials and methods

5.2.1 Cell culture and experimental setup

HaCat cells were used for the immunofluorescence assays described in the present section. Cell culture conditions and experimental configuration were performed following the protocols described in *chapter 4 (4.4.1 Cell culture, 4.4.2 Experimental setup)*

5.2.2 Immunocytochemistry

Immunocytochemistry (ICC) assays were performed on 35 mm imaging dishes with a polymer coverslip bottom (μ -Dish 35 mm, low, ibidi GmbH, Germany), with an observation area of 21mm.

Due to the special coverslip bottom, the shape of the culture dish differs from that used for regular time lapse migration assays performed in *chapter 4*. For this reason, the previous stencil design (*see chapter 4, Figure 4.2*) was slightly modified, in order to achieve the best fitting to the plate and maintain the same stencil-based wound generation method for all the experiments (*Figure 5.2*).

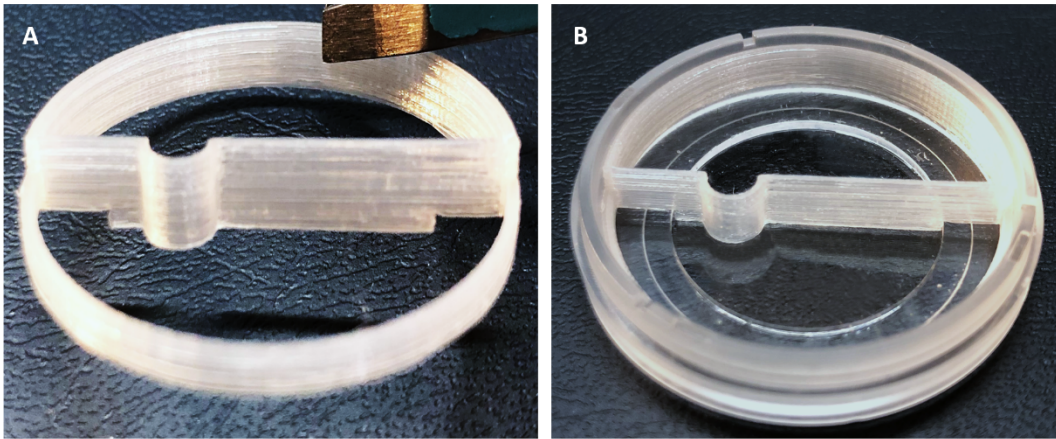


Figure 5.2. 3D printed stencil for ICC assays. A. Side view. B. Top view inside a petri dish.

After gluing the fiber and creating the wound as described in [chapter 4](#), ICCs were performed following steps described below:

- 1- Samples were **fixed** for **20 minutes** in cold **methanol/acetone (1:1)** at room temperature.
- 2- **Blocking** of non-specific interactions with 1X PBS-BSA 3% for 30 minutes at 37°C.
- 3- Incubation of the **primary antibody** diluted in PBS-BSA 3%, overnight at 4°C ([Table 5.1](#)). Fluorescent phalloxin (phalloidin) was used for actin identification (incubation for 20 minutes at room temperature).

Primary Ab	Origin / Clon	Reference	Dilution
E-cadherin	Monoclonal	BD Transduction. 610182	1:50
Phalloidin	<i>Amanita phalloides</i>	P2595 (Sigma Aldrich), coumarin labeled	1:100
Secondary Ab	Origin/Specificity	Reference	Dilution
Anti-IgG	Donkey/Mouse	Alexa Fluor 488 (Invitrogen)	1:1000

Table 5.1. References and dilutions for Phalloidin, primary and secondary antibodies.

- 4- Wash 3 times with 1XPBS
- 5- If needed, incubation of the secondary antibody (*Table 5.1*) coupled to a fluorophore, for 1 hour at room temperature in the dark.
- 6- Mounting of the samples with Mowiol (Sigma-Aldrich)/ DAPI (diamidino-2-phenyl-indole dye (0.25 ng / ml) (DAPI, Roche) for the visualization of the nuclei and containing 2,5% of 1,4-diazabicyclo[2.2.2]octane (DABCO, Sigma-Aldrich) to avoid the phenomenon of quenching or fluorescence decay.

Immunofluorescence (IF) images were obtained with an automated inverted microscope Leica Dmi8 (Leica, Wetzlar, Germany). Images were acquired with 20X and 63X magnification objectives, a Hamamatsu sCMOS Orca Flash 4.0 LT camera (Hamamatsu City, Japan), and LASX Navigator acquisition software from Leica Microsystems.

For a simpler interpretation of the fluorescence images, *Figure 5.3* represents a schematic showing of the notation used for the different areas of the cell culture that were imaged.

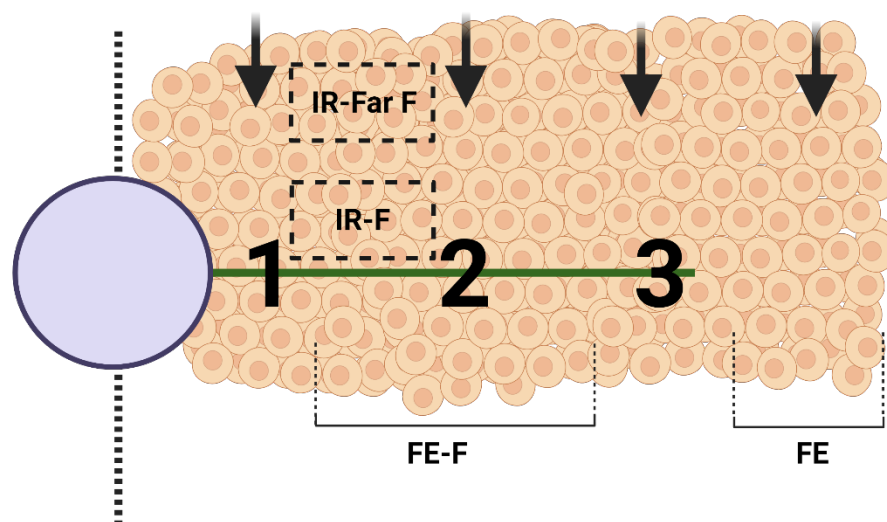


Figure 5.3. Schematic representing the notation used for immunofluorescence analysis. Green line: Carbon fiber. Black arrows: direction of migration. Blue circle: fixed end of the carbon fiber (glue drop). 1: fiber region close to the fixed end. 2: middle region of the fiber. 3: region at the fiber tip. IR-F: inner region immediately upstream the carbon fiber. IR – Far F: Inner region distant from the fiber FE-F: Cells at the front edge of the migrating tissue that have overpassed the fiber FE: Cells at the front edge of the migrating tissue that do not have overpassed the fiber This is a self-created illustration, using www.Biorender.com.

5.3 Behavior of the cell monolayer upon meeting the fiber

The fluorescent beam cannot pass through the carbon fiber, so we visualize it as a black bar. Taking advantage of this property of the fiber together with a nuclear DAPI staining, we are able to determine whether cells pass over or under the fiber.

Our experiments show that cells accumulate upon reaching the fiber, acting as a barrier to them. However, this does not prevent them from moving forward and continuing to migrate, albeit in a small number. As can be observed in DAPI images, most of the cells pass over the fiber. Nonetheless, a few of them do manage to pass underneath, being more frequent at the tip.

Figure 5.4 shows a bottom view (*Figure 5.4.A*) and a top view (*Figure 5.4.B*) of the cell culture. The respective zoom on each image is shown in the right panel, where it can be visualized that most of the cells move over the fiber to keep migrating.

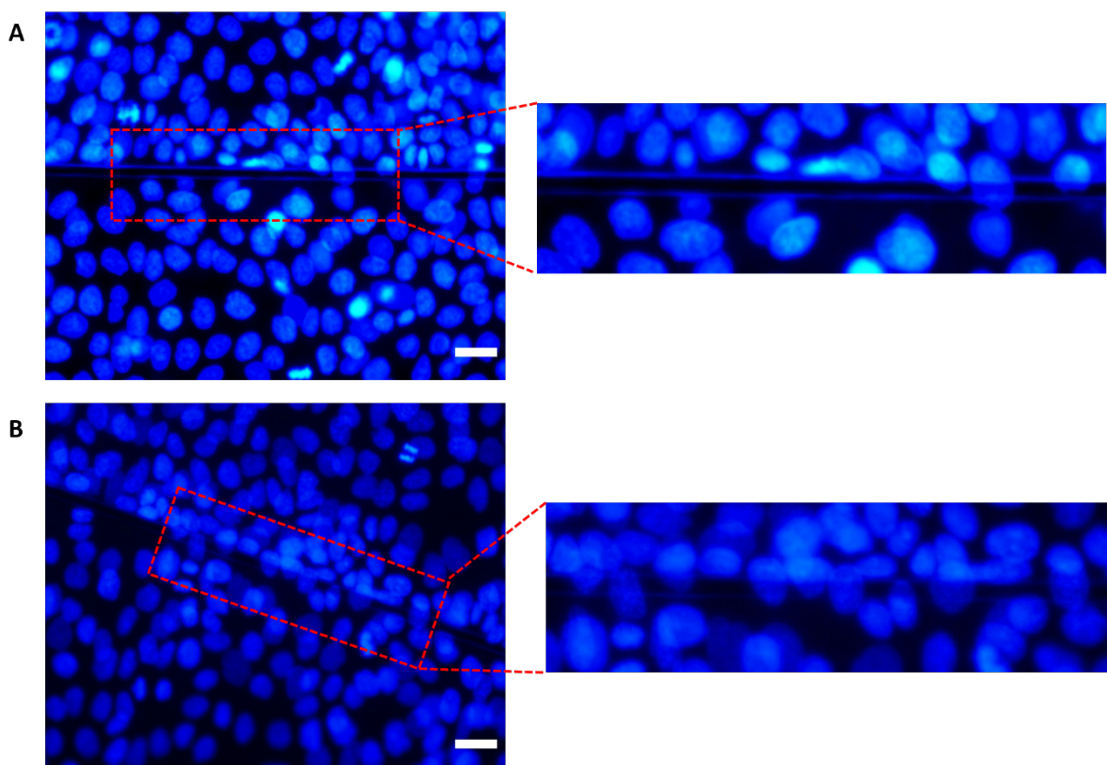


Figure 5.4. DAPI staining of migrating cells overpassing the fiber. A. Bottom view. Upper Right. Zoom on image A in the fiber area B. Top view. Lower Right: Zoom on image B in the fiber area. Scale bar= 25 μ m.

5.4 Influence of the fiber on E-Cadherin-mediated cell-cell adhesion

Immunofluorescence were used to assess changes in the subcellular distribution of E-Cadherin upon pushing the flexible fiber at fixed time points: time 0 corresponds to the day on which the wound is generated, when the cells have not yet begun to migrate. From that time on, photos were taken every 24 hours. *Figure 5.5* shows the results at 72h from wounding, as the most representative time point since cells have reached and fully bent the fiber at that moment.

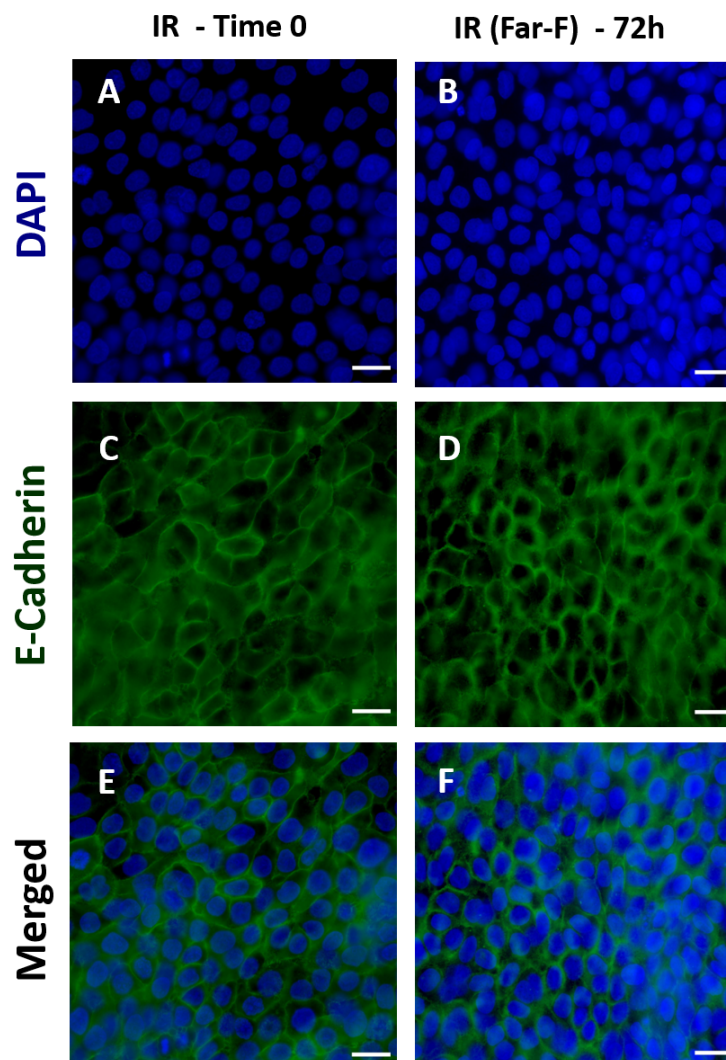


Figure 5.5. E-Cadherin cell-cell adhesion staining. From top to bottom: DAPI nuclear staining, green E-cadherin staining and color channels merged (DAPI + E-Cadherin). From left to right: IR-Time 0. Inner region of the confluent, non-migrating monolayer. IR (Far-F). Inner region of the monolayer far away from the fiber after 72h of migration. Scale bar= 25 μ m.

Figure 5.5 corresponds to a stable confluent cell culture (time 0) (*Figure 5.5.A, C, E*), and the bulk of the monolayer located at a distant region upstream the fiber (IR Far-F) after 72h of cell migration (*Figure 5.5.B, D, F*)

E-Cadherin is distributed throughout the cytoplasm as well as at the cell-cell contacts, which is characteristic of a non-cohesive steady cell culture (*Figure 5.5.C*), in contrast to a cell culture that has been migrating for 72h, which distributes E-Cadherin predominantly to the plasma membrane (*Figure 5.5. D*). This indicates an increase in tissue cohesiveness as a result of cell migration. *Figure 5.6* represents these same areas (*Figure 5.5. C and D*) magnified for better visualization. Note that, guided by the DAPI images, we have avoided focusing on areas of cell accumulation.

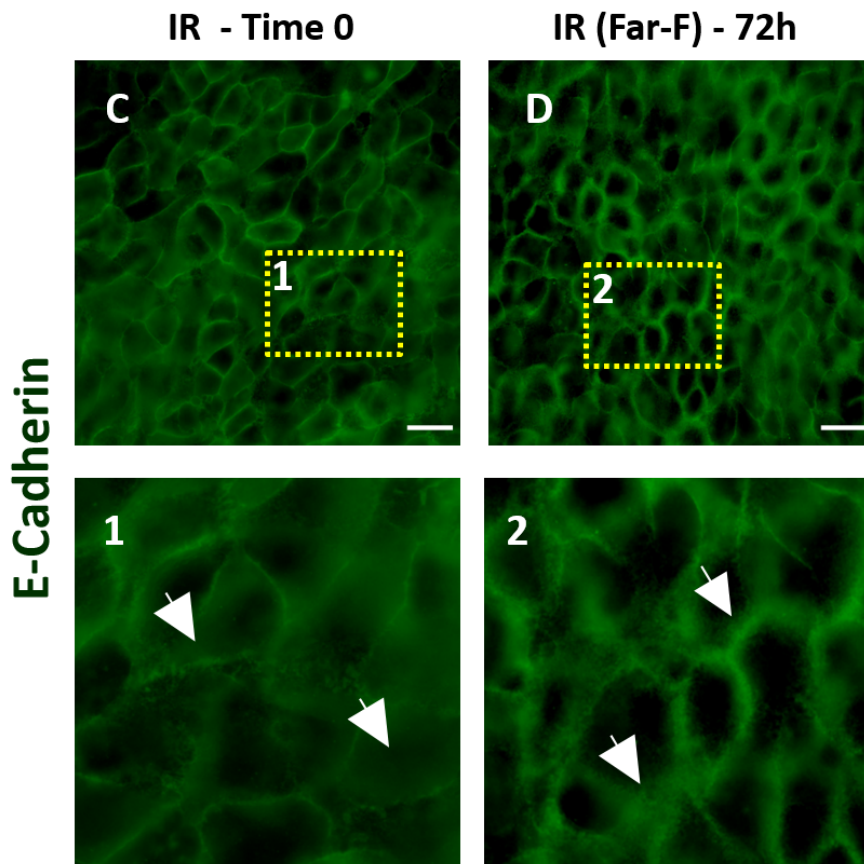


Figure 5.6. Zoom on C and D regions of Figure 5.5. Yellow dashed line: indicates zoomed areas 1 and 2. White arrows: indicate E-Cadherin cytoplasmic distribution in C-1, and E-Cadherin peripheral distribution in D-2. (Zoom =105%).

Likewise, in cells at the **leading front** (FE), E-Cadherin is fully cytoplasmic in static cell cultures (time 0) (*Figure 5.7. D*) while after 72h of migration it is

mainly located at cell-cell junctions with a weak cytoplasmic presence both in cells that have migrated freely and those that have overpassed the fiber (Figure 5.7. E, F). This is representative of the widely described intercellular tension that is transmitted from the migrating front to the inner tissue, resulting in a stress buildup that increases tissue cohesiveness, necessary to maintain its integrity during migration^{11,12}.

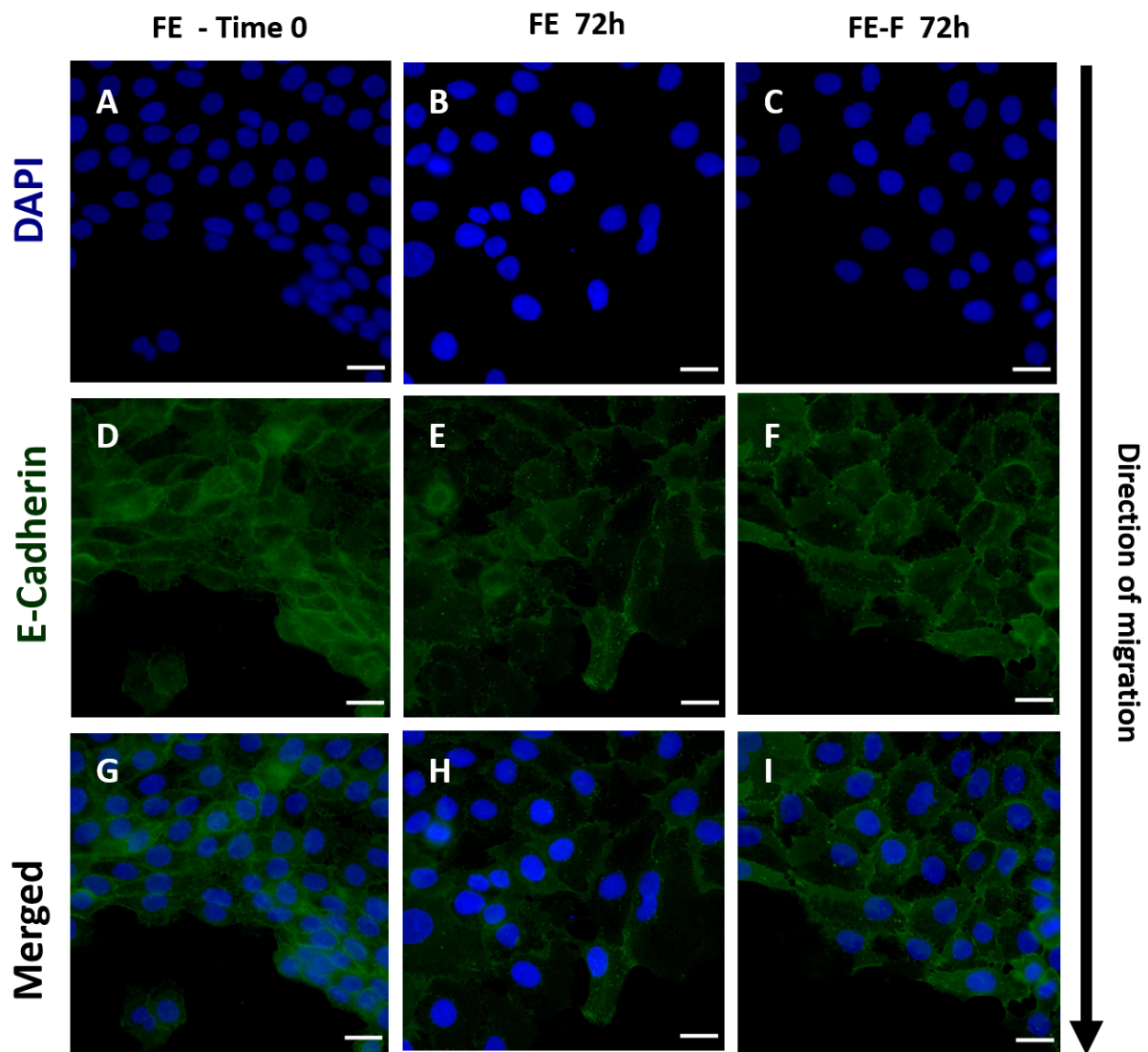


Figure 5.7. E-Cadherin cell-cell staining of the cells at the wound edge. A, D and G (FE-Time 0 column). Non-migrating cells. B, E and H (FE column). Cells at the wound edge that do not have overpassed the fiber. C, F and I (FE-F column). Cells at the wound edge that have overpassed the fiber. Scale bar= 25 μ m.

The analysis of the tissue area surrounding the fiber, showed that there is no obvious differential localization of E-Cadherin between regions located close to the fixed end (*Region 1, Figure 5.8. D*), middle of the fiber (*Region 2, Figure 5.8. E*) and at the tip (*Region 3, Figure 5.8. F*). In all three cases, the pattern distribution is similar to that observed in the inner tissue that has been migrating for 72h (*Figure 5.6. 2*).

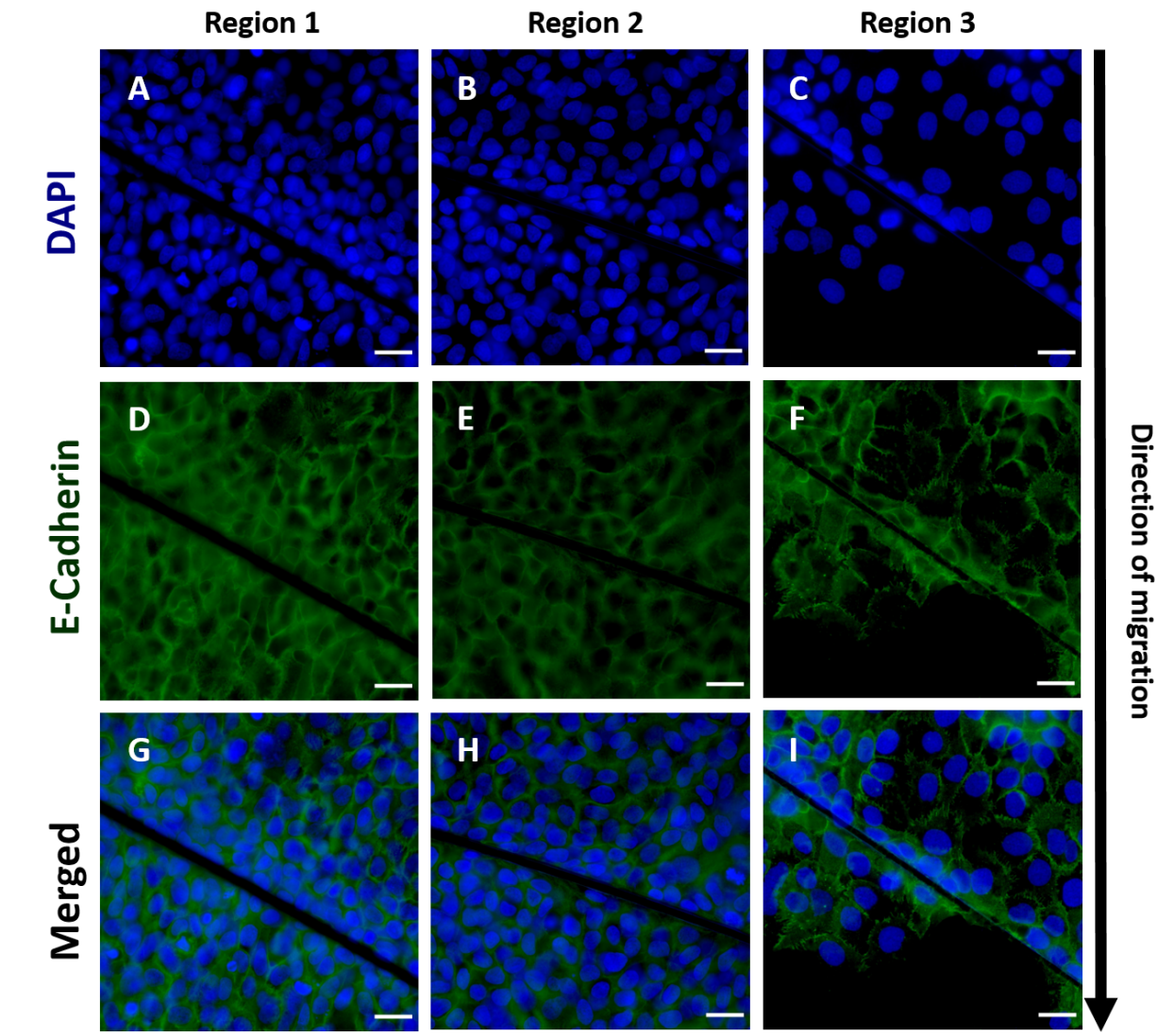


Figure 5.8. E-Cadherin cell-cell adhesion staining (72h). From top to bottom: DAPI nuclear staining, Green E-cadherin staining and color channels merged (DAPI + E-Cadherin). From left to right: fiber region 1, 2 and 3. Scale bar= 25 μ m.

For a better visualization, we show zoomed images of the regions 1, 2 and 3 (*Figure 5.9*). Here we compare the tensional state of the monolayer around the fiber and immediately upstream the fiber (IR-F). In both *Figure 5.9 A and C*, we

find a similar pattern to that obtained at the bulk of the monolayer that is far from the fiber (Figure 5.6. 2). The region corresponding to the area upstream the tip (Figure 5.9. E), is similar to that of the leading edge. Due to a lower cell density in this specific experiment, the cytoplasmic spreading upwards the fiber is larger.

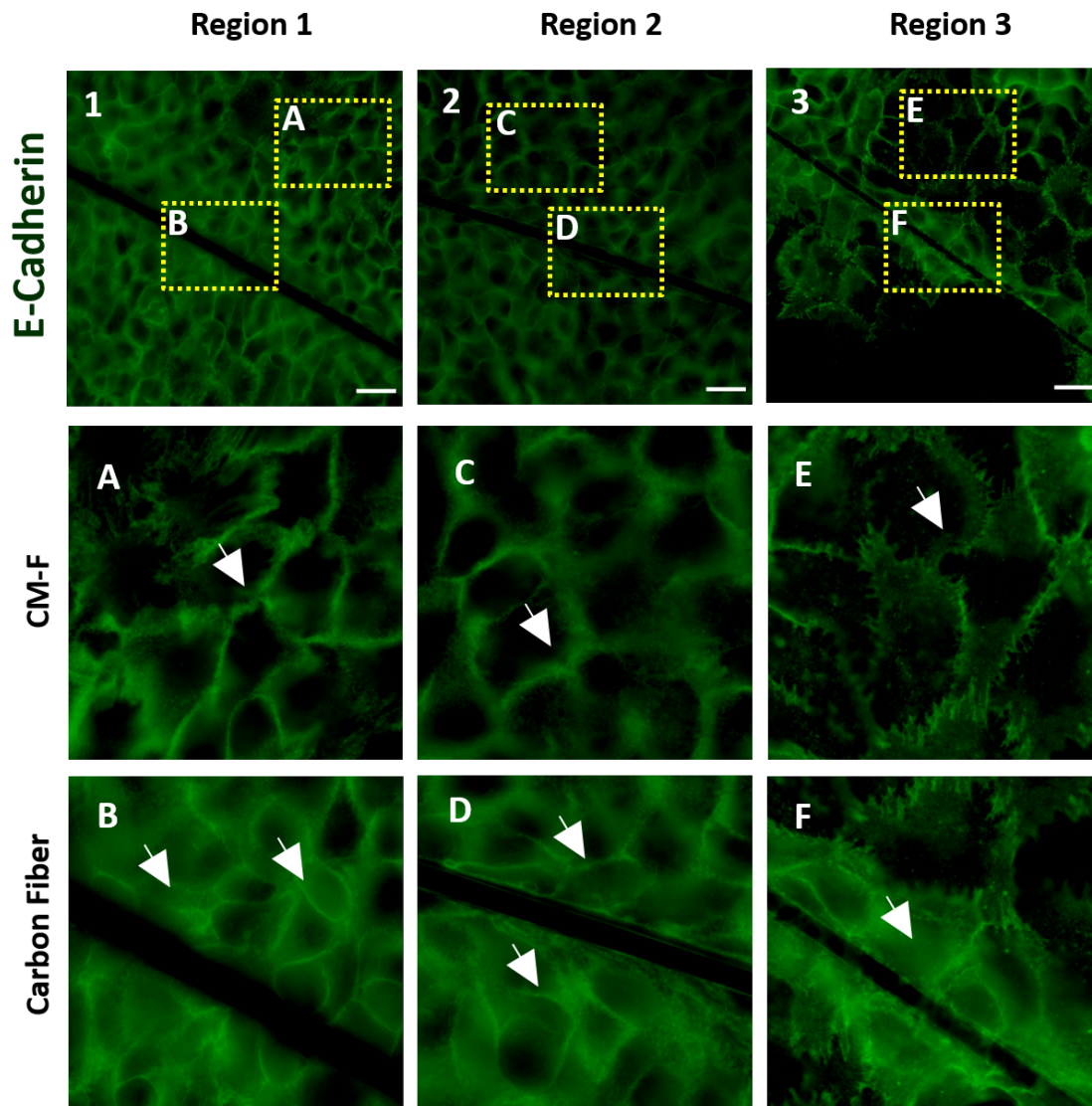


Figure 5.9. Zoom on regions 1, 2 and 3 of Figure 5.8. Upper row: Original images. Middle row: zoom on the IR (F) region. Lower row: zoom on the fiber region. IR (F): Inner region of the monolayer immediately upstream the fiber. Yellow dashed line: indicates zoomed areas below. White arrows: indicate E-Cadherin localization. (Zoom =105%)

Figure 5.9.B, D, F, shows accumulation of cells around the fiber. This precludes us from distinguish if subcellular distribution of E-Cadherin is different from that obtained in other regions.

5.5 Influence of the fiber on actin cytoskeleton rearrangement

Phalloidin is a phallotoxin isolated from *Amanita phalloides* mushroom. Its ability to bind and stabilize F-actin allows us to visualize actin polymers when conjugated with a fluorophore¹³. We used phalloidin for F-actin staining to qualitatively analyze the cytoskeleton structural reorganization of cells upon pushing the flexible fiber at fixed time points: time 0 corresponds to the day the wound is generated, when cells have not yet begun to migrate. From that time on, photos were taken every 24 hours. Here we show the results at 72h from wounding as the most representative time point since cells have reached and fully bent the fiber at that moment.

Figure 5.10. corresponds to the **inner tissue** from a stable confluent cell culture (IR-time 0) (*Figure 5.10. D*), and to two different regions of a cell culture after 72h of cell migration:

- Inner region of the monolayer located at a distant region upstream the fiber (**IR Far-F**) (*Figure 5.10.B, E, H*).
- Inner region of the monolayer located immediately upstream the fiber (**IR-F**) (*Figure 5.10.C, F, I*).

Cytoskeleton arrangement at the bulk of the monolayer at time 0, exhibits the expected cortical distribution, characteristic of steady and confluent cell monolayers (*Figure 5.10. D*). After 72h of cell migration, actin bundles along the cytoplasm are formed. The density and distribution of these actin filaments differs from the region that is far away from fiber (*Figure 5.10., E*) to the region located immediately upstream the fiber (*Figure 5.10.F*). Thus, it is possible to distinguish much more pronounced ventral stress fibers along the cytoplasm in the region that is closer to the fiber. To visualize a zoom on each image, see (*Figure 5.11*).

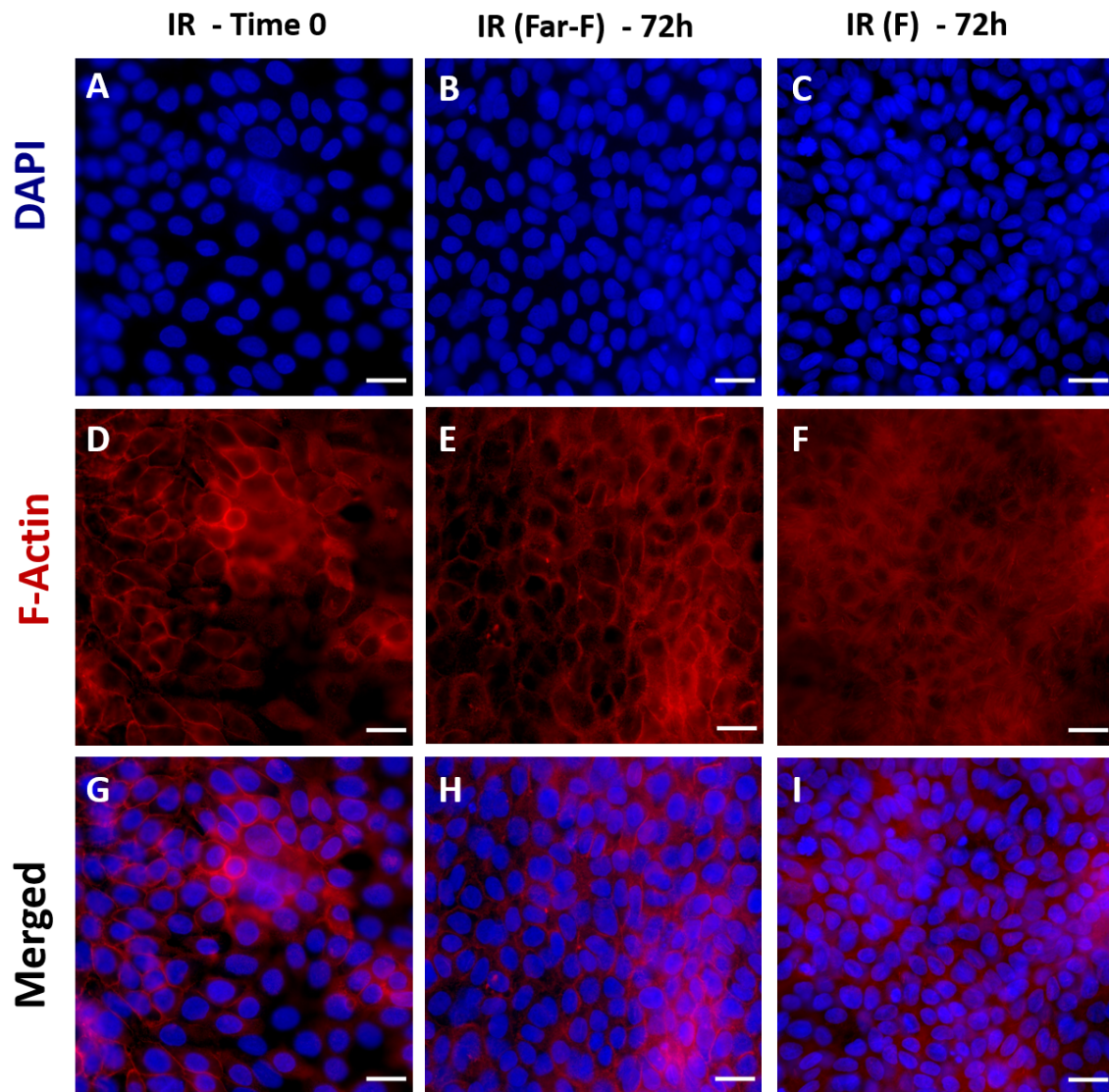


Figure 5.10. Actin cytoskeleton staining (72h). From top to bottom: DAPI nuclear staining, Red actin staining, and color channels merged (DAPI + Actin). From left to right: IR-Time 0. Center of the confluent, non-migrating monolayer. IR(Far-F). Center of the monolayer far from the fiber, after 72h of migration. IR (F). Center of the monolayer immediately upstream the fiber, after 72h of migration. Scale bar= 25 μ m.

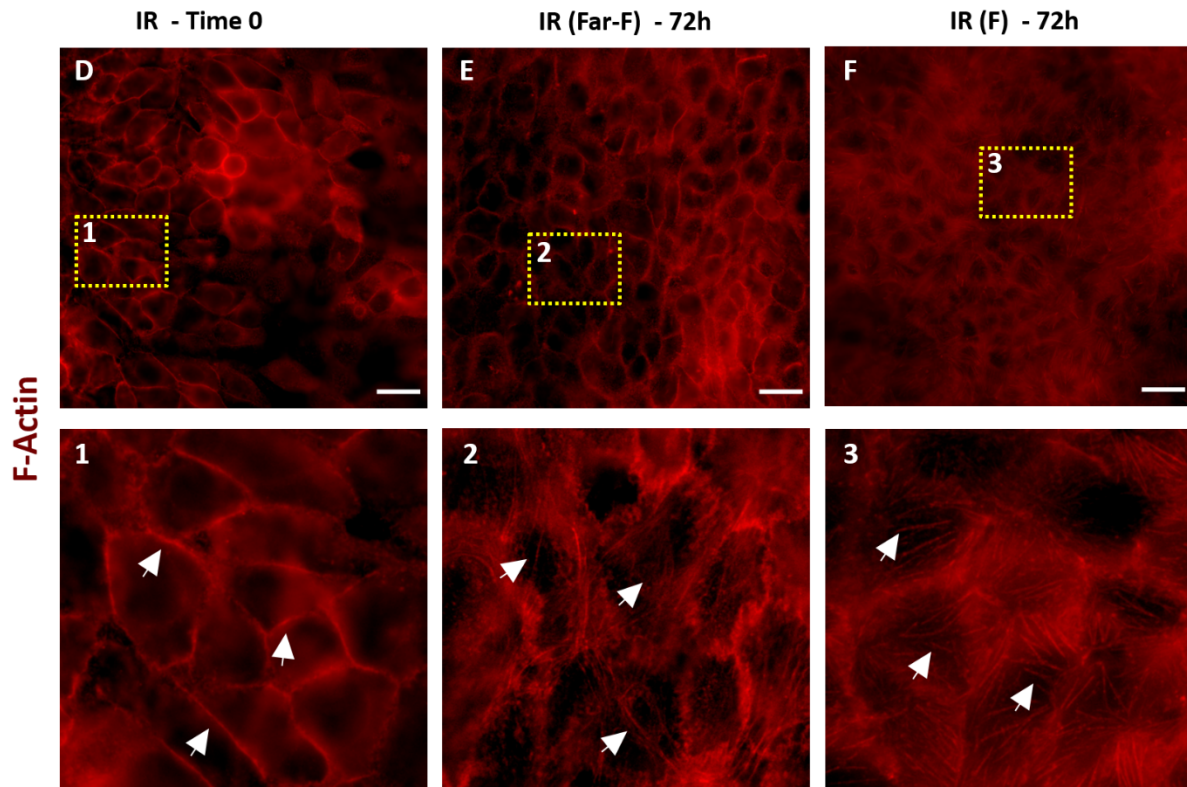


Figure 5.11. Zoom on D, E and F regions of Figure 5.10. Yellow dashed line: indicates zoomed areas below (1, 2 and 3). White arrows: indicate actin cortical distribution in D-1, and longitudinal actin bundles in E-2 and F-3. (Zoom =105%)

Cells at the **front edge of the wound (FE)**, exhibit a more diffuse cytoplasmic distribution in static cell cultures (time 0) (*Figure 5.12. D*) that differs from the already mentioned cortical localization at the center of the monolayer observed in *Figure 5.10. D*. Regarding the migratory edges at 72 hours, both those that have crossed the fiber (*Figure 5.10. E*) and those that have migrated freely (*Figure 5.10.F*), show the typical protrusions of leading fronts.

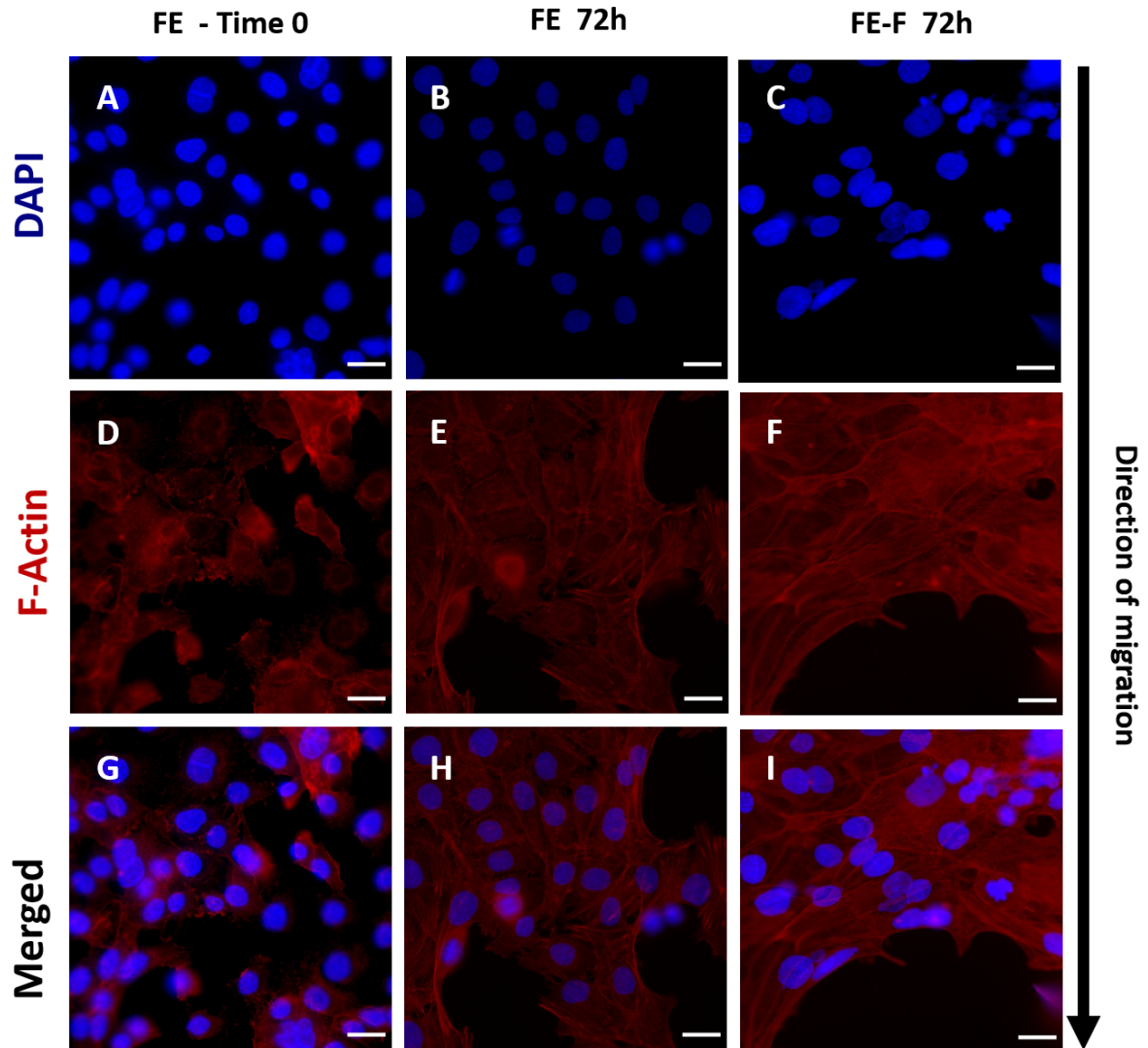


Figure 5.12. Actin cytoskeleton staining of the cells at the wound edge. A, D and G. Non migrating cells. B, E and H (FE column). Cells at the wound edge that to not have overpassed the fiber. C, F and I (FE-F column). Cells at the wound edge that have overpassed the fiber. Scale bar= 25 μ m.

However, there are differences between those who have exceeded the fiber and those who have not. *Figure 5.13* shows a zoom on *Figure 5.12. E and F* for better visualization. It can be noticed that lamellipodia extended at the front edge after having overpassed the fiber, are parallel-oriented to the front of migration (thus, parallel to the edge) (*Figure 5.13. F-2*), while lamellipodia extended at the border cells that migrated without fiber, are oriented in the direction of migration (*Figure 5.13. E-1*).

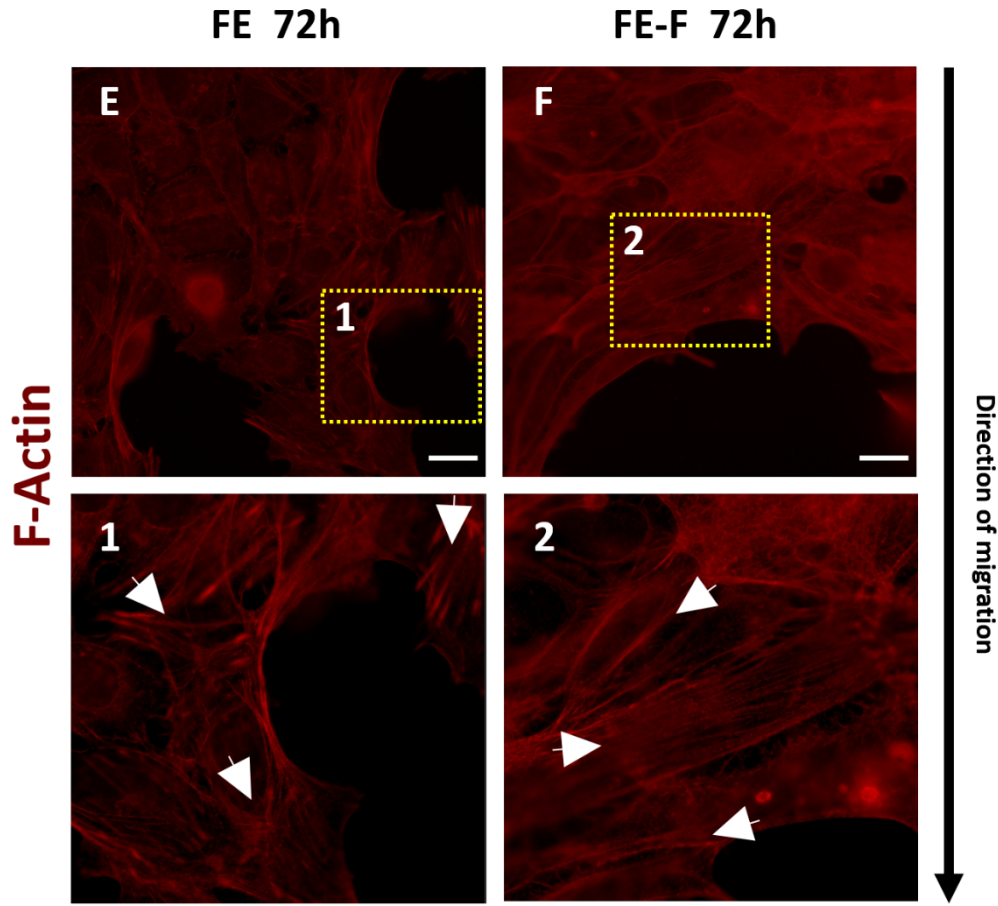


Figure 5.13. Zoom on E and F regions of Figure 5.12. FE column. Cells at the wound edge that do not have overpassed the fiber. FE-F column. Cells at the wound edge that have overpassed the fiber. Yellow dashed line: indicates zoomed areas below 1 and 2. White arrows: indicate actin orientation parallel to the migrating edge in 1, and actin orientation perpendicular to the migrating edge in 2. (Zoom =105%)

Theoretically, cells closer to the fixed end must exert a larger force than those close to the tip. Immunostaining of the region surrounding the fiber (Figure 5.14), exhibited a clear reinforcement of the cytoskeleton in places where the cells need to exert a larger force. Comparing DAPI nuclear staining of Figure 5.14., it can be observed that even though the cell density is higher in the middle region (Figure 5.14.B, E) and at the fiber tip (Figure 5.14.C, F), actin staining is more pronounced at the fixed end (Figure 5.14. A, D).

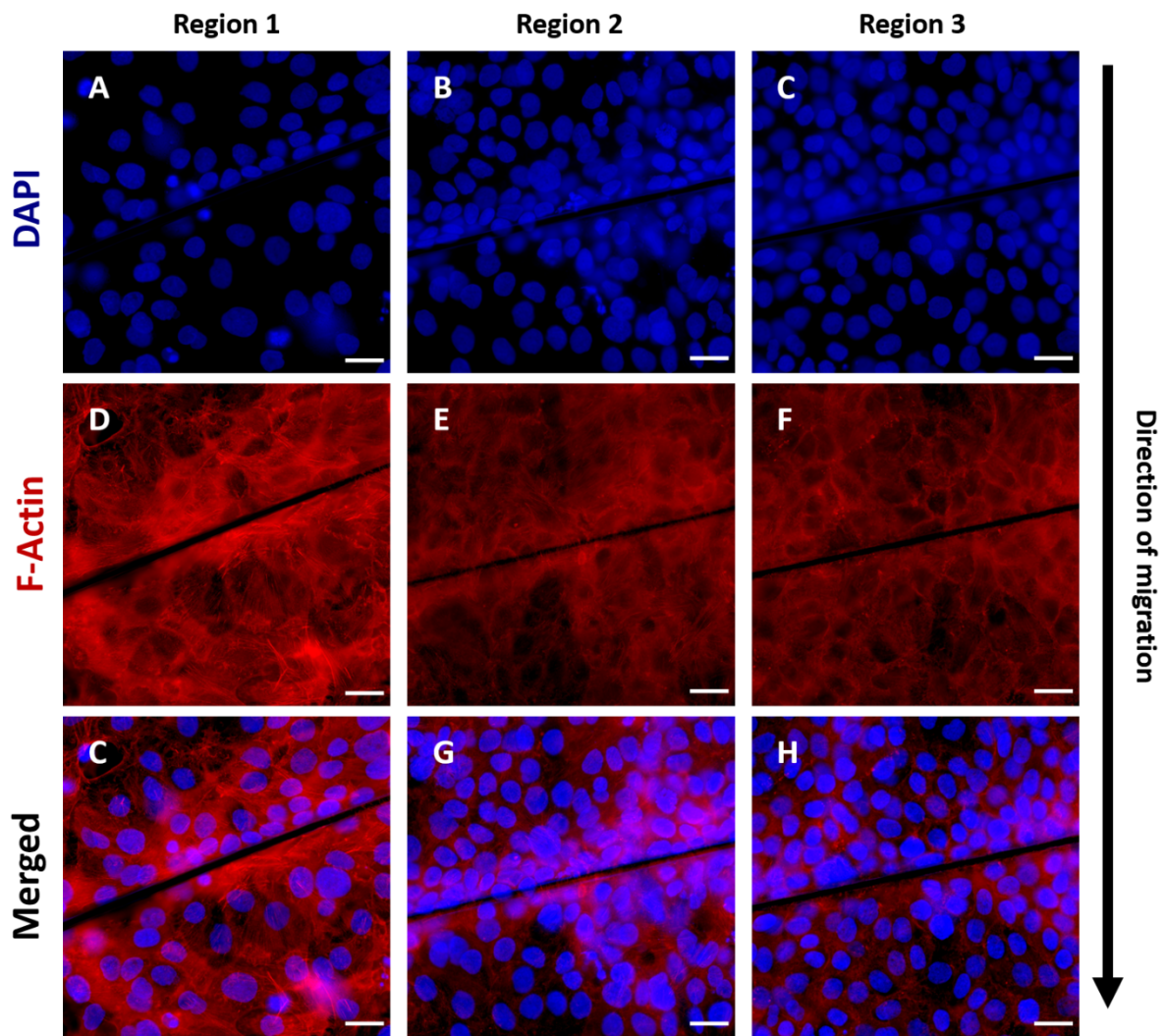


Figure 5.14. Actin cytoskeleton staining (72h). From top to bottom: DAPI nuclear staining, Red F-actin staining, and color channels merged (DAPI + F-Actin). From left to right: fiber region 1, 2 and 3. Scale bar= 25 μ m.

Respective zooms on the three regions (*Figure 5.15.*), allow an easier visualization of F- actin bundling, which is enhanced close to the fixed end of the fiber (*Figure 5.15. D-1*) presenting a cytoskeletal organization reminiscent of lamellipodial protrusions formed at the leading cells (*Figure 5.13. E-1*). Conversely, regions 2 and 3 (*Figure 5.15. E-2, F-3*), exhibit actin filaments as those found in the region immediately upwards the fiber (*Figure 5.11. F-3*), due to the high tensional state of the region and cell movement.

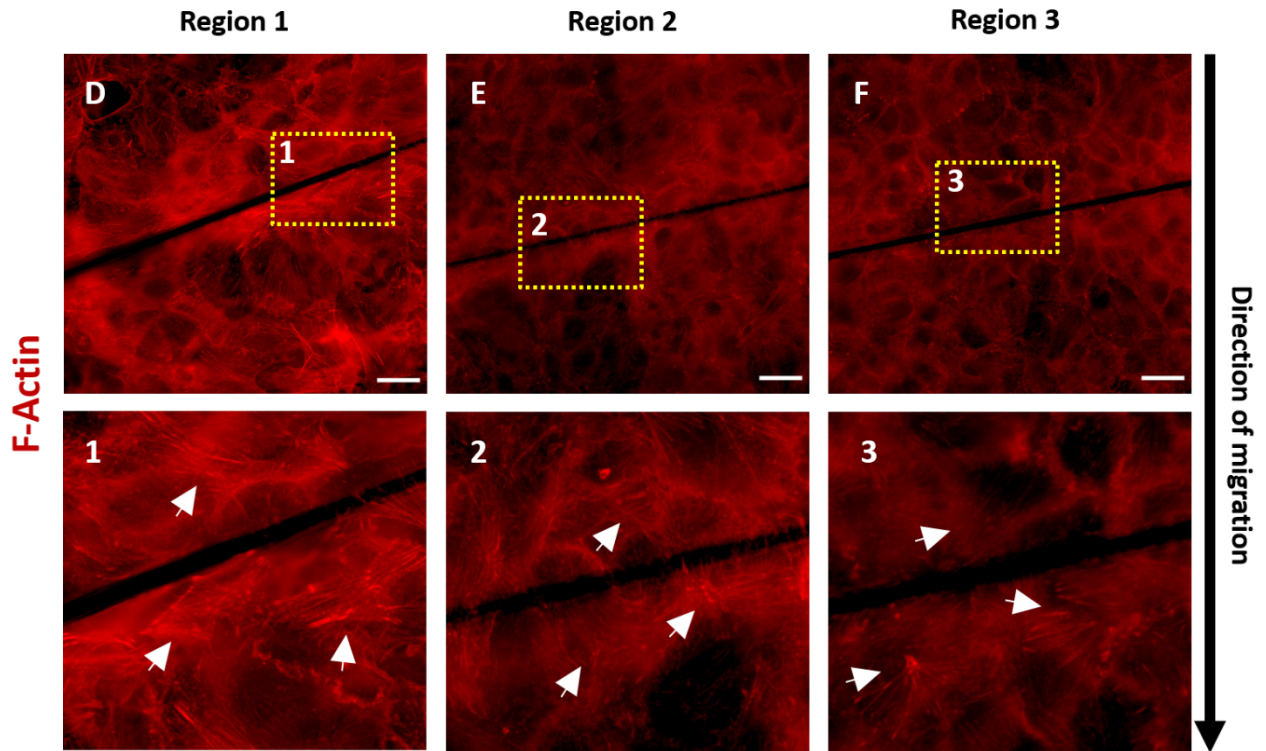


Figure 5.15. Zoom in on D, E and F regions of Figure 5.14. Yellow dashed line: indicates zoomed areas below 1, 2 and 3. White arrows: indicate strong actin bundling enhancement in 1, and longitudinal actin bundles and stress fibers in 2 and 3. (Zoom =105%)

Therefore, the cytoskeleton is considerably reinforced at region 1 (*Figure 5.14.D*) and gradually decay as the distance to the fixed end increases, showing slight differences between regions 2 and 3 (*Figure 5.14.E,.F*). This is consistent with the fact that forces applied close to the fixed position of the fiber need to be higher than those exerted at the tip.

Finally, to assess the overall state of the monolayer, we employed a lower magnification.

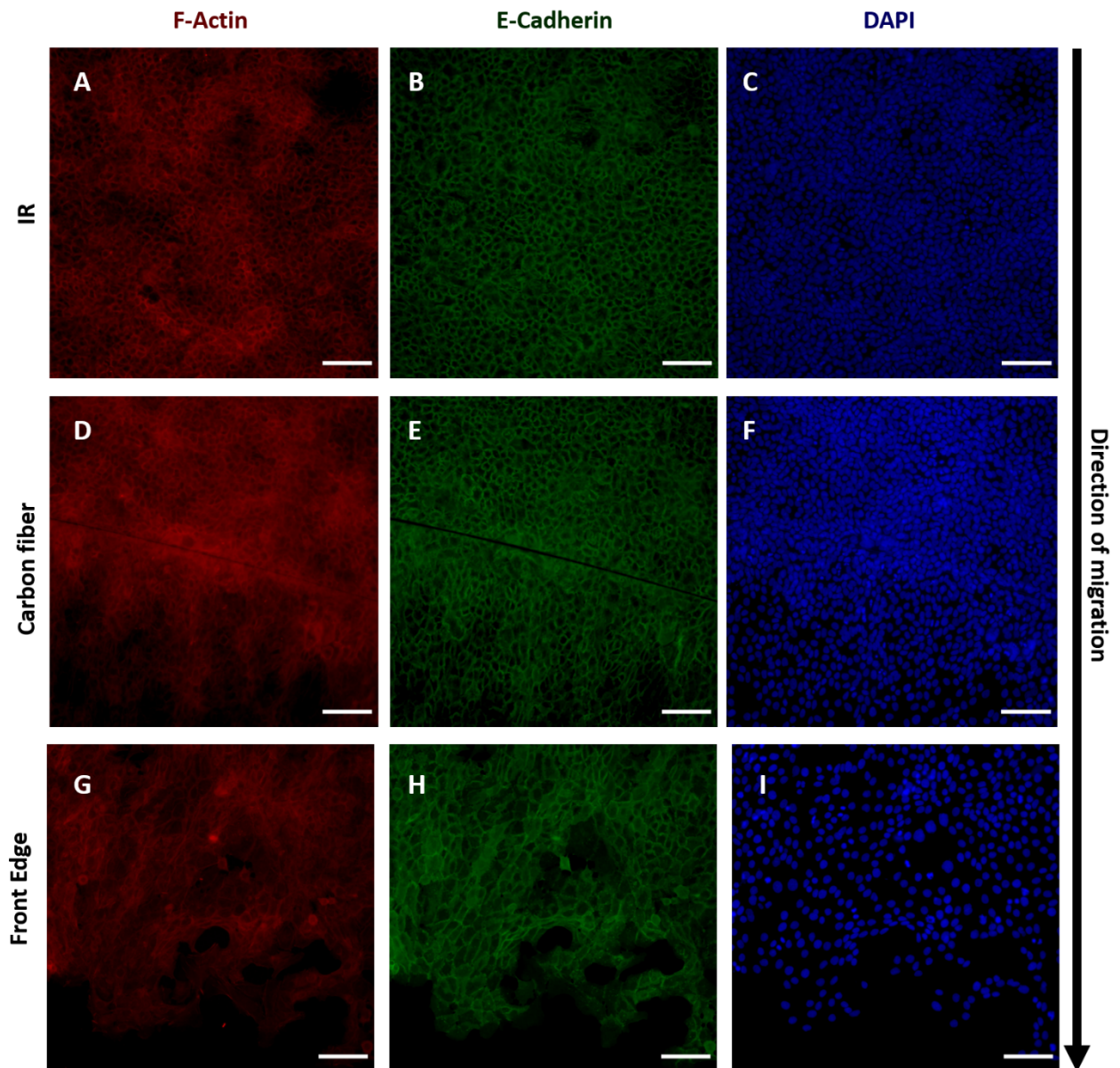


Figure 5.16. Actin cytoskeleton labelling and E-Cadherin immunofluorescence (72h). IR. Cells within the cell monolayer (inner region). Carbon fiber. Cells pushing the carbon fiber. Front Edge. Leading front. From left to right. Actin, E-Cadherin and DAPI staining. Scale bar =100 μ m

Figure 5.16, shows that there exists a gradient in the amount of actin around the fiber, extending upwards at a certain distance from the fiber. This is especially intense at the left side (fixed end), as noted previously (*Figure 5.14. D*). The intensity observed in cells within the monolayer that are still far from the fiber (*Figure 5.16.A*) is uniform. With respect to the E-Cadherin distribution, an overall jammed (solid-like) state is observed throughout the inner region of

the cell culture (*Figure 5.16.B, E*), and, to a lesser extent, in the migratory edge (*Figure 5.16.H*). This could be representative of the so-called unjammed transition (UJT) which refers to the switch from a solid-like state of a non-migratory confluent monolayer (jammed) to a fluid-like state of a migratory confluent monolayer. Both jammed and unjammed phases highly depend on cell-cell adhesion and friction between cells, which is lower at the migratory front and increases towards the bulk of the monolayer^{14,16}. These observations are also consistent with the studies that postulate that intercellular tension is transmitted from the leading edge into the tissue, generating a growing tensile gradient that extends inwards¹².

5.6 Discussion

Collective cell migration is a process highly coordinated by molecular rearrangements driven by active forces generated by cells (traction, cell-cell forces, cell protrusions, cellular confinement) or passive forces opposed by its environment. A better understanding of the regulation of cell adhesions and force generation would help to disentangle important physiological and pathological processes that are governed in part by mechanical forces (such as embryogenesis, tissue repair and homeostasis or cancer invasion)⁹.

The response of a cohesive cell monolayer to the release of physical boundaries, triggers collective cell migration. This is mediated by the anisotropic distribution of E-Cadherin at the free edge of border cells, which promotes ROCK-dependent contractility at the back and integrin-mediated cell-ECM adhesion at the front. Cell-ECM adhesion activates integrin signaling that results in actin polymerization and generation of cell protrusions (lamellipodia). This migratory phenotype is known as **cell polarization**. The tension generated by the contraction of the actin cytoskeleton is transmitted to adherens junctions (AJs), causing a conformational change in α -catenin that allows its binding to vinculin. This results in enhanced F-actin binding and recruitment of actin regulatory proteins that reorganize the cytoskeleton around the cell-cell adhesion (cortical stiffening). Moreover, increasing tension on cadherin-mediated adhesions promotes cadherin clustering at the plasma membrane (*Figure 5.1*)^{5,6,8}.

Consequently, coordinated movement mainly depends on the strength of cell-cell adhesions, which are responsible of cellular mechanocoupling. It has been described that monolayer expansion is characterized by larger traction forces exerted at the leading edge that are transmitted to the follower cells through AJs. Thereby, the transmitted mechanical stress increases towards the center of the monolayer, generating a tensional state for the whole tissue that is weaker at the front and stronger in the bulk of the tissue^{12,15}.

Here, this built-up inward tension, is easily visualized at different regions of a migrating and non-migrating monolayer. First, the front edge of a steady cell culture at time 0 (wound just performed), shows a cytoplasmic distribution of E-Cadherin (*Figure 5.7. D*), meaning that there is no tension transmitted through cadherin junctions of neighboring cells that are passively associated^{11,5}. In this case, there is no need for an extra recruitment of cadherin proteins to the plasma membrane. Furthermore, in cells at the migratory leading front, E-Cadherin is located within the cell periphery. However, a slight internalization is also noticed for both that migrated freely (without fiber) and those that overpassed it (*Figure 5.7. E, F*).

In our case, we expect the monolayer tension to be higher while pushing the fiber. This arises from the following hypothesis: cells adhere to the carbon fiber through integrin adhesions, since it is coated with collagen I. The fiber poses an obstacle with a certain stiffness. As cell adhesions are known to be mechanosensitive, they are capable to react to ECM rigidity¹⁷. Thereby, to overcome this barrier, they should reinforce both actin cytoskeleton and cell-cell adhesions in order to exert greater force on the fiber while keeping tissue integrity.

We observed that E-Cadherin staining appears to be more intense and ubiquitously localized within cells surrounding the fiber (*Figure 5.9.B, D, F*). It would be conceivable to think that this may be due to a higher accumulation of cell-cell adhesions at this point, in response to a tissue stretching produced upon migration over the fiber. Nevertheless, it should be noted that these differences may be due to the fact that these cells are located in a different focal

plane with respect to the cells attached to the plate. In addition, there is an accumulation of cells pushing on the fiber, which probably results in its shrinkage and overlapping, making the scenario difficult to interpret. Taking this into account, we consider that the information obtained from these images, is not sufficient to examine the intracellular distribution patterns observed in cells over the fiber.

On the other hand, the premature stop of the monolayer that is pushing the fiber, could be explained by the increase in the intercellular tension caused by the presence of the fiber. As the cell monolayer expands, intercellular tension increases, and then cell adhesions mature, resulting in an increment of the cell cohesiveness within the monolayer. This causes a decrease in cell velocity due to the increase of intercellular friction¹⁸.

Consequently, it would be reasonable to expect that inner tension of the tissue is higher when the expanding monolayer is migrating against an obstacle, comparing to that which freely migrates. This assumption is in agreement with the observed experimental results and the theoretical model proposed in *chapter 4*. Along the tissue affected by the fiber (L_c), there is a balance between inertia and friction presented by cells. The resistance exerted by the fiber in addition to the accumulation of cells, makes the cells that are pushing in the first row to decelerate over time. This stress is transmitted to the follower cells, triggering the reinforcement of cell-cell adhesions which results in an increase in friction between cells and, eventually, in the halt of migration.

To confirm this, we evaluated the differences in the bulk of the monolayer (IR, inner region) of respective steady cell culture (time 0), the inner tissue far from the fiber (IR-Far F) and a region of the monolayer located immediately upstream the fiber. The non-migrating cells present a diffuse cytoplasmic distribution of E-Cadherin in the center of the monolayer (*Figure 5.6. C-1*), while the migrating cells show a cortical localization regardless of its proximity to the fiber (*Figure 5.6. D-2 and Figure 5.9. A, C*).

A recent study has proven that different isoforms of the Cadherin family are involved in the maintenance of tissue homeostasis. They demonstrate the

reciprocal collaboration between E-Cadherin and P-Cadherin in the regulation of intercellular tension. Magnetocytometry experiments revealed that both P-Cadherin and E-Cadherin play different roles as tension regulators, being responsible of the magnitude of the intercellular tension and regulation of its build-up rate respectively¹¹.

Therefore, the localization of E-cadherin at cell-cell adhesions by itself is not sufficient to determine an increased intercellular stress in the presence of the fiber. It should be assessed together with other collaborating molecules (such as P-Cadherin, integrins, myosin II or α -actinin) and constituents of different cell adhesion complexes (FAs, AJs, desmosomes, tight junctions). Also, it should be studied concomitantly with other techniques, as quantitative analysis of gene and protein expression, to achieve a more solid and accurate characterization of the system.

Also, we correlated the observations obtained from E-Cadherin detection with the associated **cytoskeletal reorganization**. During cell migration, actin cytoskeleton organizes in brunches at cell front that constitute cell protrusions and form contractile stress fibers at the ventral zone and at the trailing edge.

To assess how the cytoskeleton is reorganized during our force measurement experiments, we analyze the initial steady state of HaCat cells (Time 0) which present a cortical organization of actin in the confined cells of the inner region of the monolayer (*Figure 5.10. D*), as described for confluent cell cultures¹², and more diffuse distribution in border cells (*Figure 5.12. A, D, G*). When migration is triggered, the formation of actin bundles and stronger cortical reinforcement within the tissue can be visualized, in response to an increased monolayer stress transmitted by the leader cells at the front edge, generating an actin gradient that is higher close to the fiber and decays progressively as it enters the monolayer (*Figure 5.10. E, F*),

Force transmission between neighboring cells, make cells located several rows upwards the fiber to start actin polymerization in order to migrate and overpass the forthcoming obstacle. This is visualized as an actin gradient extending a certain distance upwards the carbon fiber (*Figure 5.16. D, G*). that

progressively decreases towards the bulk of the monolayer, where the overall state of actin is uniform (*Figure 5.16. A*). For a more in-depth visualization of the inward actin structure, a zoom is shown on a non-migratory monolayer, which presents the aforementioned cortical distribution of F-actin (*Figure 5.11. D-1*), versus a migrating monolayer with a carbon fiber (*Figure 5.11. E-2, E-3*). The region which is located far from the fiber presents the formation of some actin bundles that denotes that the monolayer is migrating (*Figure 5.11. E-2*). In turn, the region located immediately upstream the fiber, exhibits a clear increase in the density of actin-filaments throughout the cell (*Figure 5.11. F-3*).

Leader cells in turn extend actin-rich lamellipodia to the free-space (*Figure 5.12. E, F*). Interestingly, lamellipodial actin network at the front edge, show different directionalities. In cells that moved against the fiber, actin filaments are arranged parallel to the fiber (*Figure 5.13.F-2*). In contrast, actin protrusion filaments points to the direction of migration (perpendicular to the fiber) in cells that migrated freely (*Figure 5.13.E-1*). This could confirm the model proposed by Ofek et al.¹⁹. They study the differential roles of cytoskeleton elements (actin, intermediate filaments and microtubules) in cellular stiffness and compressibility. By measuring compressive modulus and apparent Poisson's ratio of single cells under compression, they conclude that the three cytoskeletal elements jointly contribute to the resistance of the cell to external constraints, being intermediate filaments and microtubules major contributors in maintaining cell shape, and actin cytoskeleton in keeping bulk compressive stiffness. Thereby, under single cell compression, actin filaments localize at cell periphery to provide the cytoplasm with stiffness and form a dense actin network throughout the cell. When compression is released, actin filaments exert tensile forces on cell sides while microtubules push towards the former compression axis to recover the cell shape. Since our cells have been subjected to a compression exerted by the fiber, it is reasonable to think that after compression release, actin filaments reorganize in a different arrangement and direction. In this sense, it would be interesting to study the role and time evolution of different cytoskeletal components in cell recovery under different

conditions, such as different timepoints and fiber lengths, in presence of inhibitors or by influencing the expression of the main cytoskeletal proteins.

Furthermore, when the surrounding region of the fiber is analyzed, actin staining shows that there is a clear reinforcement of the cytoskeleton in places where the cells need to exert a greater force (*Figure 5.14*). As expected, F-actin bundling is enhanced close to the fixed end (*Figure 5.15.D1*) and resembles the cytoskeletal organization acquired by lamellipodial protrusions formed at the leading cells (*Figure 5.13. E-1*). This is less pronounced in regions more distant from the fixed end, which show a dense actin network throughout the cell, with no remarkable structural differences between the middle and tip region of the fiber (*Figure 5.15.E-2, F-3*). These regions exhibit a F-actin organization similar to those found in the region immediately upwards the fiber (*Figure 5.11. F-3*), due to the high rigidity of the region. Nonetheless, it appears that there is a slight increase in the density of actin filaments in the middle position (region 2) with respect to the fiber tip (region 3), being the cell density similar in both cases.

This could be explained in accordance to several studies about the interplay between the rheological properties of the cytoskeleton and substrate rigidity^{4,20}. They describe the cytoskeleton as an active gel, whose internal mechanical properties (viscosity and elasticity) adapt to the matrix stiffness sensed through focal adhesions (FAs). Together, these three elements influence on the ability of cells to polarize. Thereby, cells need to stiffen when interacting with stiffer substrates and vice versa. This cell stiffening can be visualized as an alignment of F-actin along the same axis, which changes the elastic modulus of the actin network due to its anisotropy. This promotes the localization of traction forces in a specific area which, in turn, strengthen the FAs and promote polarization. Consistent with this, cells pushing the fiber present strong F-actin polarized fibers due to an increase in the environmental stiffness.

Gathering all observations, it can be assumed that at the center of the monolayer, cells do not fully respond to the external stimuli. Recalling the terms defined in the theoretical model and the biological behavior of the system (*chapter 4*) the bulk of the monolayer that is far away from the fiber (IR Far-F),

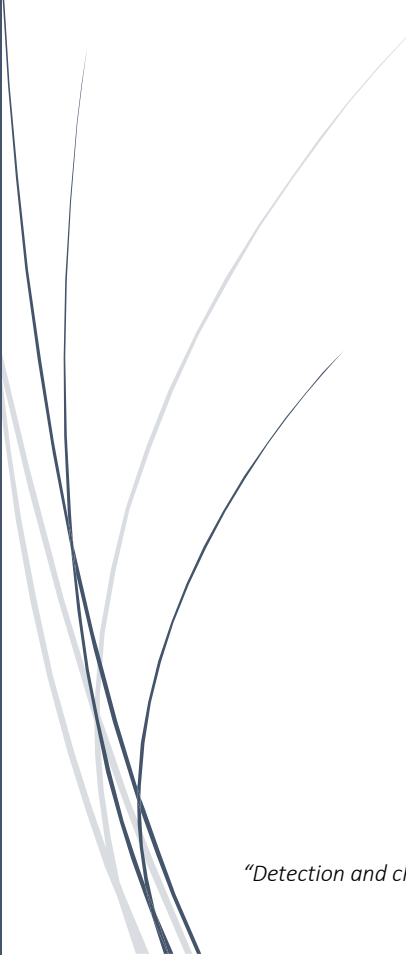

would correspond to the region where we imposed the far field boundary condition, located at a distance " ℓ " from the fiber. At this boundary, the velocities of cells are considered uniform in space. Here cells barely move, so differences in velocities between neighboring cells are negligible. The region immediately upstream the fiber where a gradient of actin is observed (IR-F), could be identified as the length of tissue affected by the fiber, L_c , and should correspond with an increase in the tensional state. Cell-ECM adhesions are strengthened by recruiting molecules that reinforce the cell attachment to the substrate and connection of FAs to the actin retrograde flow, thus promoting cell protrusions¹. In turn, the cytoskeletal tension transmitted through cadherins results in cell-cell adhesion reinforcement by the recruitment of actin binding proteins that stabilize the link between the cytoskeleton and actin protein regulators. This activates actin bundling and cortical stiffness around the cell-cell junction⁶. Consistent to this, cortical stiffening and cytoskeletal F-actin alignment seem to be enhanced at the fixed end (region 1) of the carbon fiber, where cells need to exert a stronger force in response to a stiffer environment, and decreases progressively towards the tip of the fiber.

In conclusion, the presence of the fiber has a clear effect on actin-cytoskeleton reinforcement in response to an increase in environmental rigidity, generating an inward gradient, as previously reported^{4,12}. However, E-Cadherin shows a similar distribution pattern in every region of the migratory layer (downstream, around and upstream the fiber) (*Figure 5.16. B, E, H*). As we already discussed above and in accordance with other studies^{9, 11}, E-Cadherin staining alone, reveal an overall jammed state of the migrating monolayer, but does not provide enough information about the reinforcement of cell-cell adhesions at different regions.

For a deeper understanding, it would be necessary the study of different cytoskeletal elements together with other molecules involved in different adhesion complexes. The study of their mechanical behavior and subcellular localization will contribute to a broader knowledge of the relationship between mechanics and signaling pathways.

1. Meacci, G. *et al.* α -Actinin links extracellular matrix rigidity-sensing contractile units with periodic cell-edge retractions. *Mol. Biol. Cell* **27**, 3471–3479 (2016).
2. Ram, S., Vedula, K., Ravasio, A., Lim, C. T. & Ladoux, B. Collective Cell Migration: A Mechanistic Perspective. *Physiology* 370–379 (2013). doi:10.1152/physiol.00033.2013
3. Giannone, G., Mège, R.-M. & Thoumine, O. Multi-level molecular clutches in motile cell processes. *Trends Cell Biol.* **19**, 475–486 (2009).
4. Doss, B. L. *et al.* Cell response to substrate rigidity is regulated by active and passive cytoskeletal stress. *Proc. Natl. Acad. Sci. U. S. A.* **117**, 12817–12825 (2020).
5. Mège, R. M. & Ishiyama, N. Integration of cadherin adhesion and cytoskeleton at adherens junctions. *Cold Spring Harb. Perspect. Biol.* **9**, 1–18 (2017).
6. Khalil, A. A. & de Rooij, J. Cadherin mechanotransduction in leader-follower cell specification during collective migration. *Exp. Cell Res.* **376**, 86–91 (2019).
7. Budnar, S. & Yap, A. S. A mechanobiological perspective on cadherins and the actin-myosin cytoskeleton. *F1000Prime Rep.* **5**, (2013).
8. Mayor, R. & Etienne-manneville, S. The front and rear of collective cell migration. *Nat. Publ. Gr.* (2016). doi:10.1038/nrm.2015.14
9. Chen, T., Saw, T. B., Mege, R. M. & Ladoux, B. Mechanical forces in cell monolayers. *J. Cell Sci.* **131**, (2018).
10. Paredes, J. *et al.* Epithelial E- and P-cadherins: Role and clinical significance in cancer. *Biochimica et Biophysica Acta - Reviews on Cancer* **1826**, 297–311 (2012).
11. Bazellères, E. *et al.* Control of cell-cell forces and collective cell dynamics by the intercellular adhesome. *Nat. Cell Biol.* **17**, 409–420 (2015).

12. Serra-picamal, X. *et al.* Mechanical waves during tissue expansion. *Nat. Phys.* **8**, (2012).
13. Thermo Fisher Scientific. Phalloidin Conjugates For Staining Actin. Available at: <https://www.thermofisher.com>.
14. DeCamp, S. *et al.* Epithelial layer unjamming shifts energy metabolism toward glycolysis. *Sci. Rep.* 1–15 (2020). doi:10.1101/2020.06.30.180000
15. du Roure, O. *et al.* Force mapping in epithelial cell migration. *Proc. Natl. Acad. Sci.* **102**, 2390–2395 (2005).
16. Garcia, S. *et al.* Physics of active jamming during collective cellular motion in a monolayer. *Proc. Natl. Acad. Sci. U. S. A.* **112**, 15314–15319 (2015).
17. Hoffman, B. D., Grashoff, C. & Schwartz, M. A. Dynamic molecular processes mediate cellular mechanotransduction. *Nature* **475**, 316–323 (2011).
18. Deforet, M. *et al.* Automated velocity mapping of migrating cell populations (AVeMap). *Nath methods* **9**, 1081–108 (2012).
19. Ofek, G., Wiltz, D. C. & Athanasiou, K. A. Contribution of the Cytoskeleton to the Compressive Properties and Recovery Behavior of Single Cells. *Biophysj* **97**, 1873–1882 (2009).
20. Étienne, J. *et al.* Cells as liquid motors: Mechanosensitivity emerges from collective dynamics of actomyosin cortex. *Proc. Natl. Acad. Sci. U. S. A.* **112**, 2740–2745 (2015).



6 Generation of kindlin-1 deficient cellular model for force measurement experiments

*“Look up at the stars and not down at your feet.
Try to make sense of what you see,
and wonder about what makes the universe exist.
Be curious”
(Stephen Hawking)*

*“Detection and characterization of mechanical forces and dynamic molecular rearrangements in collective
cell migration” – Verónica López*

6.1 Kindler syndrome

Kindler syndrome (KS), also called “congenital bullous poikiloderma”, is a hereditary autosomal recessive skin disorder. It is a type of *epidermolysis bullosa* (EB) caused by a mutation in the *FERMT1* gene (Fermitin family member 1), which encodes **kindlin- 1 protein**. Most of reported mutations that cause KS often result in the production of nonfunctional protein or the total loss of kindlin-1.

Kindlin- 1 is one of the multiple components that constitute **focal adhesions (FAs)**, which are protein complexes that connect the actin cytoskeleton to the extracellular matrix. Kindlin-1 is responsible for **integrin activation, regulation of migration, proliferation and adhesion**. At the tissue level, it predominates in epithelial basal cells and is localized at the dermal-epidermal junction zone.

Its loss, caused by *FERMT1* mutation, leads to the complex clinical manifestations typical of Kindler syndrome, characterized by skin blistering, skin atrophy, photosensitivity, poikiloderma and mucosal manifestations.

Regarding **histological features**, KS may result in **multiple cleavage sites** (intraepidermal, junctional or dermal) at the same time, including the **mucous membranes**. This differs from other forms of EB in which blistering occurs in a particular skin layer.

KS presents loss of *rete ridges*, hyperkeratosis, atrophy, cleavage of basal membrane, and reduplication of *lamina densa*. Laminin- 332 and collagen IV and VII (ECM proteins secreted by keratinocytes) show an abnormal branched staining pattern when analyzed by immunofluorescence^{1,2,3}.

In vitro **KS keratinocytes** are typically smaller than the healthy ones and present **abnormal shape**, with protrusions that expand in different directions. Some studies argue that KS cells motion is **slow and random** compared to normal keratinocytes resulting in **delayed wound closure**^{4,5}. However, other groups have demonstrated that kindlin-1 deficient cells reach **higher velocities** due to deficient integrin-mediated cell-substrate adhesions^{6,7}.

Furthermore it has been demonstrated that loss of kindlin-1 also results in a lower proliferation rate and lower efficiency in colony formation^{3,4,6}.

6.1.1 Kindlin-1 protein structure

The mammalian kindlin family of proteins consists of three isoforms, namely kindlin-1, kindlin-2 and kindlin-3, which express in a tissue-specific manner. Kindlin-1 is mostly expressed in epidermis, and less frequently found in colon, kidney and stomach. Kindlin-1 defect results in Kindler syndrome genodermatosis. Kindlin-2 is expressed in embryonic stem cells and ubiquitously distributed in tissues being more concentrated in myocytes. Kindlin-3 expression is restricted to hematopoietic cells. Loss of kindlin-2 and kindlin-3 results in embryonic lethality and bleeding disorders respectively^{8,9}.

Kindlin-1 protein is a 677 amino acid protein encoded by *FERMT1* gene. It is a component of FAs and plays a regulatory role in migration, proliferation and adhesion. Kindlin-1 binds to β -1, β -3 and β -6 integrin subunits causing its activation.

Kindlin-1 presents a **FERM-like domain** (erzin, raxidin, moesin) consisting of three subdomains: F1, F2 and F3. Unlike most FERMT domains, kindlin family also exhibits an N-terminal F0 subdomain preceding the F1 subdomain and a **Plekstrin Homology (PH)** domain, which is inserted in the F2 subdomain¹⁰. This PH domain allows its binding to phosphoinositides (such as PIP3 and PIP2) and helps to target kindlins to membranes, which contributes to their localization at FAs. Additionally, kindlin-1 presents an **ILK** site (integrin-linked kinase) that it is thought to reinforce its localization at FAs.

Furthermore, F3 domain, contains a **PTB** domain (phosphotyrosine binding domain), which enables its binding to the NPxY motifs in β -integrin subunit. (N = asparagine amino acid; P= proline amino acid; x= any amino acid; Y = tyrosine amino acid) (*Figure 6.1*)¹¹.

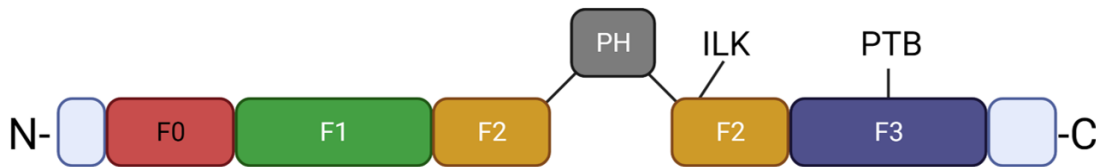


Figure 6.1. Kindlin-1 protein domains. This is a self-created illustration, using www.Biorender.com

FERM-like domain, containing PTB-fold, is also present in **talín** structure. This supports the fact that **talín** and **kindlin** bind to proximal and distal tyrosines of **β -integrin cytoplasmic tail** respectively. Both contribute to an integrin conformational change from an inactive (bent-closed (BC) or extended-close (EC)) to a high-affinity **active state** (extended-open (EO)), which allows **ligand-binding** at the integrin head domains and triggers protein recruitment for FA assembly.

Contrary to talin, no actin binding site (ABS) has been reported for kindlin-1, so it binds to the cytoskeleton through its linking to **migfilin** protein and/ or the ILK-PINCH-parvin (IPP) complex^{11,12} (Figure 6.2).

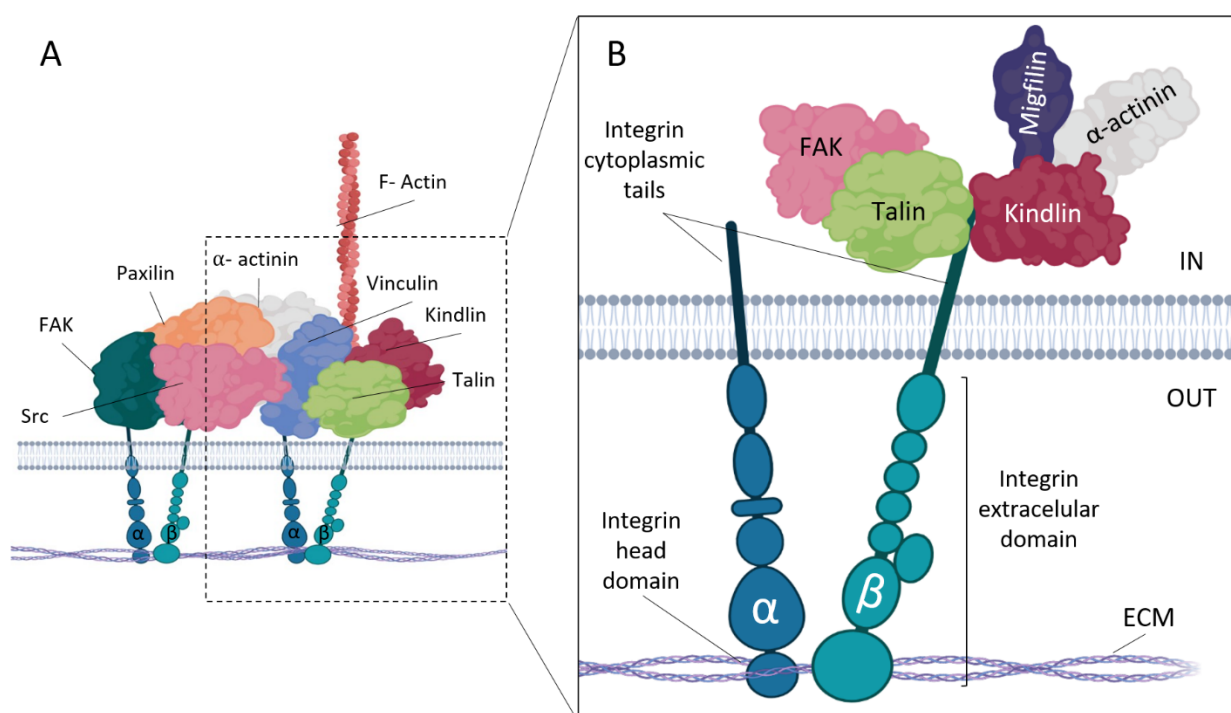


Figure 6.2. A. General representation of some of the molecules involved in the Focal Adhesion (FA) complex. B. Talin and Kindlin binding to β -1 integrin cytoplasmic tail and adaptor proteins recruitment. This is a self-created illustration, using www.Biorender.com

6.1.2 Relevance of kindlin in mechanotransduction and wound healing

As mentioned above, **integrins** are broadly expressed heterodimeric **adhesion molecules** that connect ECM components to the intracellular cytoskeleton. They are constituted by two subunits: **α and β** . This α/β association defines the **affinity state** for its ligands, depending on the conformation that they adopt. At this point, both **talin and kindlin** play a key role in **integrin activation** and subsequent **FA complex formation**.

FAs are **mechanosensitive** structures formed by a complex association of proteins, also called "**molecular clutches**" (*see chapter 2 general introduction*) The molecular clutch acts as a **mechanical link** for bi-directional communication, that transmits forces from the cytoskeleton to the ECM and vice versa, also modulating its response in accordance with its environmental stiffness¹³. This triggers a series of biochemical signals that affect **cell adhesion, cytoskeleton dynamics, cell proliferation and differentiation** through modulation of gene expression^{7,13,14,15,16}.

Little is known about which is the specific role of kindlin in the mechanosensitive regulation of integrins¹⁴. However, crystallography studies of kindlin-integrin interactions have revealed that, besides its amino acid sequence similarities with talin, kindlins present a different overall structure. This provides them with exclusive integrin recognition sites, which allow **dimerization of kindlins**¹⁷. Moreover, a recent study has demonstrated that kindlin-2 dimers are capable of **bearing and transmitting forces** applied to integrins. They also promote cluster formation by binding two β -integrins through the kindlin dimer, which allows them to transmit forces from one integrin complex to the other producing an intracellular **cross talk**¹⁰.

In addition to the regulation exerted through FA, kindlin-1 has recently been shown to bind to EGFR (Epidermal growth-factor receptor) preventing its lysosomal degradation. This was confirmed by studies performed in skin and isolated keratinocytes from patients with KS, who present loss of kindlin- 1 and reduced levels of EGFR , resulting in impaired EGF signaling and defective migratory behavior^{18,19}.

In summary, the integrity of FAs is required for processes as **mechanosensing, cell polarity, cell migration and proliferation**, which are drastically affected in cells lacking kindlin-1.

6.2 Motivation and methodology

Loss-of-function mutations in *FERMT-1* produces Kindler Syndrome⁷. Since this is a rare disease, the availability of patient samples is very limited. For this reason, we generated a cellular model using CRISPR/cas9 gene editing system to target the deletion of a specific region of the gene which results in loss of kindlin-1 expression and reproduce the Kindler syndrome phenotype in previously HKE6E7 immortalized keratinocytes.

As mentioned above, KS keratinocytes present abnormal shape and migration patterns. Furthermore, due to its implication in FA formation and the important role that they play in mechanosensing and wound re-epithelization, the poor substrate adhesion underlying KS phenotype is expected to correlate with changes in cell dynamics and kinematics. This fact leads us to test kindlin-1 deficient cells under our experimental conditions. Thus, we could analyze how kindlin-1 deficiency affect force generation and explore the response of the 2D force sensor developed in [chapter 4](#) in cells exhibiting different phenotypes.

6.2.1 CRISPR/Cas9 gene editing system

CRISPR/Cas9 gene editing system (clustered regularly interspaced short palindromic repeats) consists of the following components ([Figure 6.3](#)):

- **Recombinant Cas9 endonuclease:** it is an enzyme from *Streptococcus pyogenes* containing two active sites to generate double-stranded breaks (DSBs) in DNA.
- **Guide RNA (gRNA):** In its natural form, gRNA consists of two RNA segments: a target recognition sequence CRISPR RNA (crRNA) and transactivator CRISPR RNA (tracrRNA, required for the formation of the complex crRNA-Cas9). It contains the specific sequence of the target DNA and together with the Cas9 endonuclease form a

ribonucleoprotein complex (RNP) to guide the targeted cleavage of genomic DNA.

- **Protospacer Adjacent Motif (PAM):** It refers to short sequences adjacent to the region of DNA to be cut, and they are located in the DNA strand complementary to the target. These sequences are different depending on the species that Cas9 come from. For Cas9 from *S. pyogenes* this sequence is defined as 5'-NGG-3', where N corresponds to any nucleotide.

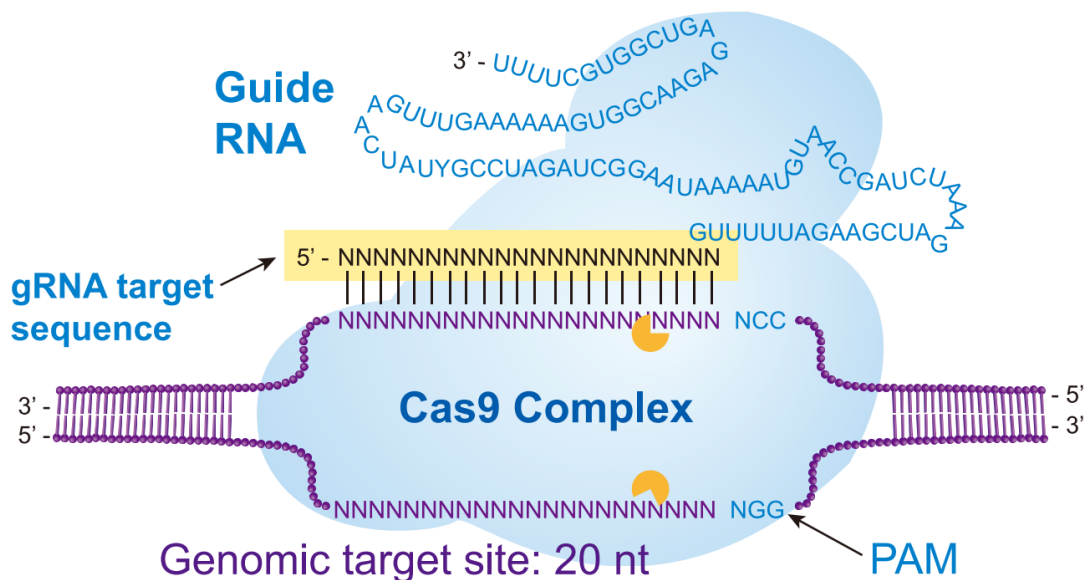


Figure 6.3. CRISPR/Cas9 System. CRISPR / Cas9 system comprises a gRNA and a Cas9 nuclease (blue), which together form an RNP complex. The cleavage site is specified by the gRNA (sequence marked in yellow), which recognizes 19 or 20 nucleotides on the opposite strand of the PAM site, allowing Cas9 to make a DSB (orange) located between nucleotide 3 and 4 from the PAM site 3' of the gRNA. (From *GeneScript CRISPR handbook 2016*).

6.3 Materials and Methods

6.3.1 Immortalized human keratinocytes (HKE6E7)

Primary human keratinocytes were previously immortalized in our laboratory using the retroviral vector pLXSN16E6E7, containing an expression cassette for the E6 and E7 proteins derived from human papillomavirus HPV16, (*Addgene (Watertown, MA, USA)*), together with plasmids containing necessary sequences for viral encapsidation (pNG-VL3-MLVgag-pol, pNGVL3-4070; *Addgene*). This is frequently used for cell immortalization procedures due to their specific activities on p53 and pRb (tumor suppressor genes) for degradation²⁰.

Cells were culture for several passages until no feeder layer was necessary for their survival. The expression of the HPV E6 / E7 antigen was confirmed by Western Blot analysis of the total protein extracted from transfected cells. Also, it was confirmed that there is no tumorigenic effect in NMRI- Foxn1^{nu/nu} mice (checked for 3 months)²¹.

6.3.2 CRISPR/cas9 system and nucleofection

We generated *FERMT1*-knockout keratinocytes using CRISPR/cas9 gene editing system to delete a specific region of the gene. This is expected to reproduce the Kindler syndrome phenotype in previously HKE6E7 immortalized keratinocytes.

CRISPR guides (*Table 6.1, Figure 6.4*) were designed to target **exon 6 of *FERMT1* gene**, using a bioinformatic tool²².

Target site	Target sequence gRNA (5'-3')
Exon 6 from FERM1 gene	Guide 1: GATATATATGTAAAATTGAC Guide 2: GATCGCCTGTTTAGCCCTGC

Table 6.1. gRNAs designed to target exon 6 from FERMT1.

Synthetic gRNAs and recombinant Cas9 (*Alt-R HiFi*) were purchased from *Integrated DNA technologies (IDT (Coralville, IA, USA))*. RNP complexes were reconstituted following the manufacturer's recommendations and introduced into keratinocytes by nucleofection, using *Neon transfection system (Thermo Fisher Scientific)* for this purpose.

For nucleofection process, 1.5×10^5 HKE6E7 keratinocytes were resuspended in 10 μ l of Buffer R (Thermo Fisher Scientific) for each reaction and RNP complexes were added to each sample (72.7 pmol of crRNA: transRNA and 10.9 pmol of Cas9, 6.6: 1 molar ratio). Electroporation conditions were: 1 pulse / 1700 V / 20 ms.



Figure 6.4. Scheme of CRISPR/Cas9 complex. Green sequence/green arrow. Corresponds to guide 1. Pink sequence/pink arrow. Corresponds to guide 2. Green asterisk. Cleavage site for guide 1. Pink asterisk. Cleavage site for guide 2. PAM. PAM sequence adjacent to each target sequence.

6.3.3 Isolation of edited clones

After electroporation, cells were plated in 6-well plates (*Corning (NY, USA)*) in absence of feeder layer with keratinocyte growth medium (KGM). KGM consists of a 2: 1 ratio mixture of DMEM: HAM'S F12 (Nutrient mixture HAM, Gibco), supplemented with 10% FetalClone II bovine serum (HyClone, Thermo Fisher Scientific) and 1% penicillin/streptomycin, also containing choleric toxin (8 ng/ml, Sigma-Aldrich), insulin (5 μ g/ml, Sigma-Aldrich), adenine (2.4 ng/ml,

Sigma-Aldrich), hydrocortisone (0.4 µg/ml, Sigma-Aldrich) and tyrosine-triiodine (1.3 ng/ml, Sigma-Aldrich) and epidermal growth factor (EGF), 10 ng/ml, Sigma-Aldrich).

To obtain isolated clones, keratinocytes were trypsinized at 37 ° C for 20 minutes (Trypsin 1-300 0.25% - EDTA (Ethylene-Diamino-Tetra-Acetate) 0.02%, *Sigma-Aldrich (Saint Louis, MO, USA)*), and plated without feeder layer in 100 mm diameter plates (*Corning*) at 10^3 cell density per plate, in KGM supplemented with ROCK Y-27632 inhibitor (10 µM) in order to avoid cellular differentiation and promote cell proliferation^{23,24}.

After 7 days of culture, individual clones were isolated using polystyrene cloning cylinders (*Sigma Aldrich*) and expanded for further analysis.

6.3.4 Nucleic acid extraction

To extract **genomic DNA**, 2×10^6 keratinocytes were used. Cells were washed with 1x PBS, trypsinized, and centrifuged at 233g. Cell pellet was resuspended in 700 µl of lysis buffer (20mM Tris HCl, pH 8; 5mM EDTA, pH 8; 400mM NaCl, and 1% SDS), 10 µl of proteinase K (20 µg / µl, *Roche (Basel, Switzerland)*) was added, and then it was incubated overnight (O/N) at 55 ° C with shaking. After adding 4 µl of RNase (5 µg / µl, *Roche*), a 30 min incubation was carried out at 37 ° C. The gDNA was precipitated by centrifugation at 9,200g in isopropanol (1:1 ratio, *Scharlau (Barcelona, Spain)*) and washed in 70% ethanol (*Scharlau*) followed by centrifugation at 9,200g to remove residual salts. The gDNA pellet was resuspended in TE 1x buffer (10mM Tris-HCl, 1mM EDTA, pH 7.5) and stored at 4 ° C.

Total **RNA** was isolated from approximately 3×10^6 cells. Cells were washed with 1x PBS, trypsinized, and centrifuged at 233g. Cell pellet was resuspended in 700 µl of Quiazol Lysis Reagent (*Qiagen*). RNA was purified using the *miRNeasy kit (Qiagen)* based on silica membrane technology, and finally stored at -80 ° C.

The concentration and quality of the extracted nucleic acids was determined by spectrophotometry using an *ND-1000 kit (NanoDrop)*.

6.3.5 RNA reverse transcription (cDNA obtention)

Complementary DNA (cDNA) was obtained from 5 µg of total RNA by reverse transcription PCR (RT-PCR), following the instructions specified in the *SuperScript III First-Strand Synthesis System for RT-PCR kit (Invitrogen (Carlsbad, CA, EE.UU.))*. The resulting cDNA was stored at -20 °C for subsequent PCR analysis (*see reagents and reaction conditions on Table 6.4 and Table 6.5 below*).

Primers for RT- PCR	Localization	Tm	Amplicon Size
F: CCTTGTTAAAGCCGTCTGGTGA	Exon 4	63.57°C	~600 bp
R: CGCCTGCAAAATCCTGTGTT	Exon 8	63.40°C	

Table 6.2. Primers for RT- PCR. F. Forward. R. Reverse.

Primers for RT-PCR were designed as shown on [Table 6.2](#). RT-PCR primers were tested under different MgCl₂ concentrations (10mM, 15mM and 20mM) and melting temperatures (60°C and 63°C). [MgCl₂] = 15mM and T_m = 63°C were selected as the best conditions for these primers.

6.3.6 DNA fragment amplification

Amplification of DNA fragments was performed using the **polymerase chain reaction (PCR)** technique.

Design of primers was carried out manually with the assistance of *Primer 3 web tool* which allows selecting the ideal primers with optimal characteristics of percentage of guanines and cytosines (GC), melting temperature (Temperature melting (T_m)), size of both primer and amplification product, and number of complementary bases.

Primers for PCR	Localization	Tm	Amplicon Size
F: GAGCCTCAGGTCAGTGCTC	Intron 5-6	62.9°C	~500 bp
R: GCACAGTAAGCTGCTACCAA	Intron 6-7	60.7°C	

Table 6.3. Primers for PCR. F. Forward. R. Reverse.

Primer pairs were synthesized to target the gene regions of interest (*FERMT1*, exon 6) (Table 6.3), and were tested under different MgCl₂ concentrations (10mM, 15mM and 20mM) and melting temperatures (60°C and 63°C). [MgCl₂] = 20mM and Tm= 60°C were selected as the best conditions for these primers.

	Concentration	Volume
gDNA /cDNA	40 ng/μl / 125 ng/μl	1,5 μl
Buffer	10x	1,5 μl
MgCl ₂	20 mM/ 15mM	1,5 μl
dNTPs	1,25 mM	2 μl
Primers	10μM	1 μl (R) + 1 μl (F)
Taq Fast Start	5 u/μl	0,15 μl
H ₂ O milliQ	-	6,35 μl

Table 6.4. PCR reagents. gDNA. Genomic DNA. cDNA. Complementary DNA. MgCl₂. Magnesium chlorhite. dNTPs. Deoxynucleotides triphosphate. Taq Fast Start. Taq DNA polymerase enzyme.

Concentrations and volumes of the reagents used for PCR (*Roche*) reaction are shown in Table 6.4. All PCR reactions were performed in a final volume of 15 μl.

For the amplification of DNA fragments, specific programs were designed using the *Veriti 96-Well Thermal Cycler kit (Thermo Fisher Scientific)* for each pair of primers, the general structure of which is as follows (*Table 6.5*):

Time	Temperature	Cycles
5 min	94°C	
30 s	94°C	
30 s	X + 5°C	x 5 cycles
45 s	72°C	
30 s	94°C	
30 s	X°C	x30 Cycles for
45 s	72°C	gDNA
7 min	72°C	or
		x25 Cycles for cDNA

Table 6.5. General conditions for PCR amplification program. X= specific T_m for each primer (See primers described in table 3 and table 2).

After amplification, 5 µl aliquot of the reaction product was resolved in 1.5% agarose gels (*D-1 low EEO agarose, Conda (Madrid, Spain)*) in tris base buffer, boric acid and EDTA (Tris-Borate-EDTA (TBE)) with 0.005% ethidium bromide, for examination using a transilluminator (*Gel Doc XR +, Bio-Rad (Hercules, CA, USA)*).

6.3.7 Cloning of PCR products

Both genomic DNA and cDNA PCR products were cloned into pGEM®-T Easy Vector (*PROMEGA*) following the instructions for ligation and subsequent bacterial transformation provided by PROMEGA before further Sanger sequencing and analysis of separated alleles.

6.3.8 Sequencing analysis

The PCR-amplified gene fragments were analyzed by automatic sequencing at the Sanger Sequencing Service of the Genomics Unit (*Fundación Parque Científico de Madrid, UCM*), using the ABI PRISM 3730 DNA Analyzer

(Applied Biosystems (Foster City, CA, USA)). Sequence analysis was performed using the program *Serial Cloner*.

6.3.9 Cellular protein extraction

Approximately 2×10^6 cells were used for the extraction of total protein. Cells were washed with 1X PBS twice, and then were disrupted using **lysis buffer** (150mM NaCl, 50mM Tris-HCl, 5mM EDTA and Nonident P-40 Substitute 1% (Roche)) supplemented with a cocktail of **protease inhibitors** (*Complete Mini Protease Inhibitor Cocktail, Roche*) and **phosphatases** (*PhosSTOP, Roche*). Cell lysate was then placed on ice for 15 minutes and subsequently centrifuged for 10 minutes at 16,100g and 4° C. The resulting supernatant, which contains the protein, was stored at -80°C in aliquots to avoid repeated freeze-thaw cycles.

Protein concentration was determined by **bradford colorimetric test** (*Bio-Rad*), measuring the absorbance at 595nm. The protein concentration in each sample was calculated by interpolation using a standard bovine serum albumin calibration curve (range 1-25 µg/µl) (*BSA, Sigma-Aldrich*).

6.3.10 Analysis of protein expression by western blotting

Total protein (20 µg/lane) was denatured by the addition of 4X NuPAGE Buffer 10X and NuPAGE reducing agent for its stabilization after denaturing process (both reagents are used at a final concentration of 1X). Then, samples are heated to 70°C for 10 minutes and placed on ice.

After that, denatured samples were resolved on acrylamide gels with a 4-12% NuPAGE Bis-Tris gradient (*Invitrogen*). In all cases, a molecular weight marker (3-198 kDa) (*SeeBlue, Invitrogen*) and a constant voltage of 120 V was used. Subsequently, transfer to a nitrocellulose membrane (0.2 µm pore size, *Invitrogen*) was performed in a humid chamber with transfer medium (33 mM Tris-Base, 194 mM Glycine and 20% Methanol) at a constant amperage of 0.40 A for 1 hour and 15 minutes.

For blocking of non-specific binding sites, the membrane was incubated in a 5% skimmed milk solution in TBS-0.5% Tween20 (20mM Tris-HCl, 137mM

NaCl, pH 7.6) for 1 hour at room temperature. Subsequently, the membrane was incubated with the corresponding primary antibody (*Table 6.1*) diluted in a 0.5% solution of skimmed milk in TBS-0.5% Tween20.

Primary Ab	Clon/Origin	Reference	Dilution
Anti- Kindlin	Rabbit	Ab68041 (Abcam)	1:1000
Anti-GAPDH	Mouse	sc-365062 (Santa Cruz)	1:5000

Table 6.6. Primary Antibodies for WB.

To detect binding of the primary antibody, corresponding specie-specific secondary antibodies conjugated with horseradish peroxidase (HRP) were used (*Table 6.7*). As loading control, an antibody against GAPDH was used. Finally, a luminescence detection kit (*Clarity Western ECL Blotting Substrate, Bio-Rad*), as a substrate of peroxidase, was used to visualize the results, following the instructions of the commercial kit. The signal was quantified using the *ChemiDoc MT Imaging System (Bio-Rad)*.

Secondary Ab	Origin	Specificity	Reference	Dilution
Anti- IgG	Donkey	Mouse	715-035-151 (Jackson Immunoresearch)	1:5000
Anti-IgG	Donkey	Rabbit	NA934 (Amersham)	1:5000

Table 6.7. Secondary antibodies for WB.

6.3.11 Kindlin-1 detection by immunocytochemistry.

Both HKE6E7 and HKE6E7ΔE6 were grown on respective glass coverslips and fixed in cold methanol/acetone (1:1) for 20 min at room temperature. Cells were incubated in 1X PBS-BSA 3% for 30 minutes at 37°C. and then incubated in primary polyclonal anti-kindlin-1 (*Table 6.6*) in 1X PBS-BSA 3% at 4°C overnight at 1:100 dilution. Secondary antibody (*Alexa Fluor 594, Invitrogen*) was used at 1:1000 dilution for 1h at 37°C. Glass coverslips were mounted using Mowiol

mounting medium (*Hoechst, Somerville, NJ, USA*) and 0.25 ng/mL DAPI (*Sigma-Aldrich*).

6.4 Characterization of generated kindlin-1 deficient cellular model

CRISPR/Cas9 gene editing system was used for the targeted deletion of exon 6 (E6) of *FERMT1* gene, in order to obtain a deficiency in the expression of kindlin-1. For that purpose, a pair of CRISPR RNA guides (gRNA) were designed to induce double strand breaks by Cas9 nuclease within intron sequences flanking the target exon 6 (*Figure 6.5*). Both gRNAs and Cas9 were delivered as a RNP complex by electroporation. After DNA cleavage, NHEJ (non-homologous end joining) DNA repair pathway produces the elimination of the fragment containing the exon 6. This results in a shift in the reading frame and a premature STOP codon formation, leading to the absence of kindlin-1 expression.

- **Obtention of homozygous clones for E6 deletion**

After CRISPR/Cas9 nucleofection, cells were seeded for clone isolation using polystyrene cloning cylinders. 20 clones were isolated and expanded, of which only 16 progressed and were analyzed by PCR, using specific primers from *Table 6.3* for amplification of the fragment containing the gRNA target sites (*Table 6.1*).

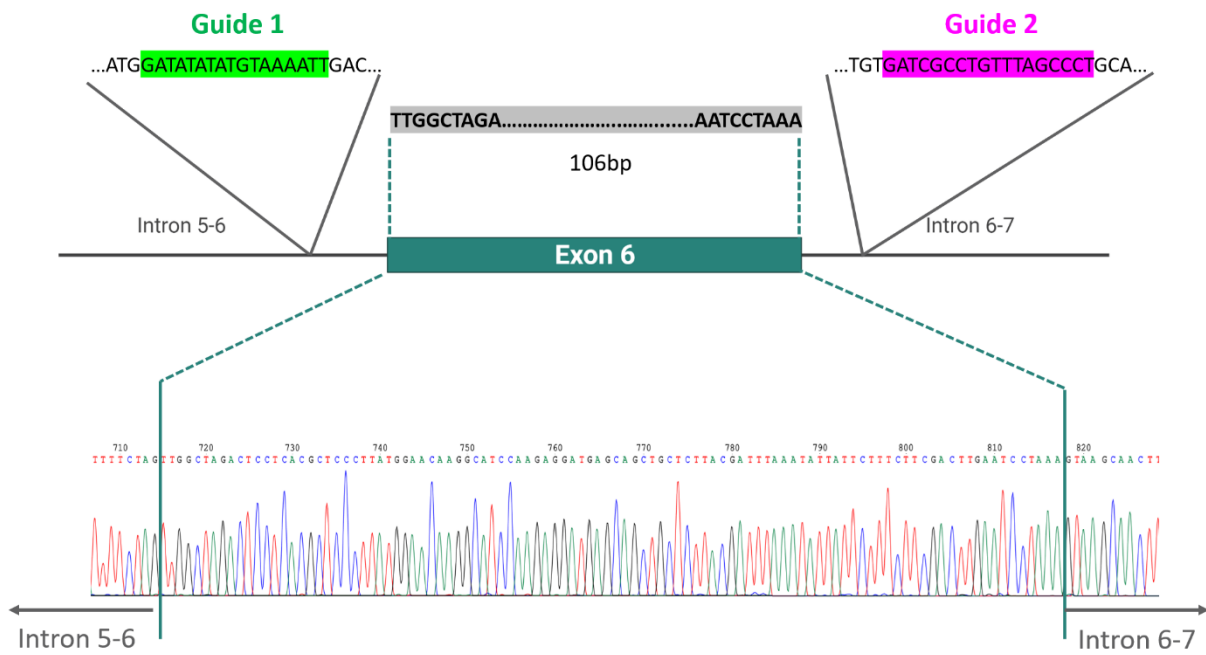


Figure 6.5. Genomic DNA chromatogram of control wild type immortalized human keratinocytes (HKE6E7).

In *Figure 6.6*, wild type control cells (HKE6E7) present a band size of approximately 500 base pairs (bp), corresponding to the amplicon size predicted for PCR primers designed for this study. Samples number 9, 14 and 16 present no deletion. Samples number 1, 2, 3, 5, 6, 7, 8, 10, 11, 12, 13 and 15 are heterozygous, presenting deletion only for one allele. **Sample number 4** shows a homozygous deletion, presenting a band size of approximately 300 bp, which coincides with the size of a band lacking a deleted region of approximately 200 bp.

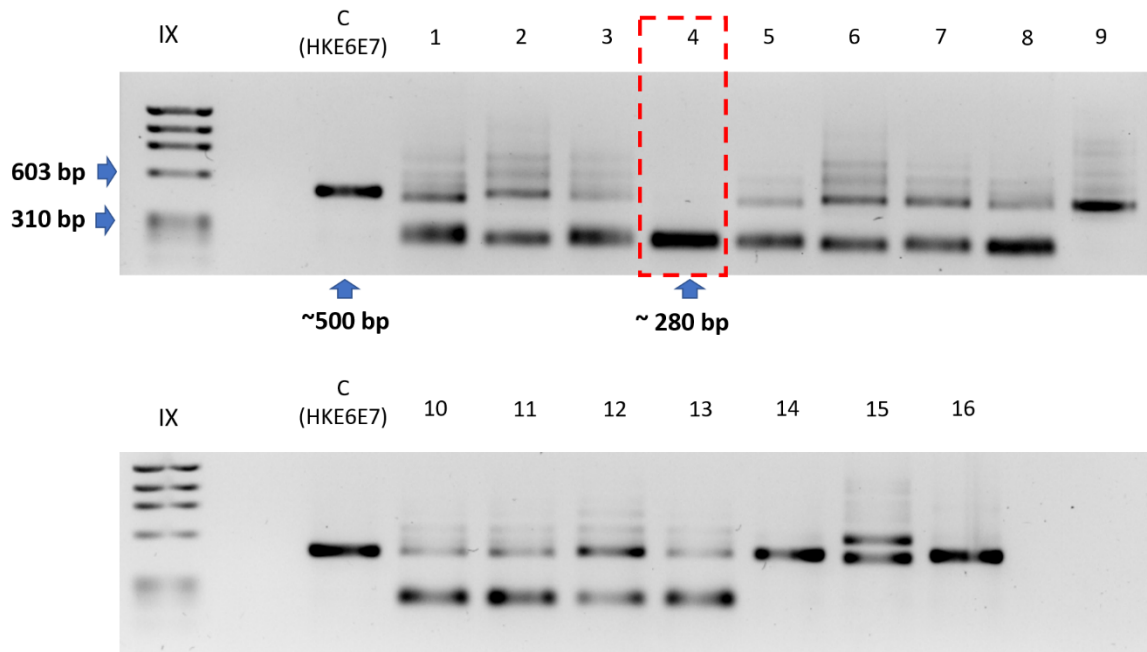


Figure 6.6. PCR analysis for homozygous clones for E6 deletion. C: Control cells (HKE6E7). IX: DNA Molecular Weight Marker IX. bp: Base pairs.

- Analysis of kindling-1 expression in HKE6E7 Δ E6

We next analyzed the expression of *FERMT1* by RT-PCR, amplified with primers in exons 4 and 8 (See primers for RT-PCR in Table 6.2). Control keratinocytes (HKE6E7) produced unedited transcript of approximately ~600 bp. Two smaller bands corresponding to ~500 bp and ~310 bp respectively are detected in edited keratinocytes (HKE6E7 Δ E6) (Figure 6.7).

Exon 6 is 103 bp long, thus, the amplified fragment of ~600 bp will be reduced to an approximately 500 bp fragment. The extra ~310 bp size band shows that different transcripts arise from different indels generated during DNA repair process after Cas9 double-strand cleavage.

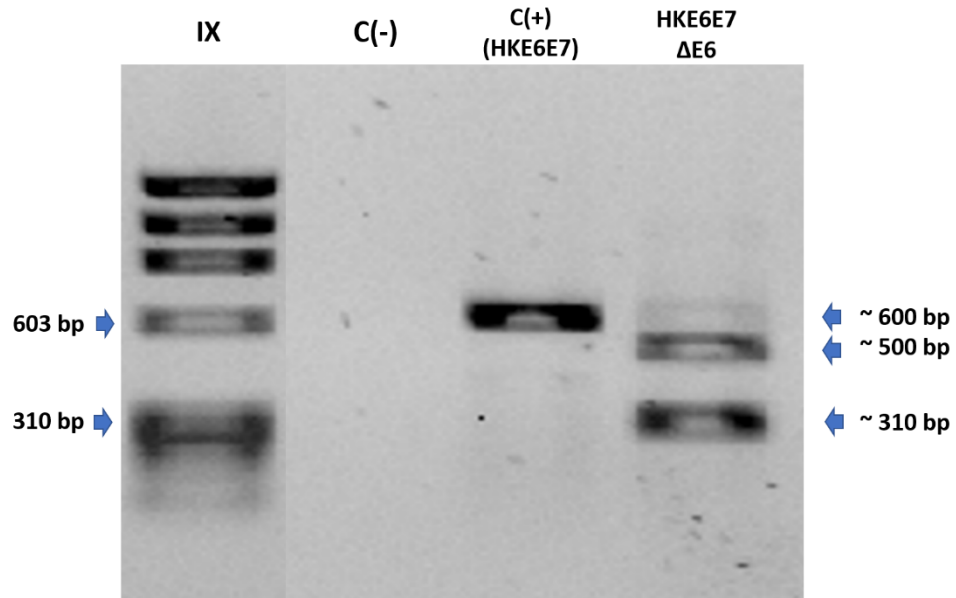


Figure 6.7. *FERMT1* expression analysis in HKE6E7ΔE6 cells. C (-): Negative cDNA control. C (+): Positive cDNA control, wild type cells HKE6E7.

Kindlin-1 expression in HKE6E7ΔE6 cell lysate was analyzed by western blot. HKE6E7ΔE6 showed total absence of the 77 kDa kindlin-1 band in contrast with unedited control HKE6E7 cells (Figure 6.8).

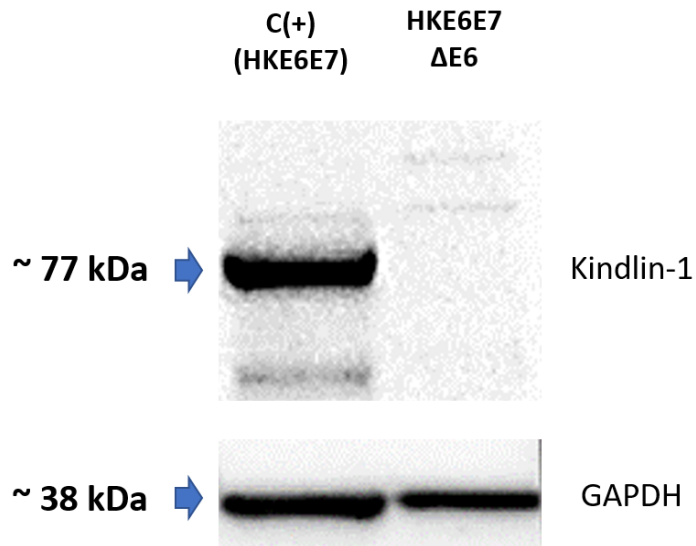


Figure 6.8. Kindlin-1 expression analysis of HKE6E7Δ*FERMT1* cells.

- Sequencing analysis

Characterization of the edited DNA was performed by TA (thymidine-adenine) cloning of both PCR and RT-PCR products and subsequent Sanger sequencing of individual bacterial colonies (n=12 colonies tested for each amplification product). This analysis shows four different DNA end joining repair variants in edited cells, revealing that isolated sample number 4, is actually an oligoclonal population of cells. All sequences analyzed result in the total removal of exon 6 (Figure 6.9).

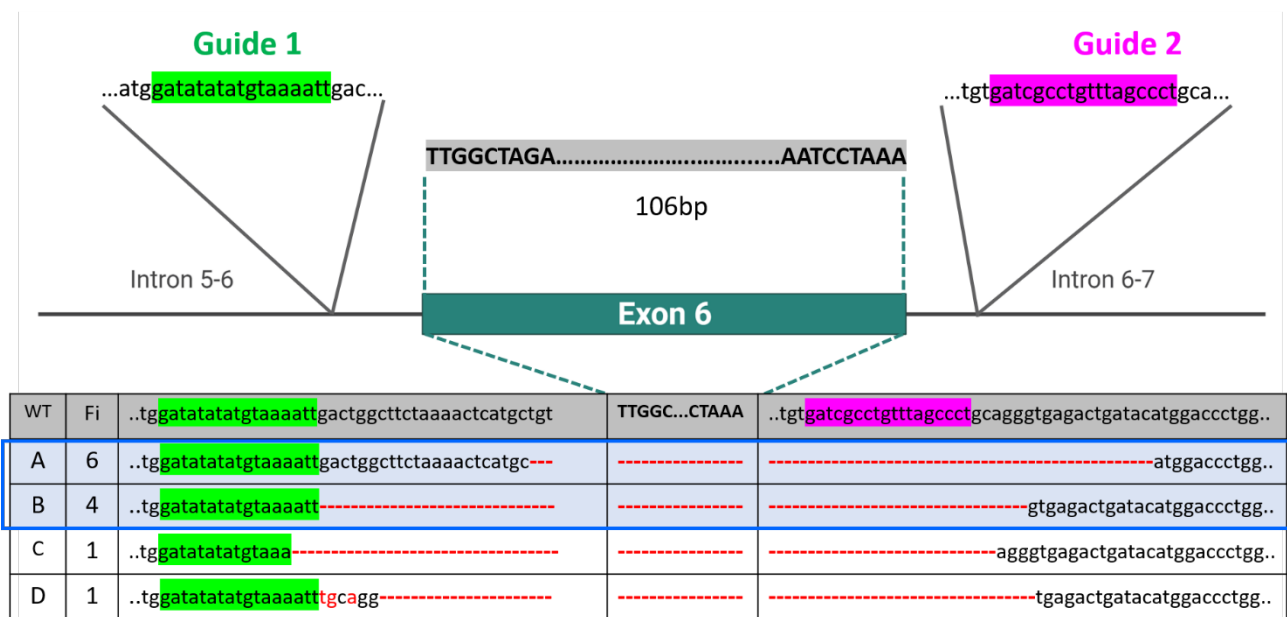


Figure 6.9. Genomic DNA Sanger Sequencing. WT: wild type gDNA sequence (unedited control cells). A- D: insertions and deletions corresponding to DNA repair after Cas9 cuts. Fi. Absolute frequency (n=12). **A and B** were found with an absolute frequency of 6 and 4 respectively. **C and D** were both found with an absolute frequency of 1. **Blue line.** Remarks the most frequent indels.

Approximately 60% of the transcript sequences analyzed resulted in the deletion of exon 5 and exon 6 and 40% of transcripts present deletion of exon 6. This is consistent with the obtained RT-PCR result. Each band in the HKE6E7ΔE6 lane, correspond to transcripts of different sizes: ~500bp band coincides with an amplified cDNA lacking exon 6 and ~ 300 bp band correspond to a transcript lacking both exon 5 and 6. All transcripts lead to the production of a premature stop codon at the beginning of exon 7 (Figure 6.10). As a result, HKE6E7ΔE6 cells

do not produce kindlin-1, as shown by previous western blot analysis (Figure 6.8), making them a suitable cellular model for the following experiments.

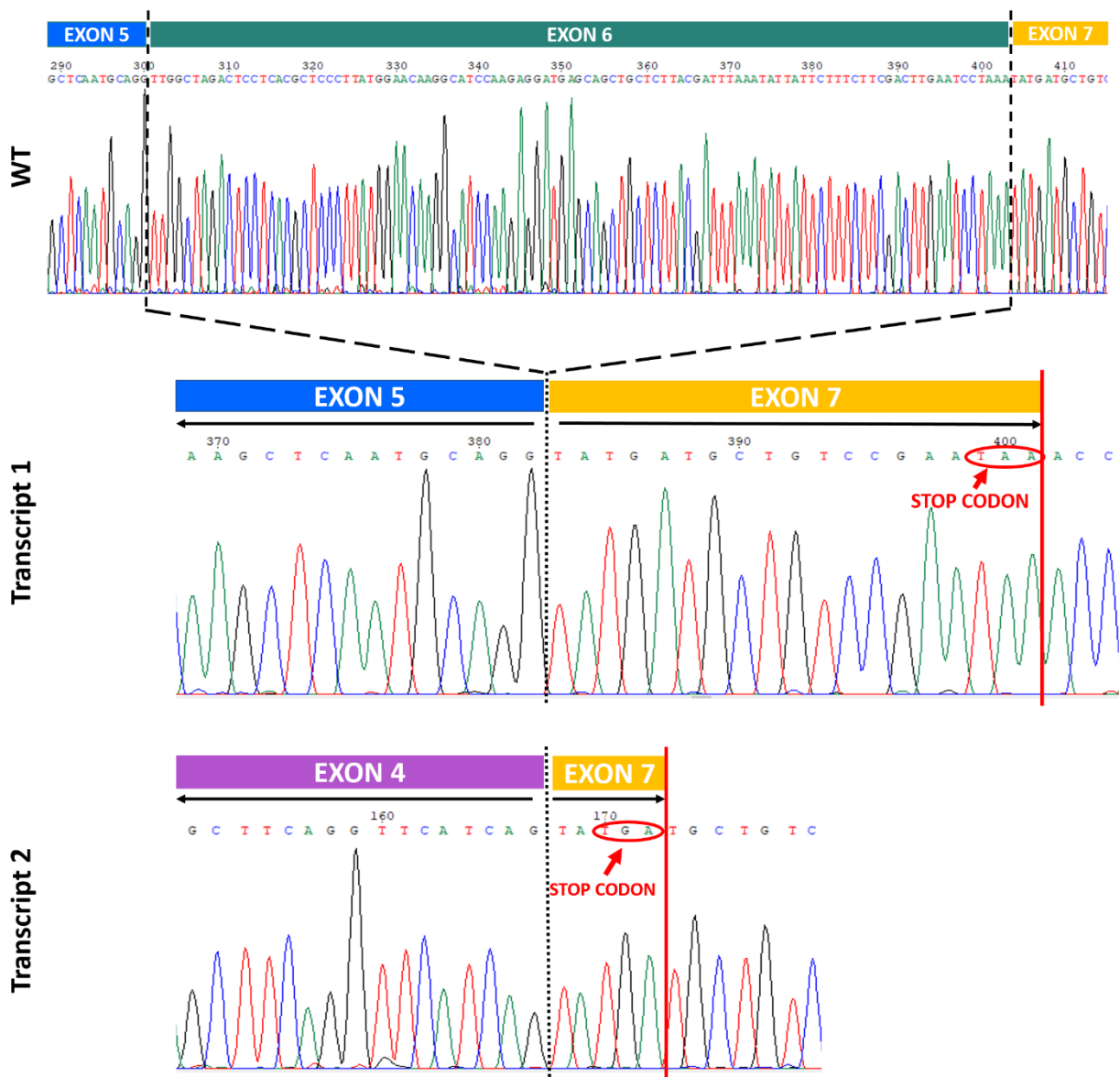


Figure 6.10. cDNA Sanger Sequencing. (From top to bottom). **Wild type cDNA** containing exon6. **Transcript 1:** cDNA sequence from **HKE6E7ΔE6** lacking exon 6. **Transcript 2:** cDNA sequence from **HKE6E7ΔE6** lacking exon 5 and 6. **Stop Codons** are marked in both transcripts (red circle and red vertical line). **Black dashed line** indicates the end and beginning of two consecutive exons.

- **Phenotypic assessment of HKE6E7ΔE6 cells**

HKE6E7ΔE6 cells were observed in culture under microscope to assess its morphology and behavior comparing to HKE6E7 control cells.

It was observed that HKE6E7 Δ E6 cell colonies formed were less rounded and individual migrating cells present elongated shapes extended in opposite directions, in contrast with rounded and unidirectional lamellipodia extended by control HKE6E7 cells (*Figure 6.11*). These features are consistent with those reported in the literature for KS cells. Furthermore, the time needed for detachment from the cell culture plate was reduced by 50% for cells lacking kindlin-1, being 20 minutes for regular detachment of HKE6E7 keratinocytes, and 10 minutes for HKE6E7 Δ E6.

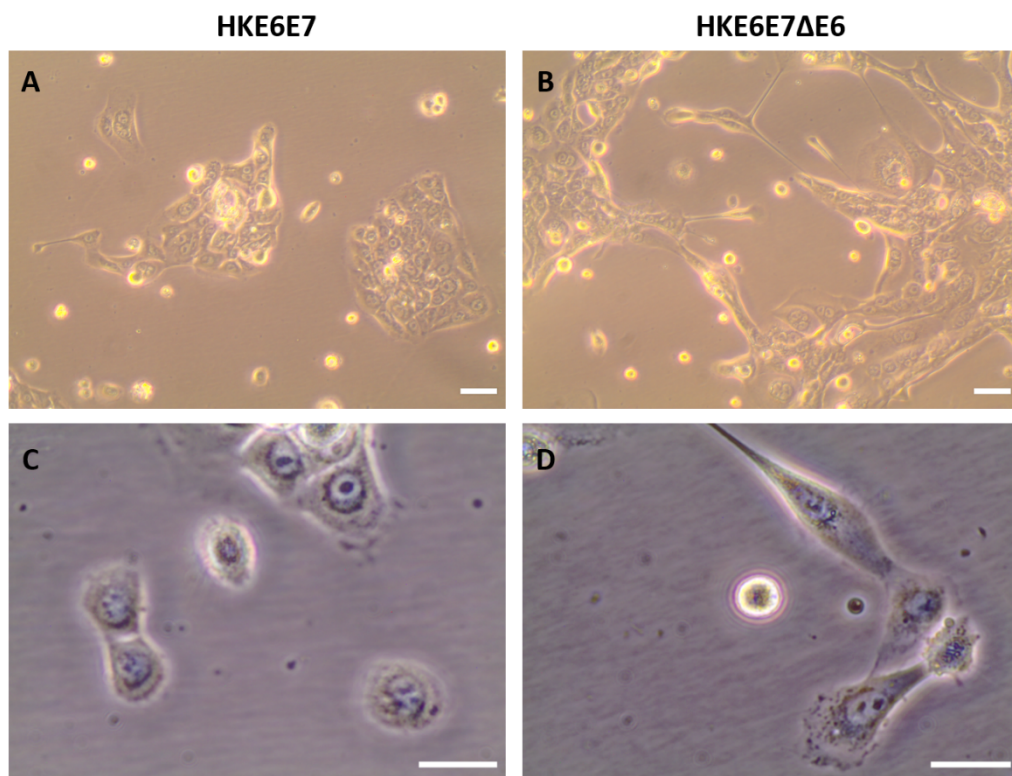


Figure 6.11. Morphological analysis of HKE6E7 Δ E6 cells. *A.* Control HKE6E7 cell colonies. Scale bar= 50 μ m. *B.* HKE6E7 Δ E6 cell colonies. Scale bar= 50 μ m. *C.* Control HKE6E7 individual cells. Scale bar= 25 μ m. *D.* HKE6E7 Δ E6 individual cells. Scale bar= 25 μ m

Finally, the presence of kindlin-1 was also tested by immunofluorescence, in control and edited cells, showing a clear difference in the staining of both samples (*Figure 6.12*).

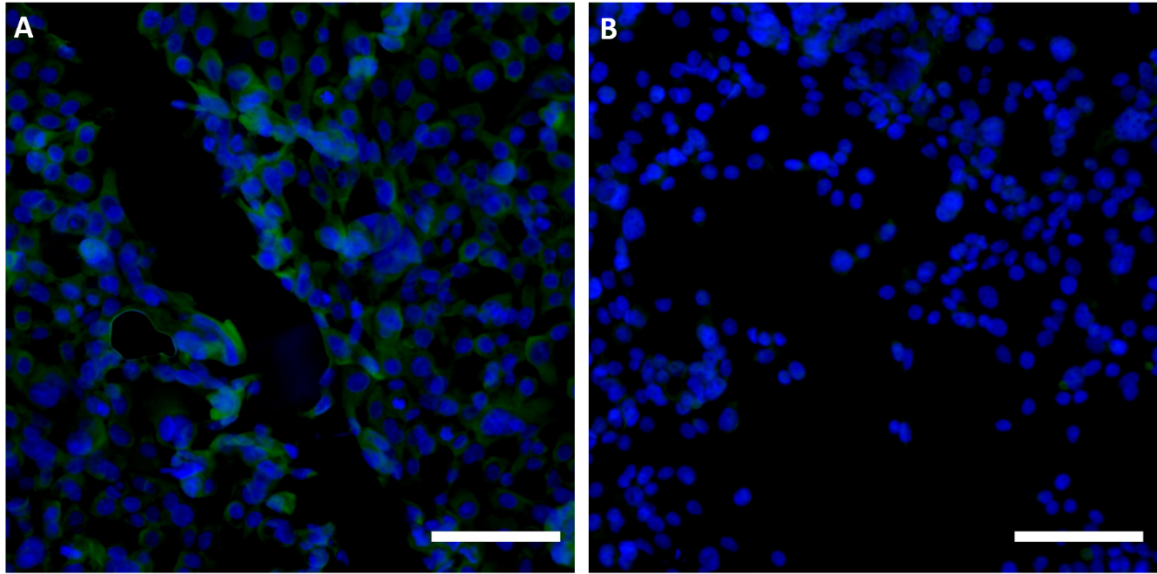


Figure 6.12. Kindlin-1 expression in HKE6E7ΔE6 keratinocytes. A. Control HKE6E7 cells. B. Edited HKE6E7ΔE6 cells. Blue: Nuclear DAPI staining. Green: kindlin-1 staining. Scale bar: 100μm.

6.5 Force measurements in kindlin-1 deficient cells

Kindlin-1 deficient cells previously generated were used for force measurement experiments as previously described in the protocols developed in [chapter 4](#). Hereafter, HKE6E7ΔE6 cells, will be referred as Kin1⁻ cells (kindlin-1 deficient cells) for convenience.

Briefly, a carbon fiber is fixed at one end (fixed end), by gluing it to a 35mm cell culture dish. After functionalization with collagen I, a wound is created by using a custom-made 3D printed stencil. This avoids the cell monolayer scratching and controls the size and homogeneity of the wound. As cells migrate to close the wound, they push the carbon fiber bending it until it reaches a maximum, which coincides with the stop of the monolayer. Time-lapsed imaging is performed under an automated inverted light microscope (*Leica Dmi8, Germany*), taking images every 15 minutes for 120h. Cells were kept under appropriate CO₂, temperature and humidity conditions in an incubator (*OKOlab, Pozzuoli*) throughout the experiment. For more details on materials and methods, [see chapter 4](#).

Carbon fiber of different lengths (L= 2mm, 3mm and 4mm) were used for force measurements of Kin1⁻ cells. In these experiments, L= 5mm was discarded

as it was previously demonstrated that measurements and assumptions made for the fiber-cell monolayer system, do not work correctly for fibers longer than 4mm, since the cell behavior is not homogeneous along the fiber, thus establishing $L=4\text{mm}$ as the limit of our system.

The shape of the fiber over time was analyzed from images to compute the uniform force per unit length, f_0 , that the cells exert along the fiber. *Equation 4.1 from chapter 4* was used to fit these different shapes. Then, time evolution of the uniform force per unit length exerted by both HaCat and Kin1^- cells, is represented in *Figure 6.13*.

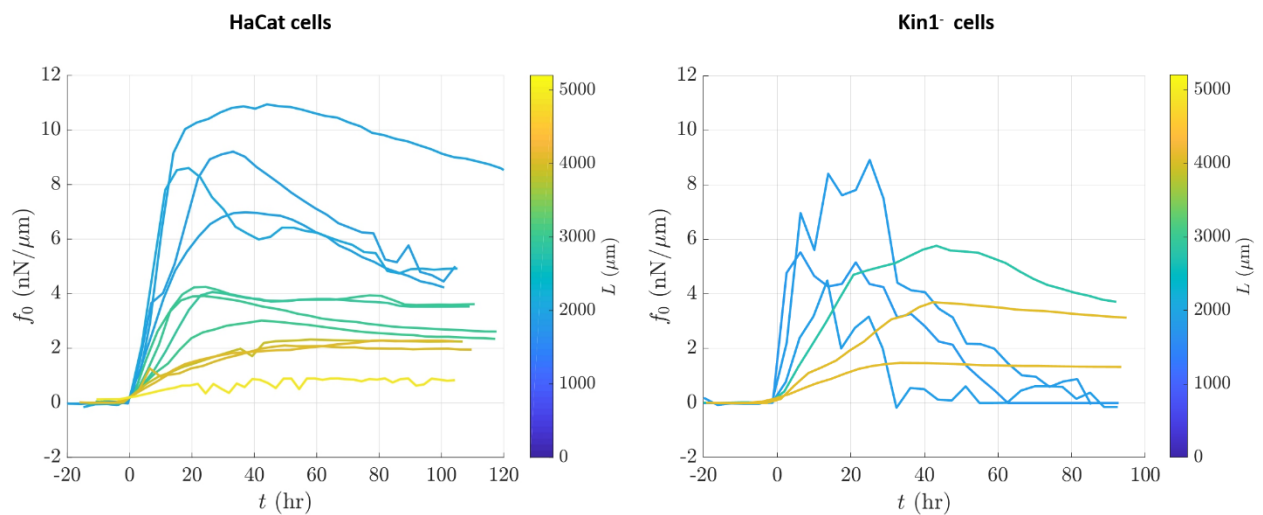


Figure 6.13. HaCat vs. Kin1^- cells. Time evolution of the uniform force per unit length for different fiber lengths Color Scale: length of the fiber. $t=0$: time at which the monolayer reaches the fiber.

We observe in *Figure 6.13*, that curves show a maximum followed by a recoil, that is in more pronounced in the shorter fibers (2mm in blue), that in the longer ones (3 mm in green and 4 mm in yellow). Note that longer fibers are softer (more compliant) and shorter fibers are stiffer (less compliant). The most salient feature is that forces exerted by Kin1^- cells are similar to those obtained by HaCat cells for both 3 mm and 4 mm fibers, while they exert a weaker force on the 2 mm fibers. In addition, that force decays faster once the recoil begins. Thereby, as we observed in the experiments conducted with HaCat cells (*chapter 4*), the viscosity of the tissue provides a certain damping which causes the fiber to describe overdamped and nearly overdamped oscillations.

Since these oscillations depend on the length of the fiber (thus the stiffness), the longer ones reach an asymptotic maximum, while the shorter (stiffer) ones (2 mm) experiment a recoil which is faster in Kin1⁻ cells than in HaCat cells. This suggests that the tissue formed by Kin1⁻ cells is less viscous and therefore provides a lower damping. This may be a direct consequence of a lower anchorage of focal adhesions and impaired intercellular communication commonly found in Kindler syndrome cells^{6,7}.

Regarding the effect of the fiber elasticity on the dynamics of the monolayer, the inverse relationship between the force and the length of the fiber predicted by $f_{0,max} \sim \frac{m^{1/2}u_0(EI)^{1/2}}{L^2}$ (Equation 4.7, chapter 4), also applies to the Kin1⁻ cell monolayer, as it is a property of the fiber, not of the cells (Figure 6.14).

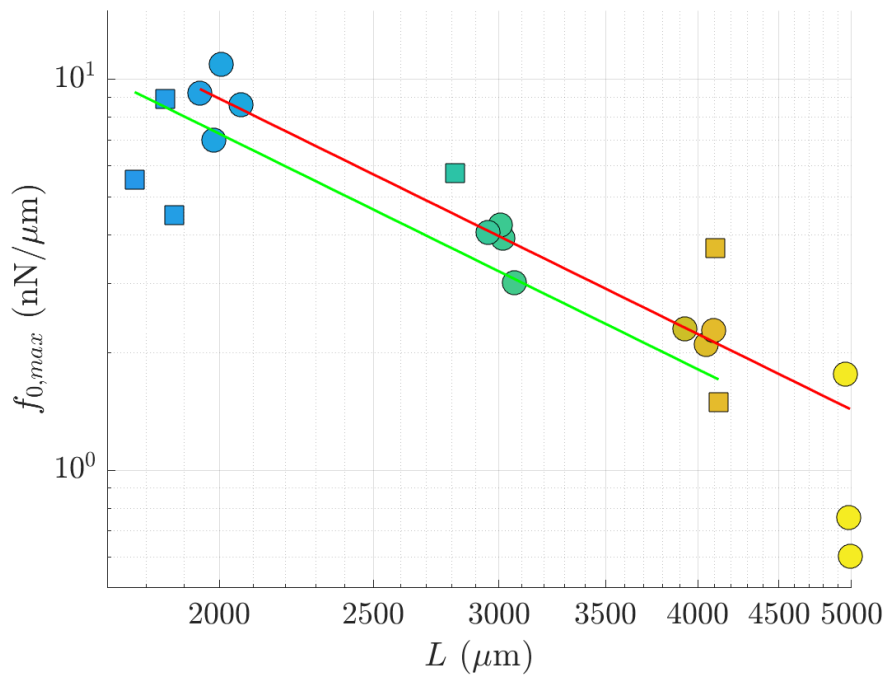
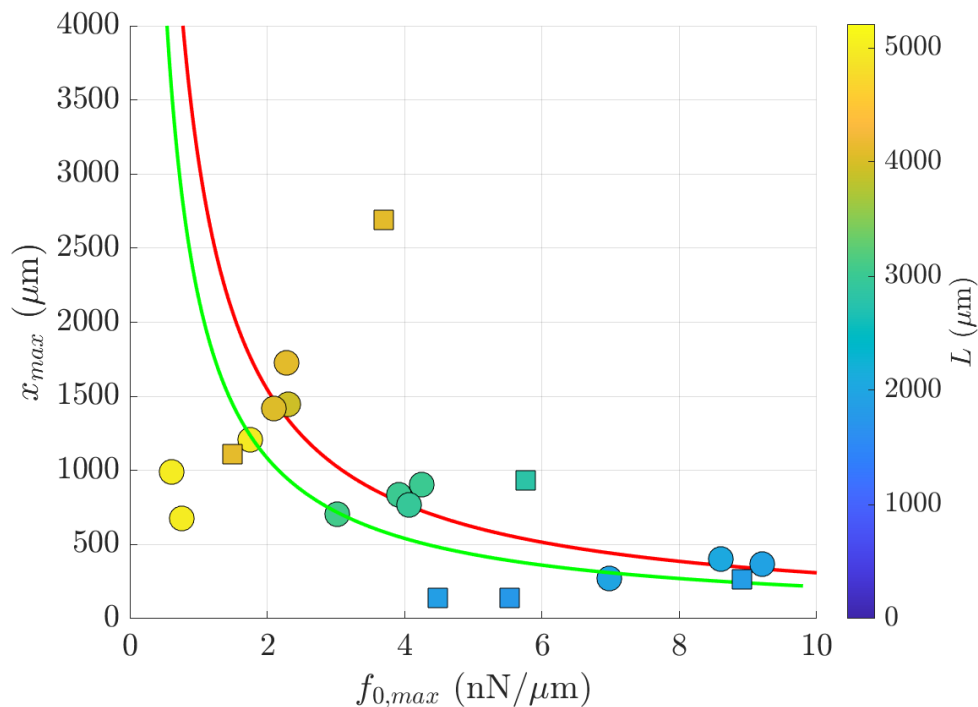


Figure 6.14. Maximum force measured in experiments corresponding to different fiber lengths. Each point corresponds to a single experiment: Circle symbols. Experiments with HaCat cells. Square symbols. Experiments with Kin1⁻ cells. Color code. Indicates the length of the fiber used in this experiment. Solid red line (HaCat cells). Fit with a power law $f_{0,max} \sim C_f \times L^{-2}$. $C_{f_{HaCat}} \approx 3.57 \times 10^7 \text{ nN}\mu\text{m}$. Solid green line (Kin1⁻ cells). Fit with a power law $f_{0,max} \sim C_f \times L^{-2}$. $C_{f_{Kin1-}} \approx 2.9 \times 10^7 \text{ nN}\mu\text{m}$.

Although the reproducibility of these results is not as high as those obtained with HaCat cells (Figure 6.14, circle symbols), we observe the same

tendency with Kin1^- cells: the stronger the resistance of the surrounding environment, the stronger the force that cells are able to exert (*Figure 6.14., square symbols*).

The last observation derived from the theoretical model described in *chapter 4* is that mechanical energy transmitted to the fiber, $f_{0,max}x_{max}$, is constant for different fiber lengths (*Figure 6.15*).



*Figure 6.15. Maximum fiber deflection ($x_{max} = f_{0,max}/k$) as a function of the maximum force, $f_{0,max}$. Each point corresponds to a single experiment: **Circle symbols.** Experiments with HaCat cells. **Square symbols.** Experiments with Kin1^- cells. **Color code** indicates the length of the fiber used in each experiment. **Solid line.** Maximum deflection inversely proportional to the maximum force for **HaCat cells** (Red line: $x_{max} f_{0,max} \approx 3.1 \times 10^3 \text{ nN}$) and for **Kin1^- cells** (Green line: $x_{max} f_{0,max} \approx 2.16 \times 10^3 \text{ nN}$)*

Figure 6.15 shows the relationship between the maximum force exerted by HaCat (circle symbols) and Kin1^- cells (square symbols) and the maximum deflection of different fiber lengths, which adheres to the hypothesis that the work exerted by the cells is the same regardless of fiber stiffness. However, in addition to the lower experimental reproducibility offered by Kin1^- cells, this theory does not fit well for stiffer fibers (2 mm). Possibly, many of the

assumptions of the model (uniform force, cell velocity etc.) are not fulfilled in this type of cells due to their altered mechanical functions.

Under normal wound healing assay conditions, Kin1⁻ cells migrate shorter distances (*Figure 6.16*) and likewise, the tissue hardly expands after overpassing the fiber compared to HaCat cells (*Figure 6.17*).

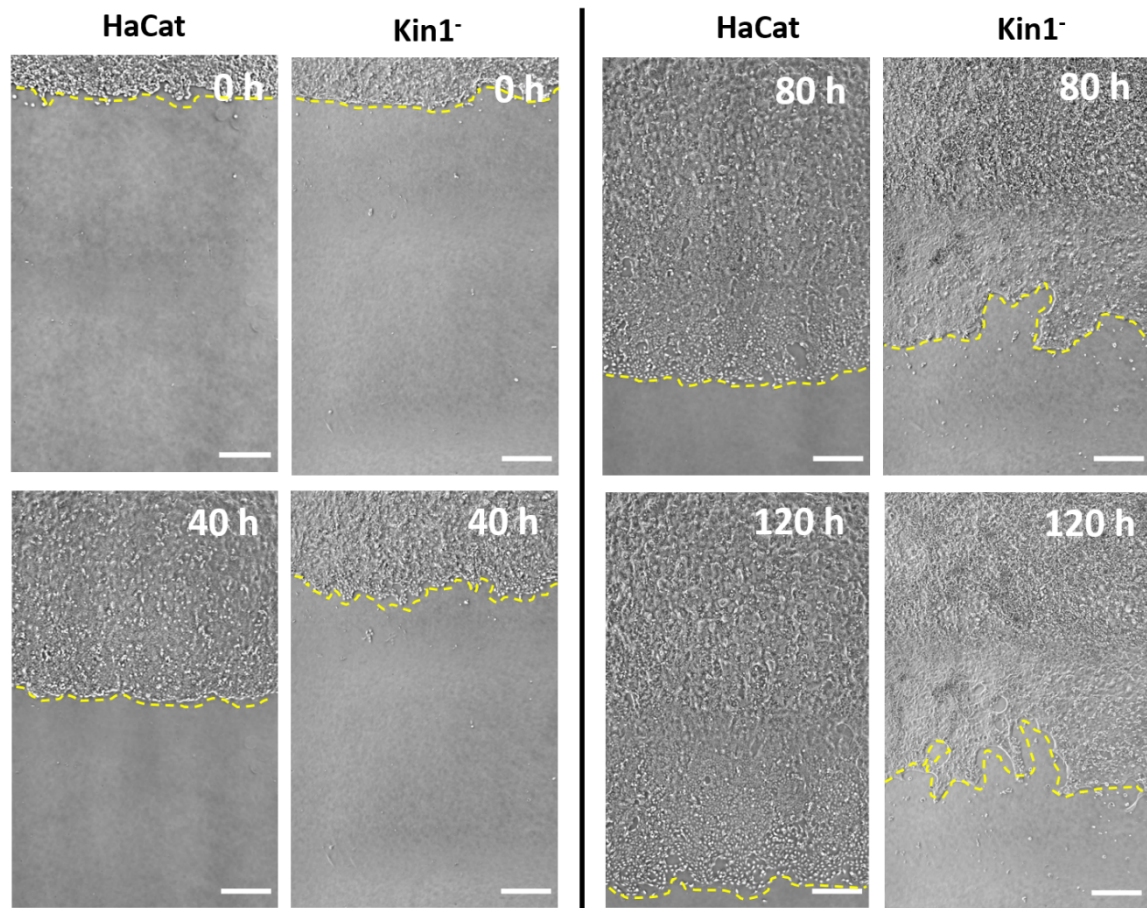


Figure 6.16. Time evolution of migrating HaCat and Kin1⁻ cells (without fiber).

Scale bar = 500 μ m.

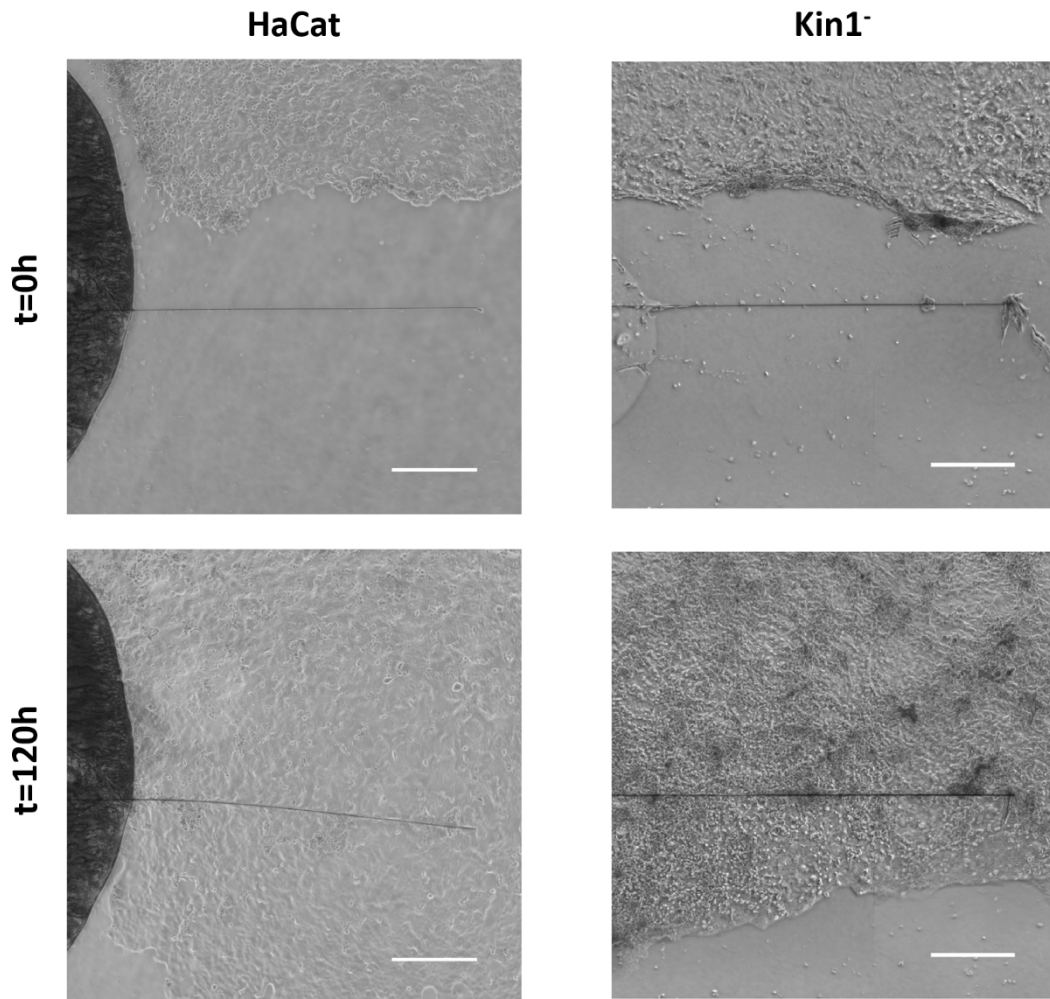


Figure 6.17. Comparison between HaCat and Kin1⁻ cells migrating front (with fiber) at initial and final timepoints. Kin1⁻ cells expand approximately 500-600 μm after the fiber while HaCat cells continue to migrate beyond the field of view. Also, it can be visualized the fiber recoil to the initial position in Kin1⁻ cells. Scale bar = 500 μm .

This is associated to the cell velocity behavior. It has been described that Kin1⁻ cells present random migration and increased cell motility as a consequence of aberrant lamellipodial formation and poor adhesion to substrate^{6,7}, however, there is some controversy in this regard, as other groups confirm that they migrate slower than normal cells^{4,5}. Our results show that cell velocities along the x axis (direction of migration) are less constant in time as compared to HaCat cells. Kymographs of HaCat and Kin1⁻ migrating monolayers without fiber (control experiments) are shown in [Figure 6.18](#). They represent the time evolution of the streamwise velocity, $u(x, t)$, at three different vertical fields as analyzed in [chapter 4](#)

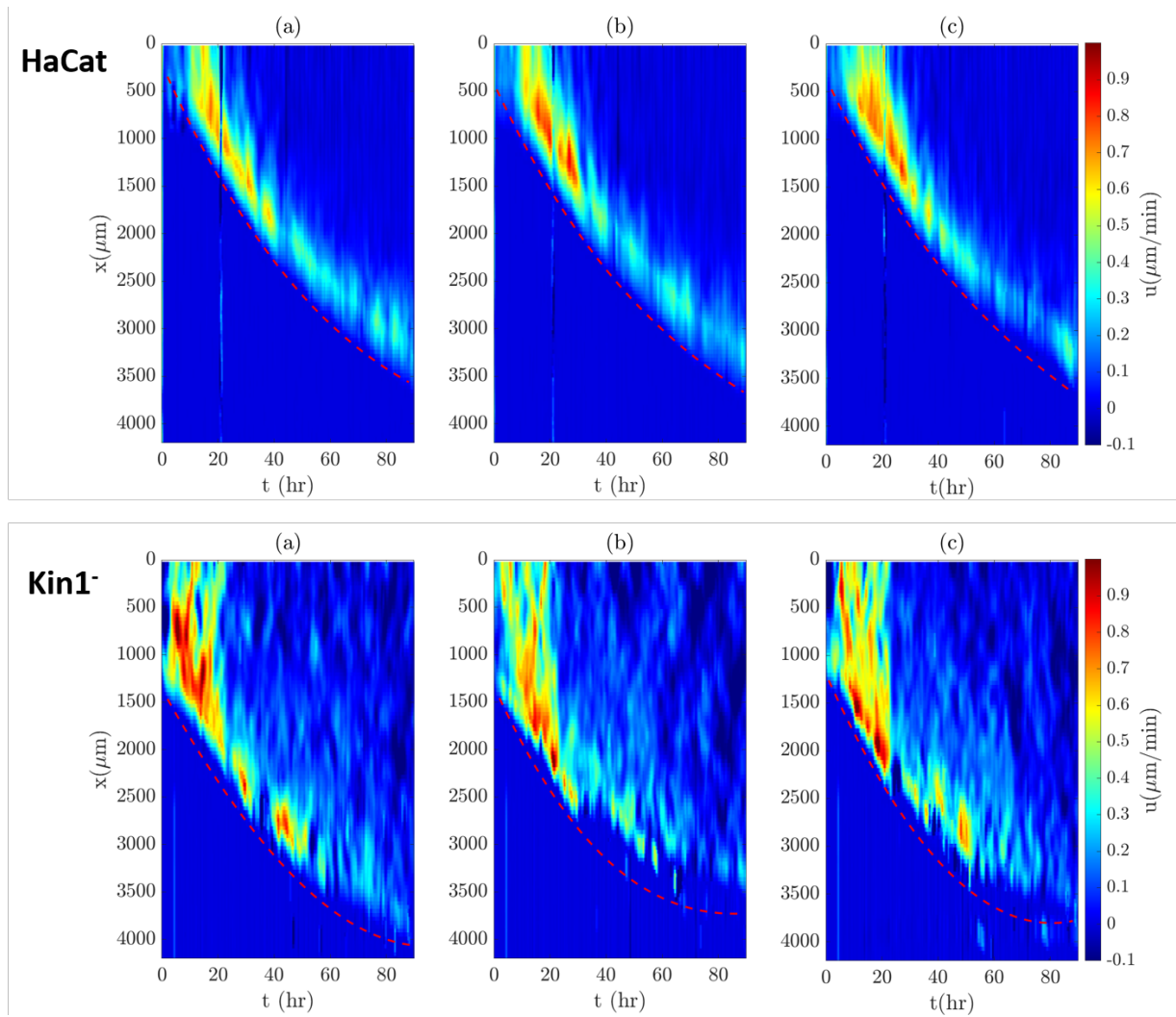


Figure 6.18. Kymographs corresponding to Figure 6.16. Colormap. Time evolution of the streamwise velocity field $u(x, t)$ at three different regions. **Red dashed line.** Front of the monolayer. **Upper row.** HaCat cells. **Bottom row.** Kin1⁻ cells. Velocity values are positive along the x axis (in the direction of migration).

In *Figure 6.18* it is easily visualized that HaCat cells reach high velocities at the beginning of the experiment and decay progressively over time. However, a greater amount of Kin1⁻ cells at the front reach high velocities that are maintained for a longer time and in a more irregular manner, both at the front and in the bulk of the monolayer. This is due to the continued change of direction and chaotic movement of Kin1⁻ cells within the monolayer as a result of poorer coordination between cells.

These behavioral differences can also be easily visualized in PIV analyses.

Figure 6.19 corresponds to a PIV analysis of Kin1⁻ cells before touching the fiber at two different timepoints. Green arrows represent velocity vectors which length depict their magnitude and arrow indicates their direction. It can be observed more than three different zones migrating in different directions: downwards, upwards, parallel to the fiber (red dashed squares) or even describing a vortex (red dashed circles).

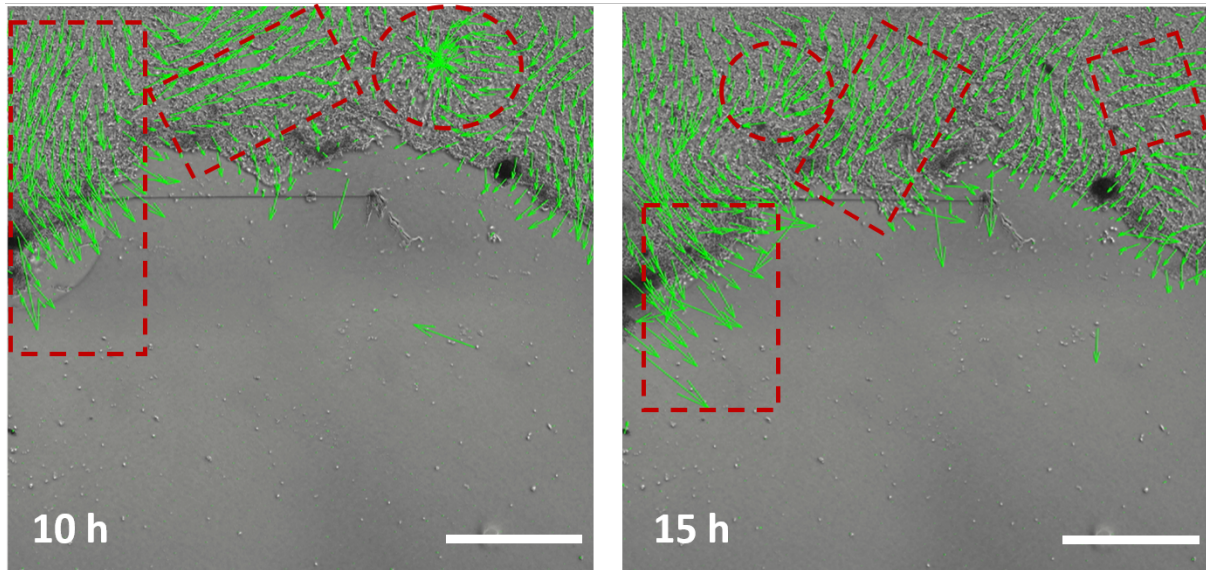


Figure 6.19. PIV analysis of Kin1⁻ cells at two different timepoints. Red dashed circle. Vortices. Red dashed square. Zones of cells migrating in different directions. Scale bar = 1000 μ m.

This uncoordinated and undirected collective cell behavior of Kin1⁻ cells (*Figure 6.20. Right*) is more disorganized than that shown by HaCat cells, which migrate mostly downwards (towards the gap) (*Figure 6.20. Left*).

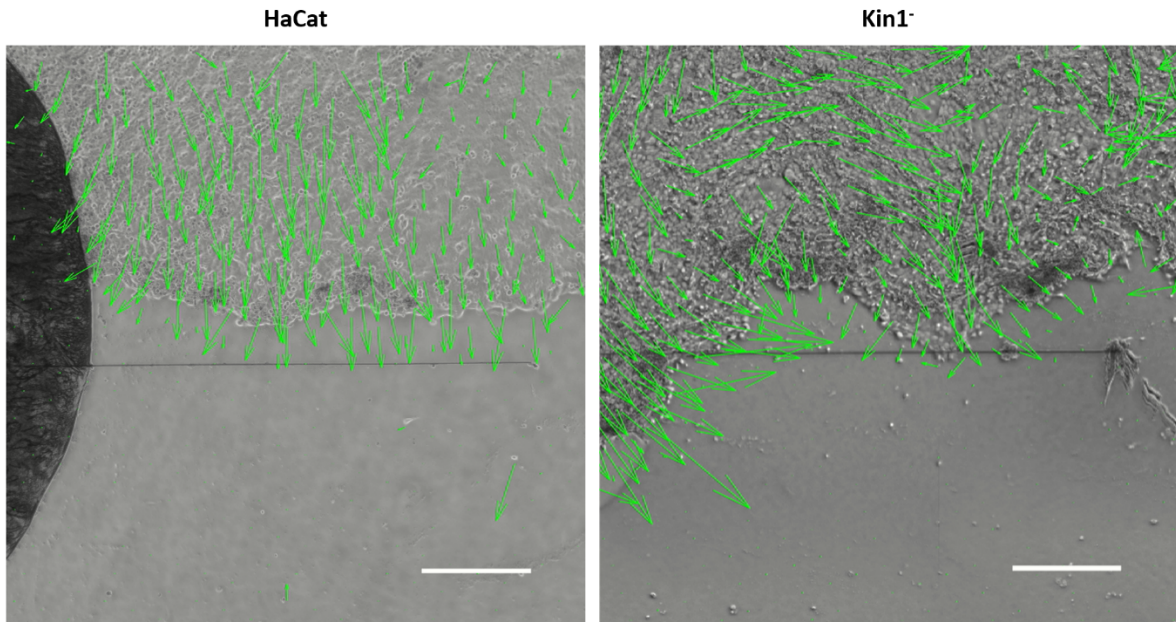


Figure 6.20. PIV analysis (time= 15h). Comparison between collective behavior of HaCat (left) and Kin1⁻ cells (right). Timepoint=15h. Scale bar= 500µm.

The streamwise velocity, $u(x, t)$, was also analyzed for different fiber lengths (Figure 6.21). Cell velocities in the experiments with fiber shown a similar pattern than that observed in controls without fiber: fast and intermittent velocities over time. The fiber causes a premature stop of the monolayer compared to control experiments (Figure 6.18. Lower row), as previously observed in HaCat cells, but the heterogeneity of movement and velocity is sustained over time. As explained above, this is due to the change of direction of cells. This confirms that Kin1⁻ cells move faster but the monolayer is not able to migrate as a whole as efficiently as normal cells to close the gap.

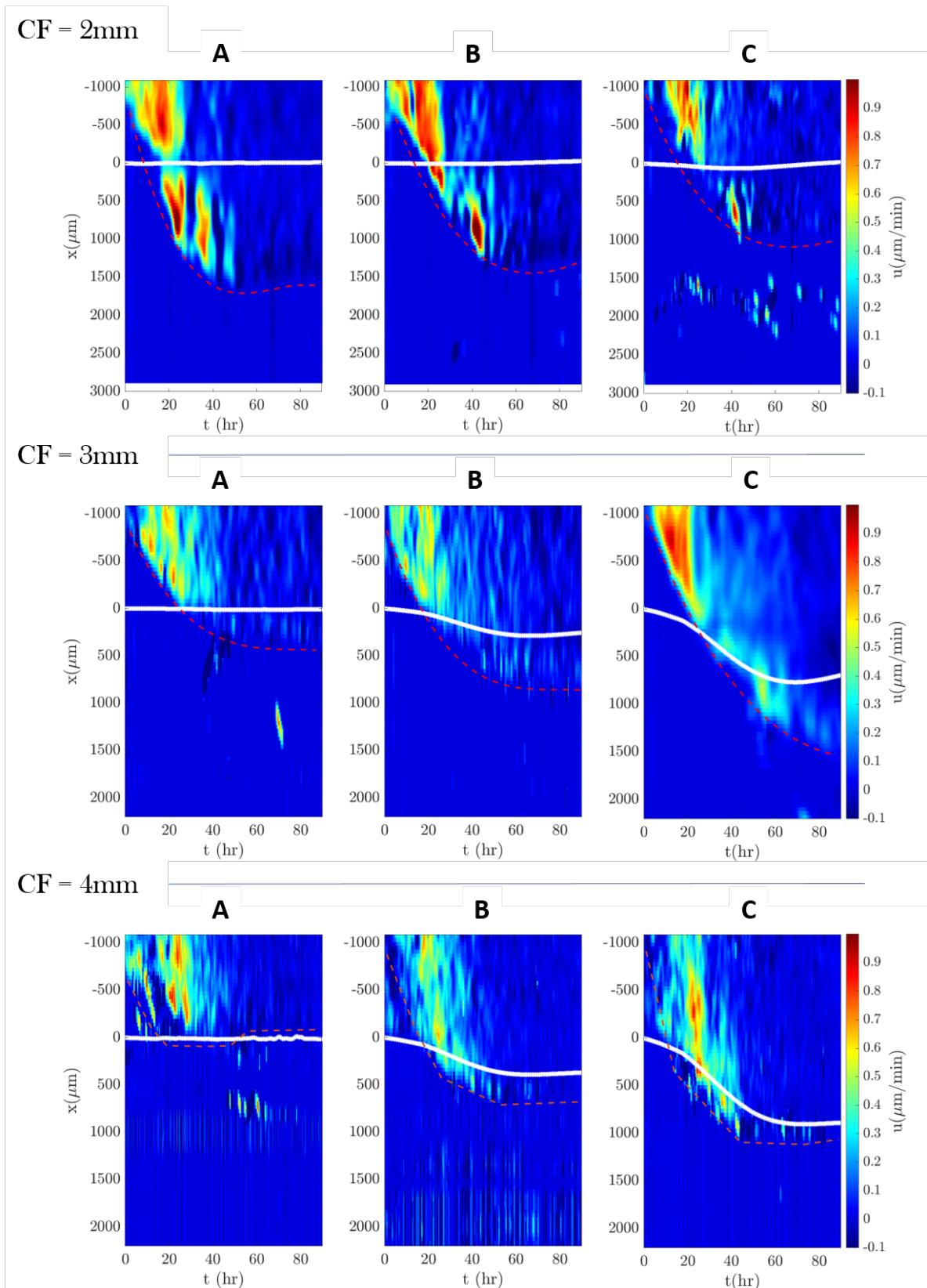


Figure 6.21. Kymographs ($Kin1^{-}$ cells). Colormap. Time evolution of the streamwise velocity field $u(x, t)$ at three different regions: A (fixed end), B (middle region) and C (tip). **White thick line.** Fiber deflection. **Red dashed line.** front of the monolayer. **CF.** Length of the carbon fiber. 2mm, 3mm and 4mm for the upper, middle, and bottom rows respectively. Velocity values are positive along the x axis (in the direction of migration).

6.6 Discussion

Together with many other molecules, **Kindlin-1** is an important member of **focal adhesions** that plays an essential role in integrin activation. Kindlin-1 mediates this activation by its binding to the intracellular domain of the β -integrin monomer, causing a conformational change that increases integrin affinity for its ligands, thus establishing a link between the ECM and the intracellular cytoskeleton. Ligand binding to β -1 integrins triggers the recruitment of molecules for the formation of a **dynamic macromolecular complex** known as “integrin *adhesome*”, “molecular clutch” or most common “focal adhesion”. The integrin *adhesome* performs several interconnected functions that mediate integrin signaling, clustering of integrin receptors, regulation of actin polymerization and force transduction. This set of events regulate basic cell functions such as proliferation, differentiation and migration^{7,15,16}.

These molecular complexes governed by integrin adhesion, make possible the establishment of mechanoreciprocity between the extracellular environment and intracellular tension. Thus, cells are able to transmit forces to its substrate, which is an essential step in cell body translocation during cell migration. Conversely, the molecular clutch provides the cell with mechanosensitive ability, allowing it to modify its behavior in accordance with different rigidities offered by the environment^{13,14}.

Kindler Syndrome is a rare disease produced by the loss of function of protein kindlin-1, caused by mutations in *FERMT-1* gene. This disease manifests features derived from a deficiency in cell adhesion function, producing a variety of clinical complications, such as the characteristic skin blisters common to the *epidermolysis bullosa* family of skin disorders. At the cellular level, *in vitro* KS keratinocytes present aberrant cell shapes and migration patterns and lower rates of proliferation, which deeply affect wound reepithelization⁴.

Bringing this into the context of our study, we considered that Kindler syndrome cells are good candidates to be assessed under our experimental conditions. Since they do not migrate regularly and, based on previous studies¹⁰,

kindlin proteins play a mechanosensitive role as a part of the FA complexes, we expect them to show different dynamic and kinematic patterns compared to healthy cells that express normal levels of kindlin-1.

To confirm this hypothesis, we analyzed the forces exerted by kindlin-1 deficient cells on a carbon fiber, as they migrate in response to the generation of a controlled wound within the 2D cell culture. Experimental conditions were configured following the same protocols established for the previous measurements performed with HaCat cells in [chapter 4](#). We tested the sensitivity of the 2D force measurement technique to detect dynamic differences between cells exhibiting different phenotypes.

Kindler syndrome is a rare disease with a very low prevalence. Therefore, the availability of patient biopsies is very limited. Hence, for this study we generated a kindlin-1 deficient cellular model, which recapitulates the KS phenotype ([Figure 6.11](#)). CRISPR/Cas9-mediated gene editing, has been described as a highly efficient tool for generation of disease models, as previously reported for Netherton Syndrome modeling²¹ or for the generation of animal models of human disease^{25,26}. Thereby, we chose CRISPR/Cas9 technology as a gene editing tool, to address the deletion of a specific region of the *FERMT1* gene.

Previously immortalized human keratinocytes HKE6E7, were selected to be edited by electroporation of two RNA guides and a Cas9 nuclease, delivered as an RNP complex. Both gRNAs were designed to target intron 5-6 and intron 6-7 respectively, to achieve the deletion of exon 6. Edited keratinocytes were seeded after electroporation to obtain isolated clones. After PCR analysis of sixteen isolated cell colonies, only colony number 4 showed a single PCR band ([Figure 6.6](#)), indicating homozygosity for the target deletion. Then, colony number 4 was characterized by TA cloning of both PCR and RT-PCR products and subsequent Sanger sequencing. Genomic DNA sequencing revealed that the selected cell colony number 4, in addition to the targeted exon 6 deletion produced by Cas9 nuclease cuts, also shows a variety of indels (insertions and deletions) ([Figure 6.9](#)). Thus, the edited cell population is oligoclonal. However,

this does not represent a drawback for our study since DNA cleavage by gRNA-guided Cas9 nuclease and subsequent DNA repair events resulted in null alleles. This caused a shift in the reading frame and a premature STOP codon formation, leading to the absence of kindlin-1.

For further characterization of the selected HKE6E7ΔE6 cells, kindlin-1 expression was assessed by RT-PCR and cDNA sequencing, revealing two mRNA transcripts lacking exon 5 and exon 6 and exon 6 respectively. Both transcripts lead to premature termination codons formation, which result in the absence of protein expression. This was confirmed by western blot and immunofluorescence (*Figure 6.8 and Figure 6.12 respectively*). Furthermore, HKE6E7ΔE6 cells recapitulate the characteristic phenotype of *in vitro* KS cells: abnormal shape and migration patterns, lower proliferation and faster detachment from the culture plate comparing to unedited cells, consistently with the characteristics reported in previous works^{4,9}.

Taken these results together, we confirmed that the generated HKE6E7ΔE6 kindlin-1 deficient cellular model, hereafter Kin1⁻ cells, constitutes a valid model for the planned force measurement experiments.

Results derived from force measurements of migrating Kin1⁻ cells, revealed expected differences when compared with those obtained from HaCat cells *chapter 4*. Surprisingly, they exerted very similar forces when pushing a 3mm or 4mm fiber, while those exerted against 2mm fibers were reduced. Furthermore, the recoil experienced by the 2mm fiber is faster in Kin1⁻ cells, resulting in a steeper slope in the representation of the time evolution of the force uniformly exerted along the fiber (*Figure 6.13*).

Although it has been described that the total amount of β1 integrin is not affected by kindlin-1 deficiency⁴, a later study demonstrates that F3 domain of kindlin-1 (containing PTB fold that binds to β integrin tail)¹¹ is essential for targeting kindlin-1 to FAs and integrin trafficking towards cell membrane⁷. Thereby, kindlin-1 deficiency reduces β1 integrin cell surface expression, although its activation remains unaltered. This is due to the compensatory role of kindlin-2. However, kindlin-2 is unable to fully reverse the lack of kindlin-1,

so kindlin-1-deficiency causes a reduction in integrin-mediated cell adhesion, which accounts for the increased cell motility⁷.

Reduced FA assembly and impaired integrin signaling is reflected in the poor ability to form lamellipodia and maintain cell polarization in absence of kindlin-1. In normal cells, the existence of a wound edge induces the engagement of FA at the leading front, which triggers integrin signaling and activation of Rho-GTPases to drive actin polymerization and lamellipodia formation²⁷. However, patient-derived Kindler syndrome cells show a significantly reduced Rho-GTPases activity and thus decreased F-actin stability. This leads to an increased actin turnover and undirected migration⁴. Furthermore, it has been reported that kindlin-1 deficient cells show a decreased expression of several molecules involved in cell adhesion, such as E-Cadherin, which causes the wound front to no longer maintain its integrity and cells begin to migrate independently⁶.

Gathering all this information, it could be reasonable to support the hypothesis that $Kin1^-$ cells present higher cell motility because the lack of kindlin-1 reduces the number of focal adhesions. The amount and distribution of FAs also could explain why $Kin1^-$ cells presented similar maximum forces for longer fibers (3mm and 4mm), but lower for stiffer ones (2mm). It is conceivable to think that FAs formed by the compensatory function of other molecules (i.e. kindlin-2) are enough to overcome the less rigid fibers. However, when a stronger force is required, cells need to recruit a large number of adaptor proteins to strengthen cell-ECM adhesions and form integrin clusters. This leads to an overall actomyosin cytoskeleton reinforcement and promotion of cell migration in normal cells. In this case, the rigidity sensing function of $Kin1^-$ cells is altered due to their reduced ability to form FAs, which could be reflected in the inability to generate sufficient traction force to overcome stiffer obstacles.

In addition, we studied collective migration, in which the maintenance of intercellular contacts is essential for the transmission of the mechanical stress produced at the cell front, for a correct migration and pushing of the fiber. Since kindlin-1 deficiency has been shown to reduce the expression of some

intercellular adhesion molecules⁶, including E-Cadherin, it is to be expected that impaired intercellular communication and weaker cortical stiffening prevents Kin1⁻ cells to properly reorganize and reinforce its cytoskeleton to migrate or in response to an external obstacle. This is consistent with a more chaotic collective behavior compared to the synchronized migration exhibited by HaCat keratinocytes (*Figure 6.19 and Figure 6.20*).

Regarding the contradictory results observed^{4,5,6,7} by other groups, here we found that, instead of progressively decrease over time, cell velocities oscillate between high and low velocity peaks until they stop (*Figure 6.21*). In all cases, regardless of the presence of the fiber, we observed impaired wound closure compared to HaCat cells (*Figure 6.16*). Both events seem to be correlated, since random and undirected migration appear to be the reason why they fail to close the wound. This explains that, although Kin1⁻ cells move quickly, the monolayer cannot advance longer distances because they do not maintain the collective behavior due to the fact that their mechanotransduction and intercellular communication mechanisms do not properly work (*see the vortices in Figure 6.19 red dashed circles*). This approach could help to clarify those contradictory results obtained by different authors, in terms of velocities and wound closure, by studying how single cells are integrated within the collective movement.

On the other hand, the increased actin turnover produced by an impaired Rho-GTPase signaling observed in cells from Kindler syndrome patients⁴, may be the cause of a reduced mechanical work exerted by Kin1⁻ cells (*Figure 6.15*). The enhanced membrane plasticity produced by an increased protrusion-retraction rate, possibly requires a high energy demand. Cell migration, epithelial to mesenchymal transition, and actin remodeling in response to mechanical forces are the major energy consumers. These processes require an increase in cell metabolism whose interplay with actin dynamics has yet to be explored²⁸. A recent study has demonstrated that applied forces on E-Cadherin activates AMPK (AMP-activated protein kinase), which acts as an energy sensor in cells, and regulates cell metabolism through the ATP:ADP ratio required for cytoskeleton reinforcement²⁹. Also, an increased integrin

engagement and actin bundling in response to a stiffer environment, produces the sequestration and inactivation of a cytosolic ubiquitin ligase that regulates the degradation of metabolic enzymes, thus resulting in increased glycolytic activity³⁰. Therefore, according to these arguments, it is possible that mechanical sensing through FAs and force transmission through E-Cadherin may activate metabolic pathways to supply more energy in the case of softer fibers. Nevertheless, a stiffer environment (2 mm fiber) cannot trigger this activation because the rigidity sensing function is impaired in Kin1⁻ cells. Consequently, Kin1⁻ cells deliver less mechanical work than HaCat cells (*Figure 6.15*). Nonetheless, although they follow roughly the same trend, the scatter of the data associated to the more erratic behavior of Kin1⁻ cells does not allow us to state that they follow precisely the prescribed equations (*Figure 6.15, square symbols*). This is to be expected, considering its poor adhesion to the substrate and all the consequences derived from it. It would be reasonable to suggest that Kin1⁻ cells are unable to coordinate the machinery needed to generate enough energy to restructure their cytoskeleton in stiffer environments. In addition, the lack of cellular coordination probably causes the individual efforts of each cell, aimed at closing the wound and/or overcoming an obstacle, to consume more energy than normal cells. This hypothesis could be tested by means of ATP:ADP ratiometric measurements which we plan to conduct as a next step (*see chapter 7, Future perspectives*)

In conclusion, force measurement results lead to the need for an in-depth study of the metabolic and mechanotransduction pathways affected, both in healthy and Kin1⁻ cells, and to determine how they are altered under our experimental conditions with respect to that described by other authors. Moreover, a higher number of replicates must be performed to compensate for low reproducibility of experiments with Kin1⁻ cells. This variability among experiments may be due, in part, to the poor coordination and random behavior of Kin1⁻ cells. This, besides decreasing the reproducibility of the results, also affects other parameters of the model that assume uniform forces and velocities along the fiber. Despite this, we find that the correlations predicted by the theoretical model, both the effect of stiffness on the dynamics of the monolayer

and the relationship between the maximum elastic energy, deflection and force, are in reasonable agreement with the experiments (*Figure 6.14, square symbols*), except for the stiffest fibers (*Figure 6.15, square symbols*).

Finally, the force measurement technique proposed in this thesis proved to be sensitive enough to detect changes in the forces exerted by different cell types, establishing the sensitivity threshold in fibers below 3 mm for Kin1⁻ cells. This confirms its potential usefulness in the study of diseases involving phenotypes with mechanotransduction defects.

1. Youssefian, L., Vahidnezhad, H. & Uitto, J. Kindler Syndrome. *GeneReviews* 1–19 (2016).
2. Fine, J. D. *et al.* The classification of inherited epidermolysis bullosa (EB): Report of the Third International Consensus Meeting on Diagnosis and Classification of EB. *J. Am. Acad. Dermatol.* **58**, 931–950 (2008).
3. Herz, C. *et al.* Kindlin-1 is a phosphoprotein involved in regulation of polarity, proliferation, and motility of epidermal keratinocytes. *J. Biol. Chem.* **281**, 36082–36090 (2006).
4. Has, C. *et al.* Kindlin-1 is required for RhoGTPase-mediated lamellipodia formation in keratinocytes. *Am. J. Pathol.* **175**, 1442–1452 (2009).
5. Kloeker, S. *et al.* The Kindler Syndrome Protein Is Regulated by Transforming Growth Factor- β and Involved in Integrin-mediated Adhesion. *J. Biol. Chem.* **279**, 6824–6833 (2004).
6. Qu, H., Wen, T., Pesch, M. & Aumailley, M. Partial loss of epithelial phenotype in kindlin-1-deficient keratinocytes. *Am. J. Pathol.* **180**, 1581–1592 (2012).
7. Margadant, C., Kreft, M., Zambruno, G. & Sonnenberg, A. Kindlin-1 Regulates Integrin Dynamics and Adhesion Turnover. *PLoS One* **8**, 1–10 (2013).
8. Yates, L. A. *et al.* Structural and functional characterization of the kindlin-1 pleckstrin homology domain. *J. Biol. Chem.* **287**, 43246–43261 (2012).
9. He, Y., Esser, P., Heinemann, A., Bruckner-Tuderman, L. & Has, C. Kindlin-1 and -2 have overlapping functions in epithelial cells: Implications for phenotype modification. *Am. J. Pathol.* **178**, 975–982 (2011).
10. Jahed, Z., Haydari, Z., Rathish, A. & Mofrad, M. R. K. Kindlin Is Mechanosensitive: Force-Induced Conformational Switch Mediates Cross-Talk among Integrins. *Biophys. J.* **116**, 1011–1024 (2019).
11. Rognoni, E., Ruppert, R. & Fässler, R. The kindlin family: Functions, signaling properties and implications for human disease. *J. Cell Sci.* **129**, 17–27 (2016).
12. Larjava, H., Plow, E. F. & Wu, C. Kindlins: Essential regulators of integrin signalling and cell-matrix adhesion. *EMBO Rep.* **9**, 1203–1208 (2008).
13. Sun, Z., Guo, S. S. & Fässler, R. Integrin-mediated mechanotransduction. *J. Cell Biol.* **215**, 445–456 (2016).
14. Sun, Z., Costell, M. & Fässler, R. Integrin activation by talin, kindlin and mechanical forces. *Nat. Cell Biol.* **21**, 25–31 (2019).
15. Zhu, L., Plow, E. F. & Qin, J. Initiation of focal adhesion assembly by talin and kindlin: A dynamic view. *Protein Sci.* **5392**, (2020).
16. Levy, L., Broad, S., Diekmann, D., Evans, R. D. & Watt, F. M. β 1 Integrins regulate keratinocyte adhesion and differentiation by distinct

- mechanisms. *Mol. Biol. Cell* **11**, 453–466 (2000).
17. Li, H. *et al.* Structural basis of kindlin-mediated integrin recognition and activation. *Proc. Natl. Acad. Sci. U. S. A.* **114**, 9349–9354 (2017).
 18. Michael, M. *et al.* Kindlin-1 Regulates Epidermal Growth Factor Receptor Signaling. *J. Invest. Dermatol.* **139**, 369–379 (2019).
 19. Shen, C., Sun, L., Zhu, N. & Qi, F. Kindlin-1 contributes to EGF-induced re-epithelialization in skin wound healing. *Int. J. Mol. Med.* **39**, 949–959 (2017).
 20. Choi, M. *et al.* Establishment of immortalized primary human foreskin keratinocytes and their application to toxicity assessment and three dimensional skin culture construction. *Biomol. Ther.* **25**, 296–307 (2017).
 21. Gálvez, V. *et al.* Efficient CRISPR/Cas9-mediated gene ablation in human keratinocytes to recapitulate genodermatoses: Modeling of Netherton Syndrome. *Mol. Ther. - Methods Clin. Dev.* **18**, 280–290 (2020).
 22. Lab, Z. Guide design resources (<http://crispr.mit.edu/>).
 23. McMullan, R. *et al.* Keratinocyte Differentiation Is Regulated by the Rho and ROCK Signaling Pathway. *Curr. Biol.* **13**, 2185–2189 (2003).
 24. Strudwick, X. L., Lang, D. L., Smith, L. E. & Cowin, A. J. Combination of low calcium with Y-27632 rock inhibitor increases the proliferative capacity, expansion potential and lifespan of primary human keratinocytes while retaining their capacity to differentiate into stratified epidermis in a 3D skin model. *PLoS One* **10**, 1–12 (2015).
 25. Harms, D. W. *et al.* Mouse Genome Editing using CRISPR/Cas System HHS Public Access. *Curr Protoc Hum Genet* **837**, (2015).
 26. Liu, K. I., Sutrisnoh, N. A. B., Wang, Y. & Tan, M. H. Genome editing in mammalian cell lines using CRISPR-Cas. *J. Vis. Exp.* **2019**, 1–13 (2019).
 27. Khalil, A. A. & de Rooij, J. Cadherin mechanotransduction in leader-follower cell specification during collective migration. *Exp. Cell Res.* **376**, 86–91 (2019).
 28. DeWane, G., Salvi, A. M. & DeMali, K. A. Fueling the cytoskeleton – links between cell metabolism and actin remodeling. *J. Cell Sci.* **134**, jcs248385 (2021).
 29. Bays, J. L., Campbell, H. K., Heidema, C., Sebbagh, M. & Demali, K. A. Linking E-cadherin mechanotransduction to cell metabolism through force-mediated activation of AMPK. *Nat. Cell Biol.* **19**, 724–731 (2017).
 30. Park, J. S. *et al.* Mechanical regulation of glycolysis via cytoskeleton architecture. *Nature* **578**, 621–626 (2020).



7 Future perspectives

*Why does the eye see a thing more clearly in dreams
than the imagination when awake?
(Leonardo Da Vinci)*

"Detection and characterization of mechanical forces and dynamic molecular rearrangements in collective cell migration" – Verónica López

7.1 Future work

The results shown in this dissertation suggest several future research lines:

7.1.1 Adaptation of the force measurement technique to 3D *in vitro* skin cultures

An organotypic 3D skin equivalent, is a three-dimensional culture that replicates the complex structure and function of the skin. It comprises both the epidermis and dermis. 3D skin equivalents are cultured in transwell inserts which allow the culture to be fed from below. Briefly, human primary keratinocytes (HK) are seeded on top of a fibrin matrix populated with fibroblasts which act as the dermal component. The 3D culture is kept submerged until keratinocyte confluence and then placed at the air-liquid interface for 21 days to induce keratinocyte stratification and differentiation to mimic human skin¹ (*Figure 7.1*).

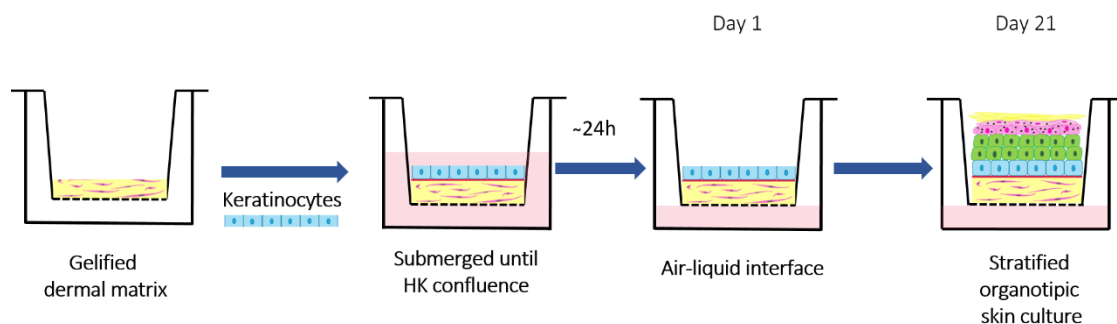


Figure 7.1. Schematic representation of the differentiation process of an organotypic skin culture. Transwells containing the 3D cell culture, are placed in 6-well plates, and kept submerged in culture medium until keratinocyte (HK) confluence. After that, cultures are placed at the air-liquid interface to induce epidermal stratification under regular temperature and humidity cell culture conditions. This is a self-created illustration.

This system reproduces the structure of the skin (*Figure 7.2*) and enables both *in vitro* and *in vivo* experiments, such as pharmacological tests and characterization studies, as well as its use as a treatment of wounds and burns in patients².

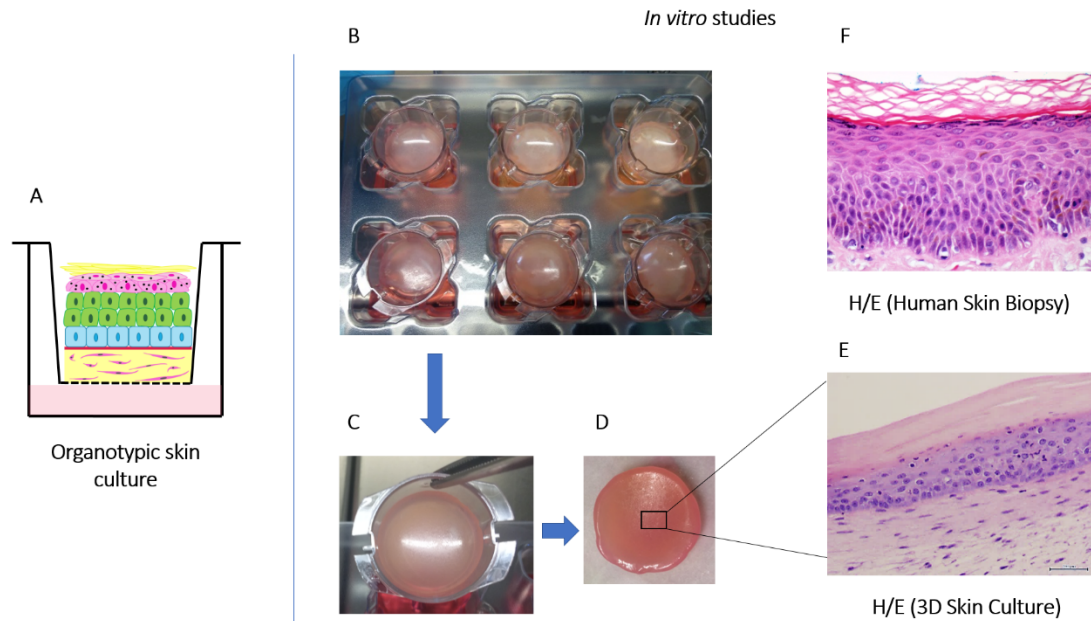


Figure 7.2. Organotypic cultures for in vitro studies. Both in vitro 3D skin culture and human skin biopsy present similar epithelial structures. **A:** Schematic representation of a differentiated organotypic culture. **B:** Six organotypic cultures during the process of in vitro differentiation into a deep well plate. **C:** Single organotypic culture into a transwell. **D:** Differentiated organotypic culture outside of its transwell (prepared for histological procedure). **E:** Haematoxylin/Eosin histological section from the organotypic culture. **F:** Haematoxylin/Eosin histological section from a human skin biopsy. **This is a self-created illustration.**

Similarly to the 2D migration assays where we analyzed both cell velocities and forces exerted by them, we aim to perform a **3D cell tracking** to define the trajectory of cells that divide in the basal layer and form the upper layers of the epidermis during the differentiation process (*Figure 7.3*).

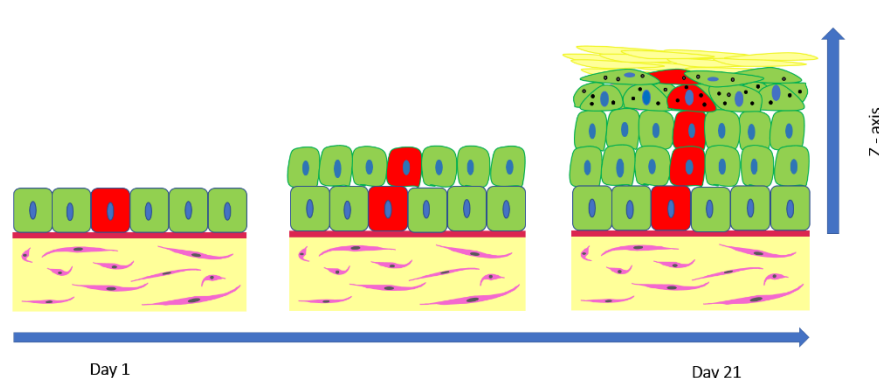


Figure 7.3. Schematic representation of the 3D cell tracking experimental procedure proposed. As epidermis grows up, the progeny of a single cell could be visualized in red. **This is a self-created illustration.**

For 3D cell tracking visualization, HaCat cells are previously transduced with two different viral vectors (retroviral pBABE-H2BGFP (*Addgene*, 26790) and lentiviral plenti-H2BmCherry (*Addgene* 89766)) to obtain two different populations of fluorescent nuclei keratinocytes (green and red). It should be noted that HaCat cells are chosen given their ease of handling and maintenance.

Fluorescent HaCat cells are then seeded on top of the dermal matrix at different percentages (99% green cells + 1% red cells) to be able to distinguish the progeny of these individual cells as epidermal layers are being formed (*Figure 7.4*). This could help to visualize the entire keratinocyte layer and distinguish the carbon fiber within the three-dimensional culture when placed for measurement of forces.

This experimental setup is still being improved since it presents several technical difficulties. Although this configuration enables imaging of epidermis formation over time (*Figure 7.4*), other microscopy methods that allow for better resolution and minimal modifications of the skin culture conditions (such as two photon microscopy or light sheet microscopy) should be considered.

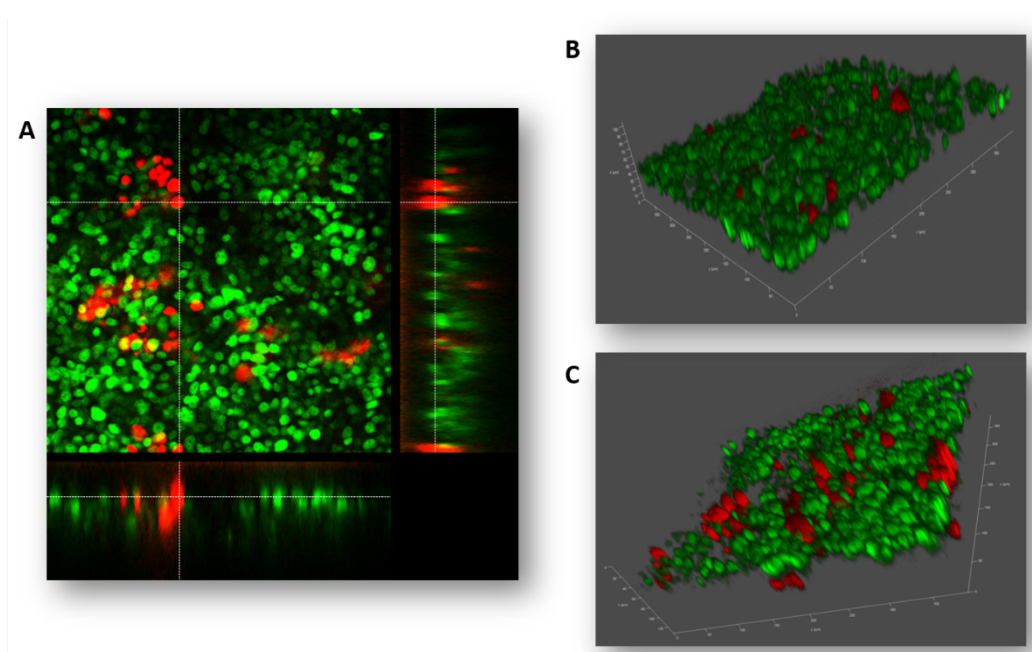


Figure 7.4. Preliminary results of 3D cell tracking imaging. **A.** Orthogonal visualization of a 3D skin culture (14 days of epidermal differentiation). **B.** 3D image of an organotypic skin culture (5 days of epidermal differentiation). **C.** 3D image of an organotypic skin culture (14 days of epidermal differentiation).

Once this cell tracking procedure is well established, we plan to adapt the fiber-force sensor technique into the three-dimensional culture, to concomitantly analyze the dynamic and kinematic evolution of the differentiating epidermis *Figure 7.5* shows a plausible positioning of the fiber.

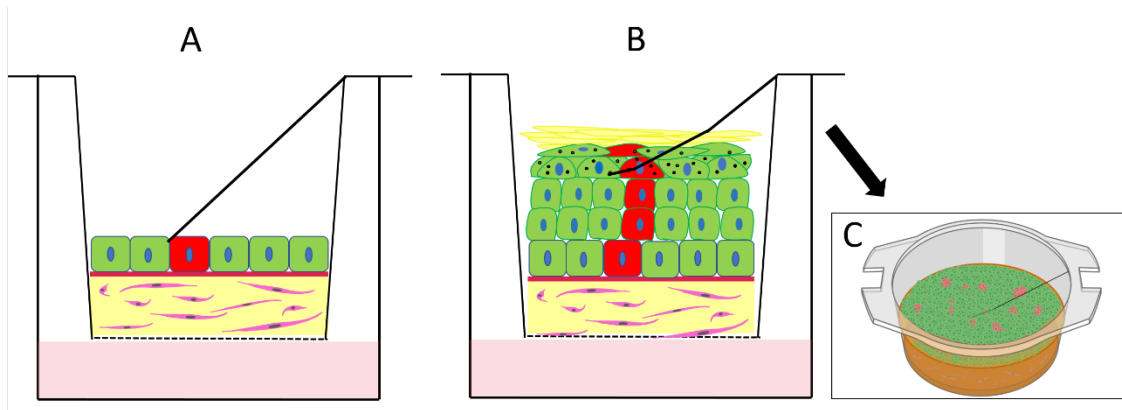


Figure 7.5. Sketch of a carbon fiber immersed in a developing organotypic skin culture during differentiation process. A. Day 1 of differentiation. B. Day 21 of differentiation. The fiber is expected to be bent. C. Top view of a transwell containing a positioned fiber. Black line. Fiber.

7.1.2 Detection of intracellular levels of ATP:ADP

From the theoretical model described in chapter 4, we hypothesized that: “the mechanical work exerted by cells is a limiting factor for a tissue to expand”. In order to confirm that hypothesis, we aim to analyze the energetic profile of migrating cells while pushing the fiber.

HaCat cells are chosen for the experimental setup given their ease of handling, and are transduced with a lentiviral vector to express a fluorescent ratiometric ATP:ADP sensor³ (*FUGW-PercevalHR*, *Addgene 49083*). Selected positive HaCat cells are used for time-lapse fluorescence imaging. Migrating cells, with and without fiber, are monitored for 72h (*Figure 7.6*).

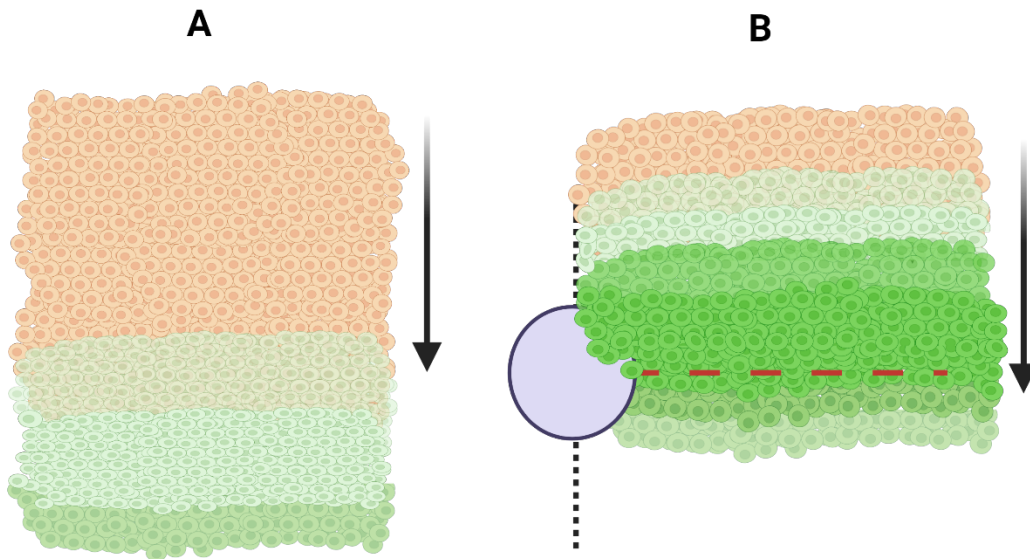


Figure 7.6. Schematic representation of the experimental setup for ATP:ADP ratio analysis. Black arrows. Direction of migration. A. Control (migrating cell monolayer without fiber). We expect higher fluorescence intensity at the leading edge and progressive decrease towards the inner tissue. B. Migrating cell monolayer with fiber. We expect the cells pushing the fiber to exhibit a higher fluorescence intensity than cells at the leading edge. Red dashed line. Indicates the fiber position.

According to a recent study that describes a higher energy demand of cells that migrate through narrow and rigid places⁴, we expect HaCat cells to show increased ATP fluorescence levels in cell monolayers that are pushing the fiber compared to those that migrate freely. In addition, given the recent demonstrated evidence of reprogramming of cellular metabolism in response to actin remodeling⁵, we aim to correlate these results with the F-actin gradient observed in the tissue upwards the fiber. Thus, we intend to study the relationship between the time evolution of ATP:ADP ratios and mechanical work exerted by cells under different conditions. Further experiments testing different fiber stiffnesses, metabolic pathways involved, and glucose uptake will be needed to obtain robust data.

1. Meana, A. *et al.* Large surface of cultured human epithelium obtained on a dermal matrix based on live fibroblast-containing fibrin gels. *Burns* **24**, 621–630 (1998).
2. Llames, S. G. *et al.* Human plasma as a dermal scaffold for the generation of a completely autologous bioengineered skin. *Transplantation* **77**, 350–355 (2004).
3. Tantama, M., Mongeon, R. & Yellen, G. Imaging energy status in live cells with a fluorescent biosensor of the intracellular ATP-to-ADP ratio. *Nat Commun.* 1–27 (2013). doi:10.1038/ncomms3550.Imaging
4. Zanotelli, M. R. *et al.* Energetic costs regulated by cell mechanics and confinement are predictive of migration path during decision-making. *Nat. Commun.* **10**, 1–12 (2019).
5. DeWane, G., Salvi, A. M. & DeMali, K. A. Fueling the cytoskeleton – links between cell metabolism and actin remodeling. *J. Cell Sci.* **134**, jcs248385 (2021).



8 Concluding remarks

*“All our dreams can come true,
if we have the courage to pursue them.”
(Walt Disney)*

“Detection and characterization of mechanical forces and dynamic molecular rearrangements in collective cell migration” – Verónica López

8.1 Conclusions

1. We developed an affordable and easy-to-implement force measurement technique for cell monolayers based on a flexible structure of known mechanical properties (a carbon fiber). This technique is amenable to be translated to three-dimensional tissues.
2. Based on the results observed, a fluid-based theoretical model was formulated to describe how a multicellular tissue modulates the force it exerts depending on the compliance of its external surroundings. The model captures the essential features of the fiber-cell monolayer system, namely: effective inertia, viscous stress between cells, and elastic force.
3. From the mathematical relationships established, we extracted information on the biological behavior of the tissue:
 - The tissue exhibits a viscous fluid behavior responsible for the overdamped fiber oscillations.
 - The fiber stiffness is inversely proportional to the maximum force exerted by the monolayer.
 - The fiber accumulates the same maximum elastic energy per unit length regardless of its stiffness.
4. Immunofluorescence staining showed that the presence of the fiber has a clear effect on F-actin cytoskeleton reinforcement in response to an increase in environmental rigidity, and generates an inward gradient as previously reported by other studies. E-cadherin staining only revealed an overall intercellular tensional state transmitted throughout the monolayer.
5. A kindlin-1 cellular model was generated by CRISPR/Cas9 technology and proved to exhibit a phenotype typical of cells from Kindler syndrome patients.

6. Our force measurement technique was sensitive enough to detect dynamic differences between healthy cells and kindlin-1 deficient cellular model. This confirms its potential usefulness in the study of various diseases involving mechanotransduction defects.

7. Analysis of kindlin-1 deficient cells revealed that:
 - Forces exerted by Kin1⁻ cells are similar to those applied by HaCat cells when pushing fibers longer than 3mm (more compliant) but weaker on 2 mm fibers (the stiffest ones).

 - Kin1⁻ cells migrate faster due to a deficient cell-ECM adhesion but their undirected migration and their lack of a coordinated collective behavior results in delayed wound healing.

 - Despite the variability among the experiments caused by the erratic behavior of Kin1⁻ cells, the correlations predicted by the theoretical model are in reasonable agreement with the experiments.

*“From now on
what's waited 'til tomorrow starts tonight [...] and we will come back
home, home again”
(The greatest showman)*

